

Alma Mater Studiorum – Università di Bologna

DOTTORATO DI RICERCA IN

CHIMICA

Ciclo XXXII

Settore Concorsuale: 03/C1

Settore Scientifico Disciplinare: CHIM/06

**Unconventional Catalysis in Organic Chemistry:
a Computational Mechanistic Study**

Presentata da: Edoardo Jun Mattioli

Coordinatore Dottorato

Prof.ssa Domenica Tonelli

Supervisore

Prof. Matteo Calvaresi

Esame finale anno 2020

Abstract

Catalysis plays a vital role in modern synthetic chemistry and a large amount of everyday chemistry is based on catalysed transformations. Nowadays, different catalytic methods can be applied “routinely”. These are organo-catalysis, metal-catalysis and enzyme-catalysis and can be denoted as *conventional* catalysis. However, even if conventional catalysis has provided outstanding results, various *unconventional* ways to make chemical reactions more effective appear now very promising. In many cases, the experimental conditions required by these unconventional catalytic methods are rather complicated and the interpretation of results is not obvious. Computational methods can be of great help to reach a deeper comprehension of these chemical processes. Methods used in this thesis, to discuss different unconventional approaches to catalysis, are Quantum-Mechanical (QM), Molecular Mechanics (MM) and hybrid Quantum-Mechanical/Molecular Mechanics (QM/MM) methods. The first catalytic approach examined in this thesis consists in the application of Oriented External Electric Fields (OEEFs) to reacting systems. The second approach is based on the use of Carbon Nanotubes (CNTs) working as nano-reactors: the reaction is confined inside a CNT. Finally, a new biochemical approach (alternative to the well-known enzymatic catalysis), based on the use of a biocatalyst obtained from DNA (Deoxyribozyme) is discussed. All these approaches cannot be considered “routine” catalytic techniques yet and this makes even more important the use of computational methods to elucidate the mechanism of these novel catalyses. The effects of OEEFs on S_N2 and 4e-electrocyclic ring opening mechanisms were examined using QM methods. S_N2 reactions with *back-side* mechanism can be catalysed or inhibited by the presence of an OEEF. Moreover, OEEFs can inhibit *back-side* mechanism (with Walden inversion of configuration) and promote the *front-side* mechanism (with retention of configuration). This mechanistic change leads to a different stereochemical output of the reaction. Electrocyclic ring opening reaction of 3-substituted cyclobutene molecules can occur with *inward* or *outward* mechanisms. The *inward* and *outward* selectivity (*torquoselectivity*) depends on the nature of substituent groups on the cyclobutene structure. OEEFs can catalyse the naturally favoured pathway in agreement with the *torquoselectivity* principle. Moreover, OEEFs can circumvent the *torquoselectivity* principle leading to different stereoisomers. Subsequently, the reaction of ethyl chloride with chloride anion inside CNTs, used as nano-reactors, was investigated. In addition to the S_N2 mechanism, *syn* and *anti*-E2 reactions are possible. These reactions inside CNTs of different radius were examined with hybrid QM/MM methods, finding that these processes can be either catalysed or inhibited. The

results suggest that Electrostatic effects govern the activation energy variations inside CNTs of different diameters. Nonetheless, in the case of elimination products, van der Waals interactions become as important as electrostatic interactions. Elimination products stabilisation is additionally enhanced if the reaction occurs on a graphene sheet. Finally, the catalytic mechanism of the deoxyribozyme 9DB1 was investigated at the QM level. 9DB1 catalyses the RNA ligation reaction thanks to its ability to orient RNA strands in a conformation which allows the regioselective formation of the 3'-5' bond. Reactive RNA nucleotides can be positioned close to each other. This is done by means of the Watson-Crick base pairing which recognizes and properly orients reactants. After this pre-reactive organisation process, 9DB1 catalyses the regioselective RNA ligation reaction, following an addition-elimination (A_N+D_N) two-step mechanism. *In silico* mutagenesis studies confirmed that the highly polarised environment of 9DB1 enhances kinetics.

Contents

Introduction	1
1 Theoretical Background	3
1.1 Reaction Mechanisms	4
1.1.1 Geometry Optimization	5
1.1.1.1 Transition States Location	6
1.1.2 Critical Points Characterisation	8
1.1.3 Quantum Mechanics	8
1.1.3.1 Basis Set	11
1.1.3.2 Correlation Energy	12
1.1.3.3 Density Functional Theory	14
1.2 Solvent effects	17
1.2.1 Continuum Medium Models	18
1.3 Molecular Dynamics	21
1.3.1 Force Field	21
1.3.2 Verlet Method	22
1.3.3 Approximations Inside Molecular Dynamics Simulations	23
1.4 Hybrid Quantum Mechanics/Molecular Mechanics Methods	24
1.4.0.1 Energy of a QM/MM system	24
1.4.0.2 Electrostatic QM/MM Interactions	26
1.4.0.3 The Boundary region	27
2 Oriented External Electric Fields	29
2.1 Computational Methods	31
2.2 Substitution Reactions	33
2.2.1 Introduction	33

2.2.2	Results and Discussion	34
2.2.2.1	Type I Substitution Reactions	34
2.2.2.2	Case Study: OEEF-Functional Group Relationship	42
2.2.2.3	Type II Substitution Reactions	49
2.3	Electrocyclic Reactions	64
2.3.1	Introduction	64
2.3.2	Results and Discussion	66
2.3.2.1	Electron-Donor Substituents	68
2.3.2.2	Electron-Acceptor Substituents	72
2.4	Conclusions	79
3	Carbon Nanotubes	83
3.1	Introduction	83
3.2	Computational Methods	86
3.3	Results and Discussion	87
3.3.1	Gas Phase Reaction Profiles	87
3.3.2	Carbon Nanotube Confined Reaction Profiles	87
3.3.3	Substitution Mechanism	89
3.3.4	Elimination Mechanism	92
3.3.4.1	Kinetics	92
3.3.4.2	Thermodynamics	94
3.3.5	4-Chloro-1-butene	96
3.4	Conclusions	99
4	Deoxyribozymes	101
4.1	Introduction	101
4.2	Computational Methods	102
4.3	Results and Discussion	105
4.3.1	Reaction Mechanism Investigation	105
4.3.2	<i>In Silico</i> Mutagenesis	109
4.4	Conclusions	111
	Conclusions	113
	Bibliography	115
	List of Figures	124
	List of Tables	131

Introduction

Following the most common definition, catalysis is a process where the reaction rate is increased by adding a substance (catalyst) to the reaction mixture. The catalyst is not consumed. It is recovered at the end of the reaction and, apparently, does not participate to it. A key-concept concerns the balance between the thermodynamics of a reaction, which tells that a chemical reaction is possible, and the kinetics which tells how fast this chemical reaction will proceed. A catalyst does not change the final state (products) of a reacting system because the equilibrium state is governed by thermodynamics. A catalyst provides an easier way to proceed from reactants to products by modifying the reaction mechanism. The catalysed mechanism involves activation barriers lower with respect to the non-catalysed process, which leads to an increase of the reaction-rate.

Nowadays, the importance of catalysis is unquestionable and a large amount of everyday chemistry is based on catalysed transformations. Different approaches to catalysis are possible and can be applied “routinely”. These are bio-catalysis, organo-catalysis and metal-catalysis. These approaches to catalysis are keystones in organic chemistry and can be grouped together as *conventional* catalysis methods.

Even if *conventional* catalysis has provided outstanding results, other approaches to catalysis are possible. Various *unconventional* ways to make chemical reactions more effective appear now very promising. However, in many cases the experimental conditions required by these *unconventional* catalytic methods are rather complicated and the interpretation of results is not obvious. In this sense, computational methods can be of great help in the investigation of these novel ways to promote reactions.

During the last decades it has been demonstrated that, in general, a reasonable modelling of the reacting system and the use of appropriate computational meth-

ods can be highly effective to reach a deep comprehension of chemical processes. The first goal of a theoretical approach is the comprehension of the reaction mechanism. In this sense, computational chemistry can provide a detailed picture of the reaction pathways. Without a detailed knowledge of the possible mechanisms, it is inconceivable to understand how a catalytic (*conventional* or *unconventional*) method works, to make predictions on the reaction outcome and, consequently, to suggest appropriate experimental conditions. Importantly, the application of computational techniques is not an automatic procedure where computer does everything. In general, the complexity of the problem requires a preliminary and careful modelling of the reacting system. Secondly, a correct choice of the computational approach (level of theory) must be done.

In this thesis computational methods to discuss different *unconventional* approaches to catalysis are used. The first approach examined here consists in the application of Oriented External Electric Fields (OEEFs) to reacting systems. The second approach is based on the use of Carbon Nanotubes (CNTs) working as nano-reactors: the reaction is confined and occurs inside the nanotube. Finally, a new biochemical approach (alternative to the well-known enzymatic catalysis), which is based on the use of a biocatalyst obtained from DNA (Deoxyribozyme) is discussed. All these approaches cannot be considered "routine" catalytic methods yet and only in the last decade papers dealing with these new techniques begin to appear in literature. This makes even more important the use of computational methods to elucidate the mechanism of these new catalyses. This research aims to provide some insight on these *unconventional* ways to catalyse chemical reactions. To investigate the effects of these *unconventional* catalytic methods, appropriate model-systems were built for each reaction. The definition of the model-systems was based on a detailed study of the available related literature and a careful analysis of the experimental conditions.

In general, the model-system built to emulate the real system, can be described with different theoretical methods, depending on the investigated properties. These methods can be Quantum-Mechanical (QM) methods, Molecular Mechanics (MM) methods and hybrid Quantum-Mechanical/Molecular Mechanics (QM/MM) methods. Since this thesis is focused on reactivity, QM and hybrid QM/MM approaches were mainly employed. In both cases the reactive portion of the model-system is described using quantum mechanics, which represents the correct approach to describe bond-breaking and bond-forming processes occurring in the course of a chemical reaction.

CHAPTER 1

Theoretical Background

Organic computational chemistry describes organic and biomolecular systems with a theoretical approach. This approach consists of the translation of the subject of studies into a model system which could describe and predict its properties by solving physical equations.

Depending on the type of information researched, different computational methods are available. For the description of a reactive process it is necessary to describe bonds break and formation, this is fundamental to conjecture a reaction mechanism. Since the chemical bond is a quantum phenomenon depending on the electronic structure of a molecule, Quantum Mechanics (QM) methods are needed. Even if this approach guarantees a good description of the molecular reality, the computation demanding prohibits this approach for big molecular systems.

The information which does not require the electronic structure description, like the behaviour of a system during non-reactive processes, could be calculated with a classical approach based on Newtonian mechanics. These methods termed Molecular Mechanics (MM) methods, thanks to a simpler representation of the system, can describe N-particle systems and can be useful for an important application of these methods: the Molecular Dynamics (MD). MD simulations allow to follow the evolution of a system during the time; its applicability to big systems, such as natural bio-molecules, have made MD simulations widely used, especially in the description of conformational changes.

1.1 Reaction Mechanisms

A reaction mechanism is the step by step sequence of elementary reactions by which overall chemical change occurs. [1]

In chemistry, it is a theoretical conjecture that tries to describe detailed steps of a reaction. The knowledge of a reaction mechanism is the knowledge of the chemical system behaviour during a reactive process. With this information, it is possible to explain experimental results and to hypothesise ways to induce a reactive system to follow a determinate path to a determinate output by modifying reaction conditions or by adding reagents, auxiliaries and catalysts.

There are different ways to investigate a reaction mechanism. Many experimental methods are available to provide insight into the understanding of what leads reactants to evolve into products. However, all these methods have limitations due to the impossibility to observe single-molecules during reactions.

In this sense, computational chemistry has the unique advantage to be able to observe single molecule system evolving during the reactive process and to quantify observables which allows deriving kinetics and thermodynamics data.

In computational chemistry to know the reaction mechanism means to know the Potential Energy Surface (PES) of the system. PES describes the energy of a system, especially a collection of atoms, in terms of atomic coordinates. The surface defines the energy as a function of these coordinates. For a given collection of atoms, all the coordinates mean also all the possible way to dispose atoms in space. Chemistry laws define which disposition are forbidden and which dispositions define stable states such as molecules.

If the PES contains all the energies of all atomic dispositions, to follow a determinate evolution of this dispositions means to follow a chemical process which can be a geometrical rearrangement (*i.e.* conformation change or folding process) but also a reactive process. To determine the energy profile of a reactive process means the knowledge of the related reaction mechanism.

If there are N nuclei, the dimensionality of the PES is $3N$. Three coordinates describe the translation of the system, and three coordinates describe the rotation of the system. This leaves $3N - 6$ coordinates or $3N - 5$ coordinates for linear molecules, where the rotational degrees of freedom are defined by two coordinates instead of three. Unfortunately, systems with more than four atoms (pratically all the systems) make the determination of the analytical form of the PES hyper-surface virtually impossible.

To determine a reaction mechanism it is necessary to know the critical points of the PES. Minima represent stable species (Reactants, intermediates and products), first-order saddle points which connect minima are transition states (TSs)

related to what is called Minimum Energy Path (MEP). The reaction mechanism is conceivable as the determination of a PES section along the so-called reaction coordinate, a bi-dimensional plot which represent the energy as a function of the geometrical rearrangement (connectivity changes in the case of reactive process *i.e.* bonds breaking and formation) which lead reactants to products.

1.1.1 Geometry Optimization

Critical points characterization of the critical points is possible through the evaluation of the first and second-order derivatives of the PES. For a many-variable function, the first-order derivatives calculated in respect of each variable form the gradient vector, while the second-order derivatives originate the Hessian matrix. In classical mechanics this gradient vector (\mathbf{g}_i), with opposite sign, represents the forces acting on the system; the Hessian matrix (\mathbf{H}) indicates how much this force can perturb the set of internal coordinates and this is the force constant of the corresponding nuclear motion. A point is considered a critical point if the gradient in that point is null. The nature of this critical point is determined by the number of negative eigenvalues which characterize the Hessian matrix in that point. If each eigenvalue is negative the point is a local maximum, vice versa if all eigenvalues are positives the point is a local minimum, for n negative eigenvalues with all the remaining eigenvalues positives, the point is a saddle point of $n - th$ order.

Being the functional form of the PES too complex to be analytical determined, a fundamental approximation has been done: the surface near a critical point is locally described as a quadratic function. The starting point is the Taylor expansion on the PES truncated, in agreement with the approximation done, at the second order:

$$E(x) = E_k + \mathbf{g}_k^T(x - x_k) + \frac{1}{2}(x - x_k)^T \mathbf{H}_k(x - x_k) \quad (1.1)$$

Where x_k is the position vector that locates a certain structure on the PES, \mathbf{g}_k^T is the gradient, \mathbf{H}_k is the Hessian matrix and E_k is the energy of the x_k point. The optimization process starts with an estimated Hessian \mathbf{H}_0 ; this estimation can be done through empirical methods. Even if an empiric Hessian is highly approximate, the important point is to have a good geometry, derivable from model systems. The \mathbf{H}_0 quality is improved continually during the optimization. The optimization algorithm for the research of the equilibrium geometry in a critical point can be summarized as:

- from the starting atomic coordinates x_k ; $k = 0$, H_0 or its inverse matrix is estimated;
- E_k and g_k values are obtained from x_k ;
- Hessian matrix and gradient vector are improved for having a better PES model in agreement with real energy value;
- the calculation “moves” on the surface to search for a minimum by using the gradient vector and the updated Hessian matrix. The displacement along the PES is regulated by the following conditions:

$$\frac{dE}{dx} = g_k + B_k(x - x_k) = 0 \quad (1.2)$$

$$(x - x_k) = p_k = -B_k^{-1}g_k = H_k g_k \quad (1.3)$$

- if the gradient g_k or the displacement vector p_k are smaller than a fixed threshold, the calculation is converged and stops;
- the optimization goes on by moving to the selected direction, minimizing $E_k(x_k + \alpha p_k)$ with respect to α ;
- the variables $(x_{k+1}) = (x_k + \alpha p_k)$; $k = k + 1$ are defined and the process re-starts from point 2.

This method is called *Newton-Raphson* (NR) method and is a second-order method because it uses both first and second-order derivatives. Due to the computational cost of second-order methods, first-order methods aim to reach critical points with only the gradient vector. The *Steepest Descent* (SD) method is an algorithm that performs the geometry optimizations by considering only the negative gradient direction, since that is the direction where the function decreases most. By following the negative gradient direction, it is possible to minimize a function. Because of its nature, the SD method can only locate minima. The main problem is that this method “forgets” the history of the performed steps so the curvature of the function. *Conjugate Gradient* (GC) method tries to keep in memory the previous step gradient to have an indirect knowledge of the PES curvature.

1.1.1.1 Transition States Location

Transition state location is fundamental to elucidate a reaction mechanism, since minima can only provide thermodynamics data while transition states provide kinetic data. Different techniques are available to find the transition state structure. During a reaction, the system moves from a minimum to the next one passing through a saddle point. The number of negative eigenvalues can be used to distinguish a saddle point from a minimum. NR method is an exact method inside the quadratic region, however, differently from minima, the transition region is often non-quadratic outside a small neighbourhood of the transition state.

A usual method to elucidate the reaction path is to scan the PES by systematically varying the internal coordinates which are supposed to be part of the reaction coordinate in the mechanistic hypothesis. This method is called relaxed PES scan. Suppose a process that can be described by means of a single coordinate *i.e.* dihedral torsion: it is possible to scan the dihedral angle and collect the energy of the system as a function of the dihedral angle value. From the minimum to the transition state, the energy will increase, subsequently, from transition state to the next minimum, the energy will decrease. The maximum energy should be accompanied by the sign change in the eigenvalue related to that mode (the related eigenvector).

It is worthy of attention that a relaxed scan of a single internal coordinate will require N calculations while the grid scan of two internal coordinates will require N^2 and hence with the power of internal coordinates investigated. This growth of the computational demand implies that the scan should be carried out close to the transition region making the scanned region choice based on the chemical knowledge of the system.

Transition structure can be refined with an optimisation step from the extrapolated geometry of a previous scan. To carry out this further calculation different techniques can be used. The most intuitive method is to use the NR method to find a saddle point of order I. The success of this method is strongly related to the starting geometry. The Eigenvector-Following (EF) method is an implementation of the NR method which follows the negative eigenvector direction. [2–4] This calculation can be achieved with a full-Hessian matrix calculation or by calculating only the Hessian matrix elements of a few internal coordinates which are supposed to be involved in the reactive process. Moreover, to assist this calculation, the Berny algorithm which checks the number of negative eigenvalue during the calculation can be suppressed, differently from minima optimisation where it is generally used. [5] Alternatively, the Hessian matrix can be recalculated during the TS optimisation each NR step or every n steps.

An alternative method to locate TSs is the Synchronous Transit-Guided Quasi-Newton (STQN) method. [6, 7] It extrapolates the transition state structure starting from the adjacent minima and then, STQN uses a quadratic synchronous transit approach to get closer to the quadratic region of the transition state. To complete the TS optimisation it switches to a quasi-Newton or eigenvector-following algorithm.

1.1.2 Critical Points Characterisation

After the geometry optimisation it is necessary to know where this geometry is located on the PES to have knowledge of the chemical meaning of the optimised structure. Each geometry is a point on the PES however, to determine a reaction mechanism it is necessary to know the *critical points* which connect reactants to products. The characterisation of a critical point is achieved by analysing the derivatives of the PES function.

The Hessian matrix diagonalisation allows to characterise the critical point and to check whether it is a minimum or a saddle point. Moreover, in the framework of the harmonic approximation, the eigenvalues and eigenvectors of the Hessian matrix represent the Hooke constants (eigenvalues) of the related normal mode (eigenvector) of a molecule.

A non-linear polyatomic molecule possesses $3N - 6$ independent normal modes which wavenumber $\tilde{\nu}$ (cm^{-1}) is:

$$\tilde{\nu} = \frac{1}{2\pi c} \sqrt{\frac{k}{\mu}} \quad (1.4)$$

where c is the speed of light, k is the force constant of the vibration or Hessian matrix eigenvalue and μ is the reduced mass. In fact, the Hessian's eigenvalue matrix comprises the force constants for all the $3N - 6$ vibrations. When all the Hessian eigenvalues are positive, the point is a minimum, when all but one Hessian eigenvalue are positive, the point is a first-order saddle point (transition state). In addition to the topological information related to the optimised geometry, the computation of normal modes also allows evaluating the Zero-Point Energy (ZPE). ZPE is a quantum effect, this effect arises because of the uncertainty principle. Being the position of the a particle uncertain, the momentum of the particle is uncertain too ($\Delta p \neq 0$) and hence the kinetic energy can not be zero too. An harmonic oscillator has $ZPE = h\nu/2$, this energy contribution emerges from the energy of the vibrational wave-function. The oscillator never stops fluctuating about its equilibrium position. If $E_{ZPE} = 0$, $E = 0$. Kinetic and potential energies are both zero, which implies $p = x = 0$ that is contrary to Heisenberg uncertainty principle.

1.1.3 Quantum Mechanics

The importance of quantum theory resides in some fundamental empirical observations which lead to a new conception of subatomic particles. Quantum

mechanics describes subatomic particles, and then also the electrons, as corpuscles and waves. This dual character of electrons imply the non-locality of such particles, which means the impossibility to distinguish one electron from another. Heisenberg's indetermination principle says that one electron has only a probability to be in a determinate point of the space. This new way, in agreement with the experimental data, to conceive the electrons also explains the reason why the calculation methods based on the deterministic engine of Newtonian mechanics fails in the description of chemical reactions mechanisms.

The probability to find an electron in a spatial region is described by the wave function which is the solution of the time-independent Schrödinger equation:

$$\hat{H}\psi(x, y, z) = E\psi(x, y, z) \quad (1.5)$$

Where \hat{H} is the Hamiltonian operator. In organic computational chemistry the interest is focused on polyatomic systems, more than single particle systems, one which is defined as:

$$\begin{aligned} \hat{H} = & - \sum_{\alpha=1} \frac{\hbar^2}{2M_{\alpha}} \nabla_{R_{\alpha}}^2 - \sum_{i=1} \frac{\hbar^2}{2m_e} \nabla_{r_i}^2 - \sum_{i=1} \sum_{\alpha=1} \frac{Z_i e^2}{4\pi\epsilon_0 |R_{\alpha} - r_i|} \\ & + \sum_{i=1} \sum_{j>i} \frac{e^2}{4\pi\epsilon_0 |r_i - r_j|} + \sum_{\alpha=1} \sum_{\beta>\alpha} \frac{Z_{\alpha} Z_{\beta} e^2}{4\pi\epsilon_0 |R_{\alpha} - R_{\beta}|} \end{aligned} \quad (1.6)$$

The first term represents the kinetic energy operators for each nucleus in the system; the second term represents the kinetic energy operators for each electron in the system; the third term represents the potential energy between the electrons and nuclei (the total electron-nucleus Coulombic attraction in the system); the fourth term represents the potential energy arising from Coulombic electron-electron repulsions; eventually, the fifth term represents the potential energy arising from Coulombic nuclei-nuclei repulsions (also known as the nuclear repulsion energy).

The Hamiltonian in Eq 1.6 contains attractive and repulsive terms between the particles and the fourth term makes impossible to analytically solve the Schrödinger equation for systems with more than one electron. Electronic motion is correlated and some approximations are required. The first fundamental approximation is the Born-Oppenheimer (BO) approximation which allows decoupling electronic and nuclear motion. Being nuclei heavier than electrons their kinetics energy is lower by a factor of 10^5 and the electronic motion can be modelled as in presence of a fixed nuclear field. In this view, nuclear kinetic energy can be eliminated, and the repulsive nuclear-nuclear potential is constant (V_{NN}) for a given geometry. With the BO approximation \hat{H} becomes an electronic

Hamiltonian \hat{H}_{el} :

$$\hat{H}_{el} = - \sum_{i=1} \frac{\hbar^2}{2m_e} \nabla_{r_i}^2 - \sum_{i=1} \sum_{\alpha=1} \frac{Z_i e^2}{4\pi\epsilon_0 |R_\alpha - r_i|} + \sum_{i=1} \sum_{j>i} \frac{e^2}{4\pi\epsilon_0 |r_i - r_j|} \quad (1.7)$$

$$= T + V_{Ne} + V_{ee} \quad (1.8)$$

where T is the kinetic operator, V_{Ne} the nuclear-electron attraction operator and V_{ee} the electron-electron repulsion operator. The Schrödinger equation based on the electronic motion, where the potential repulsion between the nuclei is added as V_{NN} . two Schrödinger equations can be written now:

$$[\hat{H}_{el} + V_{NN}] \psi_{el}(r, R) = E_{el}(R) \psi_{el}(r, R) \quad (1.9)$$

$$\left[- \sum_{\alpha=1} \frac{\hbar^2}{2M_\alpha} \nabla_{R_\alpha}^2 + V_{NN} \right] \psi_{nuc}(R) = E_{nuc} \psi_{nuc}(R) \quad (1.10)$$

Eq. 1.9 depends on the electronic coordinates. The nuclear repulsion V_{NN} is independent on the electrons and it is a constant for a given nuclear configuration or geometry. ψ_{tot} can be factorised as product of a nuclear and electronic functions (Eq. 1.11).

$$\psi_{tot}(r, R) = \psi_{nuc}(R) \psi_{el}(r, R) \quad (1.11)$$

$\psi_{tot}(r, R)$ is the total wave-function, $\psi_{nuc}(R)$ is the nuclear wave-function and $\psi_{el}(r, R)$ is the electronic wave-function. $E_{el}(R)$ is the sum of the potential energy of the system with the electronic kinetic energy. $E_{el}(R)$ is called BO surface and is the PES of the system. It defines electronic energy as a function of a set of nuclear coordinates. While nuclei are frozen, electrons show quantum aspects. The nuclear motion is classically described while the related energy is defined by the electronic structure described with the quantum theory. This approximation for the nuclear motion takes note of the higher mass of nuclei compared to electrons which make the probability to observe quantum behaviour for nuclei very low.

This low probability makes BO approximation reasonable. If nuclear motion shows quantum behaviour, nuclei would be able to adopt a linear combination of configurations and molecules would modify their geometry by tunnelling through energetic barriers, this phenomenon has a very low probability to occur. A cyclohexane molecule would become a 2-hexene molecule without following the organic reactivity laws.

1.1.3.1 Basis Set

Mono-electronic wave functions that describe the probability to find an electron in a spatial region are defined as atomic orbital in the atomic case or molecular orbitals (MO) in the molecular case. In organic computational studies, the molecules under exam could be of large dimension and the MO used to describe their behaviour are expressed as Linear Combinations of Atomic Orbitals (LCAO). $\psi_i = \sum_{j=1}^N c_{ij}\phi_{ij}$ Where ψ_i is the MO i -th, c_{ij} the associated coefficient. The j -th wave function is part of a set of atomic orbitals called basis set, used to generate the LCAO for the MO description.

The basis set is strictly correlated to the quality of the MO representation, with the increase of the number of atomic orbitals used, the representation will increase in quality. This quality is every time bonded to the compromise of the calculation power, which prohibits something similar to an infinite number of atomic orbitals. AOs, which composed the basis set, exist as a solution of the Schrödinger equation only for the hydrogen atom. The new problem is the quality of the representation of the atomic orbital. Slater Type Orbitals (STOs) try to do this, they are built ad hoc with empirical parameter. However, these orbitals can be problematic, especially in the numerical resolution of polycentric integrals.

The new generation of orbitals developed by Boys [8] and later by Shavitt and Karplus, [9] is known as Gaussian Type Orbitals (GTOs). GTOs are well employed in computational methods and described by:

$$\chi_j^{GTO} = Nx^l y^m z^n e^{-a(x^2+y^2+z^2)} \quad (1.12)$$

where N is a normalization constant and a is the orbital exponent, which is a constant and defines the radial expansion of the function. Defining the azimuthal quantum number: $L = l + m + n$, for $L = 0$ the GTO describes a s orbital, $L = 1$ a p orbital and so on. The principal difference with respect to STOs is the exponential dependence of the radial part; this difference makes GTOs worse than STOs in the description of electron density near and far from the nucleus. The approach for employing this kind of orbital in the representation of an AO is to use a linear combination of those called primitive Gaussian functions χ_j^{GTO}

$$\phi_i = \chi_i^{STO} = \sum_{ij} b_{ij}\chi_j^{GTO} \quad (1.13)$$

where ϕ_i is called contracted Gaussian function and b_{ij} is the contraction coefficient known and constant during the calculation. Independently from the choice of STOs or GTOs the number of functions which compose the basis set is fundamental for the accuracy of the calculation. The minimal basis set gives to each

atom a number of basis functions necessary to place each electron. This basis functions could be STOs represented as linear combination of GTOs. In order to approximate an accurate orbital with less computing-demanding functions.

If the summation in Eq.1.13 runs from $i = 1$ to N , this orbital is called STO-NG which means that the representation of this STO is approximated as a sum of N GTOs. This kind of basis set is the most popular minimal basis set, STO-3G for example could provide good geometry description, for molecules in the ground state and composed by elements of the first period; but observables like the energy are less accurate. The main problems are:

- while during the course of a reaction, MO physiognomy change, the coefficients and the GTO function remain fixed during the calculation giving to the orbitals of the system an unnatural rigidity;
- for the same reason, the anisotropy of the MOs belonging to a molecular system is not described. This is true for the orbital orientation in the orbital space without a spherical symmetry even for the description of the charge distribution;
- if each element of the same period is described with the same number of basis function, even if the number of electron increases from left to right during the period; the description given by the same basis set is more accurate at the left of the periodic table.

STO-NG is a basis set unable to describe with the desired accuracy a reactive process. Some limitations of the minimal basis set can be avoided with the use of an extended basis set. This new basis set uses a larger number of contracted Gaussian functions for the description of an orbital. Doubling or tripling the number of functions of a minimal basis set lead to the so-called double- ζ (DZ) and triple- ζ (TZ) basis sets. When only the valence function is a double or tripled the basis set is called split valence (SV). Another improvement of the basis functions is the use of polarization and diffusion functions.

1.1.3.2 Correlation Energy

The analytic solution of the Schrödinger equation for a many electrons system doesn't exist. This problem has led to many approximate methods to calculate wave functions, that could describe the electronic environment inside molecules and atoms, without the exact solution.

The most famous ab initio method is the Hartree-Fock (HF) method. The method solves a pseudo-Schrödinger equation called Fock equation and results in wave functions that are also necessary to build the Fock operator. This paradox is

solved through the iterative calculation with an input wave function derived from more approximate methods. Other theories were developed for the improvement of the HF method like the Roothan-Hall equations which expand each MO in the LCAO approximation or unrestricted Hartree-Fock (UHF) method.

Despite these improvements of the HF method, all of these theories are based on the independent-particle model. This model does not consider explicitly the electron-electron interactions but a mean potential felt by each electron and generated by the surrounding electronic cloud. This error is known as correlation energy and is defined as: $E_{corr} = E - E_{HF}$, where E_{HF} is the limit energy calculated by the Hartree-Fock method and E is the exact eigenvalue of the Schrödinger equation. The correlation energy is about 1% of the total energy of a generic molecular system, its magnitude is the same as the energy involved in a chemical reaction. The computational approach for mechanistic studies can not be affected by an error of this magnitude. Considering a N-electron system, the corresponding Hamiltonian operator is:

$$\hat{H} = \sum_{i=1} \hat{h}_i + \frac{1}{2} \sum_{i=1} \sum_{j=1} \hat{h}_{ij} \quad (1.14)$$

Where \hat{h}_i is the monoelectronic Hamiltonian operator defined as the hydrogen-like Hamiltonian:

$$\hat{h}_i = -\frac{1}{2} \nabla_i^2 + \sum_{j=1} \frac{Z_j}{r_{ij}} \quad (1.15)$$

\hat{h}_{ij} in Eq 1.14 is the Hamiltonian operator which represents the interaction between the i -th and j -th electron. This interaction tends to infinity if r_{ij} is null. This effect is known as “Coulomb’s hole”, the independent particle model neglects this phenomenon because the mean potential is constant and independent from the distance between electrons. The physical meaning of this fact is not negligible because implies a probability different from zero to find two electrons with an opposite spin in the same point of the space. The Pauli’s principle, on the other hand, forbids the analogue phenomenon for electrons with the same spin; this means that the electrons are characterized by a “Fermi’s hole”. HF method considers only the Fermi’s hole thanks to Pauli’s principle but ignore the Coulomb’s hole. The correlation energy could be divided in two contributes:

- internal or structure-dependent correlation energy, for electrons represented by different spatial orbitals. Due to the inappropriateness of the Hartree-Fock model to describe the degeneration or quasi-degeneration of two or more electronic configurations;

- external or dynamic correlation energy associated with the motion of the antiparallel electrons characterized by Coulomb's hole.

The dynamic correlation energy is fundamental during the study of an organic reaction. That is true also because its value changes along the reaction coordinate, due to the reactive process which changes continuously the electronic cloud of the system. This non-linear change implies a non-systematic error, a not negligible error, and it has to be introduced during calculations.

Calculations that contemplate the correlation energy are called post Hartree-Fock methods. Configuration Interaction (CI) method describes the wave function of the system with a linear combination of Slater determinants. These determinants are obtained from the electronic ground and excited states through the permutation of each orbital with each virtual orbital. In the perturbation theory of Møller-Plesset (MP), the perturbation is the lack of the HF model in the description of electronic motion. The most promising method is the Density Functional Theory (DFT), which is the main calculation method adopted in this thesis.

1.1.3.3 Density Functional Theory

The DFT method is a widely employed computational method, thanks to the smaller computational cost also for big molecular systems. DFT results were found in agreement with empirical data: thermochemical information, frequencies, force fields, transition states (TS) structures and NMR interpretation. The success of DFT method is due to its ability to describe the correlation energy with accuracy.

This method is based on the Hohenberg-Kohn theorem which states that all the fundamental state properties of the system are determined univocally by the electronic density $\rho(r)$ and that any other electronic density $\rho(r')$ conducts to an higher energy than the real one. [10] The electronic energy is a functional of electronic density.

$$E = F[\rho(r)] \quad (1.16)$$

where E is the electronic energy, $\rho(r)$ is the electronic density and F is the functional which relates E to $\rho(r)$. The exact form of this functional is unknown, being unknown the exact relationship between E and $\rho(r)$. DFT method aims to a good approximation of the functional or at least of a part of it. The approximation used today is that proposed by Kohn and Sham. Like the HF calculation the Kohn-Sham equations reduce the problem of a multielectronic structure to an

ensemble of mono-electronic orbitals. [11]

$$h_i^{KS} \phi_i(r) = \epsilon_i \phi_i(r) \quad (1.17)$$

where h_i^{KS} is the Kohn-Sham operator, $\phi_i(r)$ are the Kohn-Sham wave functions for the non-interacting particles and ϵ_i is the eigenvalue of energy associated to the eigenfunction $\phi_i(r)$. This equation is similar to the Schrödinger equation, but in this case the electrons are not interacting among them. This is a fictitious system different from a real system but with the same behaviour, and the Kohn-Sham equations' eigenvalues of energy are equal to Schrödinger equations' eigenvalues of energy. The expression of the energy proposed by Kohn and Sham is the sum of different contributors: the kinetic energy (T_k), the electrostatic attraction electron-nucleus (E_{Ne}), the Coulombian term (J) and the exchange-correlation term (E_{XC}).

$$E[\rho] = T_k[\rho] + E_{Ne}[\rho] + J[\rho] + E_{XC}[\rho] \quad (1.18)$$

The electrostatic attraction electron-nucleus (E_{Ne}) and the electrostatic repulsion electron-electron (J) are derivable from an HF calculation. The kinetic energy of an electron from the HF theory to the Kohn-Sham theory instead, has been redefined as:

$$T_k[\rho] = -\frac{1}{2} \sum_{i=1}^N \int \phi_i^*(r) \nabla^2 \phi_i(r) dr \quad (1.19)$$

where $\phi_i(r)$ are the Kohn-Sham non-interacting particles wave functions and are the eigenfunctions of the Kohn-Sham eigenvalue equation (Eq 1.17). Ultimately, the functional expressed in Eq 1.18 is determined less than the exchange-correlation energy (E_{XC}). The representation of this last functional is strictly related to the quality of the DFT calculation. It is possible to define the Kohn-Sham operator as:

$$h_i^{KS} = -\frac{1}{2} \nabla^2 - \sum_{k=1}^{Nn} \frac{Z_k}{|r_i - r_k|} - \int \frac{\rho(r')}{|r_i - r'|} dr' + V_{XC} \quad (1.20)$$

Where V_{XC} is the exchange-correlation term for one electron and is represented as:

$$V_{XC} = \frac{\delta E_{XC}}{\delta \rho} \quad (1.21)$$

Where E_{XC} is the expectation value of the energy for a monodeterminal wave function, solution of the Kohn-Sham eigenvalue equation (Eq 1.17). Being the analytical form of $E_{XC}[\rho]$ not determinable, it is necessary to use some approximations. [12] The most important is to separate this functional into a sum of contributes.

$$E_{XC}[\rho] = E_X[\rho] + E_C[\rho] \quad (1.22)$$

Again, to provide a good description of V_{XC} , different DFT methods have been developed for the calculation of the exchange ($E_X[\rho]$) and correlation ($E_C[\rho]$) functionals. It is the accuracy of these two functionals to determine the quality of the DFT method employed. They are classifiable as local methods, where only the electron density is used, and non-local methods or generalized gradient corrected, where the electron density is used as well as its gradient. Gaussian09 software has some models of this kind of functionals. [13] Other important features are the possibility to build mixed functionals generally expressed in the Gaussian09 series as:

$$a_1 E(S)_x + a_2 E(HF)_x + a_3 E(B88)_x + a_4 E(local)_c + a_5 E(non - local)_c \quad (1.23)$$

where $E(S)_x$ is the Slater exchange functional, $E(HF)_x$ the exchange term of Hartree-Fock, $E(B88)_x$ is the non-local correction for the exchange functional as suggested by Becke [14], $E(local)_c$ is the correlation functional without gradient corrections and $E(non - local)_c$ is the non-local corrected correlation functional. Today, many different functionals, which aim to describe different problems, are available. One of the most famous is the ‘‘hybrid’’ functional introduced by Becke in 1993. [15] This functional is known as B3LYP: in this functional $E(local)_c$, is described as the local correlation functional of Volsko, Wilk and Nusair [16] while $E(non - local)_c$ is given by the Lee-Yang-Parr functional. [17] The coefficients of Eq 1.23 were suggested by Becke [18] and are respectively: $a_1 = 0,80$ $a_2 = 0,20$ $a_3 = 0,72$ $a_4 = 0,10$ $a_5 = 0,81$. This functional has been widely invoked during computational studies. However, it showed some modelling issues:

- the description of the system is better for the principal groups compared to transition metals;
- activation energy is generally underestimated;
- middle-range interactions, such as van der Waals and, π -stacking interactions are not accurately quantified.

These problems led the research in finding better functionals. This goal has been achieved by Zhao and Truhlar, [19, 20] which have developed a new functionals

family called M05, later evolved to M06. Zhao and Truhlar have introduced the uniform electron gas limit and the absence of auto-correlation energy which allows to overcome B3LYP problems. M06 functional family depends on the spin density, the spin density gradient and the spin density kinetic energy. $E(\text{non} - \text{local})_c$ is described with HF exchange functional. Reaction mechanisms in this thesis have been investigated through M06-2X functional. M06-2X is a son of M06 functional family and allows a good description for main group thermochemistry, kinetics and non-covalent interactions.

1.2 Solvent effects

Solvation is a fundamental aspect in organic and bio-organic chemistry affecting kinetics and thermodynamics of chemical reactions. A solvent is a media where the solute is embedded. This media is composed of solvent molecules which interact with the solute and vice versa. Depending on the polarity of the solvent, an electric field (*i.e.* reaction field) is generated. The reaction field polarizes the solute producing an induced dipole moment on it, which induces a dipole moment in the interacting solvent molecules. Since the solvent molecules fluctuate, the induced dipoles fluctuate in turn.

Modelling the solvent effect on a solute can be extremely important to reproduce experimental data properly. There are different ways to model solvation, here briefly described. Explicit solvation describes the solvent effect on the solute by considering solvent molecules explicitly. In this way, all the solute-solvent interactions can be described through the interaction between all the pairs of atoms, one belonging to solvent and the other one belonging to the solute. MM methods take advantage of the classic description of the system to use explicit solvation. Solvation is the most expensive process to be calculated. When solvent molecules are considered, the number of interactions increases dramatically. Specialised force fields for solvent molecules, to reduce the computational cost, have been developed for MM approach. An example is the popular triangulated water (TIP3P) model that keeps the H-O-H angle and O-H bonds fixed in order to delete the energetic contributions due to the water proton vibrations.

While for MM computations explicit solvent computations are, most of the time, feasible, it is nearly impossible to treat all the solvent molecules at QM level. This approach is practicable only if a few solvent molecules located in the first solvation sphere (micro-solvation) are considered.

1.2.1 Continuum Medium Models

A much simpler approach, known as the "continuum medium method", is to approximate the solvent to a uniform and polarisable continuum characterised by its dielectric constant ϵ_r , which is measurable. Within this approximation, the interaction between the solute and the solvent is calculable. In QM computations, the solute charge distribution $\sigma(r_s)$, which is affected by the dielectric medium, is obtained from the wave-function of the system. Subsequently, the new solvent-polarised charge distribution $\sigma'(r_s)$ polarises the medium so that the equation must be solved iteratively. This procedure is known as Self-Consistent Reaction Field (SCRF).

To model the solvation process, special attention needs to be given to the solute cavitation in the medium. The simplest approach creates a spherical or ellipsoidal cavity, but with this description, the solute-solvent interaction is not accurately described (Figure 1.1.a). More accurate models reproduce the molecular shape of the solute using van der Waals (VDW) radii or a scaled VDW radii, by which VDW-surfaces (VDWS) are created (Figure 1.1.b) This description still has some deficiencies since the valleys and pockets of the external cavity may not be sufficiently wide to accommodate at least one molecule of the solvent. To improve this approach, Solvent-Accessible Surface (SAS) is used. The surface (and hence the cavity) is obtained by rolling a probe of the size of the solvent along the VDWS (Figure 1.1.c).

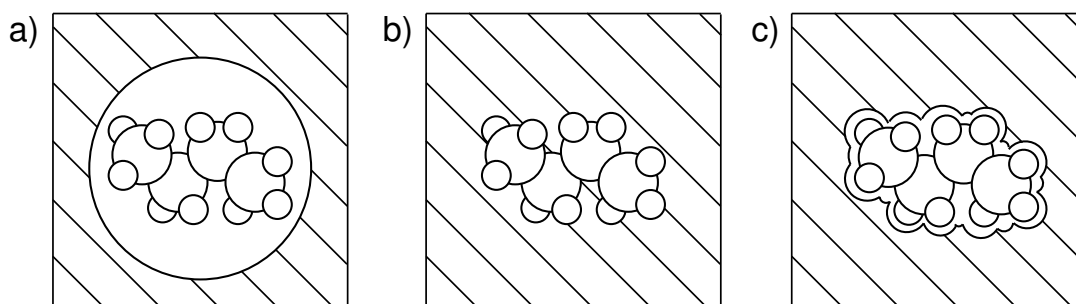


Figure 1.1: Schematic representation of the cavity shapes formed in the medium to accommodate the solute. In particular, the surface described by a) spherical cavity, b) VDW radii, c) solvent-accessible surface.

Various continuum models differ in the description of the cavity's shape and size, the charge distribution of the solute and how the dielectric medium is described. The Osanger model employs a spherical (or ellipsoid) cavity while the charge distribution of the solute is expressed in terms of a dipole (or multipole) expansion. The Tomasi's polarised continuum model (PCM) [21] has a cavity based on the VDWS, where the VDW radius is scaled by a value of 1.2 and the electrostatic interactions are calculated via SCRF. Various PCM versions are

available; in particular, the Integral Equation Formalism-PCM (IEF-PCM) is the solvation model adopted for all the QM computations reported in this thesis when solvent effects are taken into account. In particular, IEF-PCM has been used to model water solvation during the investigation of the reaction mechanism of deoxyribozyme 9DB1 (Chapter 4). IEF-PCM model is implemented in Gaussian09 software, [13] the program used to carry out all the QM and QM/MM investigations reported in this thesis.

Solvation modelling is also important to estimate the solvation free energy, solvent's degrees of freedom are taken into account implicitly. The energy of a molecule in a solvent is:

$$E_{tot} = E_{vac} + \Delta G_{solv} \quad (1.24)$$

where the solvation free energy ΔG_{solv} can be roughly described by

$$\Delta G_{solv} = \Delta G_{elec} + \Delta G_{non-polar} \quad (1.25)$$

The ΔG_{elec} accounts for electrostatic interactions, and is the most demanding calculation, while $\Delta G_{non-polar}$ adds the contributions due to the ‘‘hydrophobic’’ interactions, which are van der Waals interactions and the cavitation cost of the solute in the medium. These two contributions that form ΔG_{elec} are approximated to be proportional to the SAS area (SASA). To obtain the $\Delta G_{non-polar}$ one can solve the Poisson equation (Eq. 1.26), which provides the electrostatic potential $\phi(r)$ which is generated by the molecule charge distribution $\sigma(r_s)$:

$$\nabla[\epsilon(r)\nabla\phi(r)] = -4\pi\rho(r) \quad (1.26)$$

where $\epsilon(r)$ is the dielectric constant of the solvent that depends on the position. From Poisson's equation it is possible to derive the Poisson-Boltzmann equation. $\rho(r)$ as composed by the solute charge density $\rho_f(r)$ and a contribution from the ions in solution $c(r)$. For N ion species with charge and bulk concentration, the ion charge distribution is given by:

$$c(r) = 4\pi \sum_{i=1}^N q_i c_i^\infty e^{-\beta q_i \psi(r)}; \beta = k_b T^{-1} \quad (1.27)$$

with the separation in its contributes $\rho(r)$ is also explicit by substituting 1.27 into 1.26 and by following steps considering electrostatic neutrality, expanding the expression function as a Taylor series, the linearised Poisson-Boltzmann equation

is obtained:

$$\nabla[\epsilon(r)\nabla\phi(r)] - 8\pi q^2 c^\infty \beta\psi(r) = 4\pi\rho(r) \quad (1.28)$$

in order to solve this equation, various numerical methods can be employed. For obtaining the polar term of solvation Gibbs free energy AMBER [22] adopts the method of the finite difference which allows to divide the space in a three dimensional grid and map the charge generated by atoms inside this grid. The Poisson-Boltzmann equation has to be solved both in the solvent and in vacuum with the respective dielectric constants. With the solution is possible to know the polar term of solvation Gibbs free energy:

$$\Delta G_{elec} = \frac{1}{2} \sum_{i=1} q_i (\phi_i^{solv} - \phi_i^{vac}) \quad (1.29)$$

where q_i is the charge assigned to a grid point. ϕ_i^{solv} and ϕ_i^{vac} are the potentials in the same point but in different environment, water and vacuum respectively. Other than PB model, Generalised Born (GB) model provide an implicit solvent. This model is an approximation of the approximate PB solvent model. The expression of the polar term for the solvation Gibbs free energy is now described as the summation of the atomic charges multiplied to g_{ij}^{GB} .

$$\Delta G_{elec} = \frac{1}{2} \sum_{i,j \in X} q_i q_j g_{ij}^{GB} \quad (1.30)$$

g_{ij}^{GB} as an analytic expression for its functional form:

$$g_{ij}^{GB} = \left(\frac{1}{\epsilon} - 1 \right) \left[r_{ij}^n + B_{ij} \exp\left(- \frac{r_{ij}^n}{AB_{ij}} \right) \right]^{-\frac{1}{n}} \quad (1.31)$$

where B_{ij} is a parameter which depends on the distance from the solute-solvent dielectric boundary of atom i - th and j - th and the shape of the entire bio-molecule. A and n have a preset value.

The final step for the calculation of the solvation Gibbs free energy is to determine the non polar term. This term is the sum of two terms: a van der Waals interaction represented by its contribute in term of variation of Gibbs free energy and the energetic cost for generating a cavity in the solvent by the solute.

$$\Delta G_{non-polar}^{solv} = \Delta G_{non-polar}^{vdW} + \Delta G_{non-polar}^{cav} = \gamma SASA + \beta \quad (1.32)$$

Where β and γ are parameters depending on the method employed, SASA is the solvent accessible surface area.

GB solvation model has been used to model water solvation during MD simulations of deoxyribozyme 9DB1 (Chapter 4)

1.3 Molecular Dynamics

Molecular dynamics is a method that produces the evolution of a molecular system during time. The initial assumptions are to describe atoms like rigid spheres and bonds like oscillators defined by harmonic potentials. By solving Newton's equation of motion, the trajectory of the atoms is quantifiable generating a displacement during time.

1.3.1 Force Field

From Newton's second law: $F = ma$ which is in the case of MD simulation a many bodies problem, where each body is an atom of known mass; it is necessary to know the applied force to calculate the acceleration produced on it. Considered this, to calculate the position of the i -th atom as a function of time t , it is necessary to solve Newton's second law for each atom and explicit the meaning of acceleration or the second derivative of position with respect to the time:

$$F_i = m_i a_i = m_i \frac{d^2 r_i}{dt^2} \quad (1.33)$$

The force acting on each atom is also derivable from the potential, as the negative of the derivate of potential energy ($-\frac{\delta V}{\delta r_i}$) with respect to the position of the atom. Thanks to this relationship, through the potential energy of a given system, it is possible to know, if are known the starting coordinates, initial velocities and, the forces acting on atoms; which also means the acceleration and the position after a time step. If the trajectories of the atoms are deductible from the potential energy, it is evident the necessity of a good description of the potential energy. To have a good potential energy function, it is possible to separate this function in a sum of functions for each contribution, due to the additivity principle:

$$\begin{aligned} V = & \frac{1}{2} \sum_{i=1}^{N_b} k_i^b (r_i - r_{0,i})^2 + \frac{1}{2} \sum_{i=1}^{N_\theta} k_i^\theta (\theta_i - \theta_{0,i})^2 + \frac{1}{2} \sum_{i=1}^{N_\xi} k_i^\xi (\xi_i - \xi_{0,i})^2 \\ & + \frac{1}{2} \sum_{i=1}^{N_\phi} k_i^\phi \cos[(\phi_i - \phi_{0,i})] + \frac{1}{4\pi\epsilon_0} \sum_{i=1}^{N_q} \sum_{j<i}^{N_q} \frac{q_i q_j}{r_{ij}} + \sum_{i=1}^{N_a} \sum_{j<i}^{N_a} \left(\frac{A_{ij}}{r_{ij}^{12}} - \frac{B_{ij}}{r_{ij}^6} \right) \end{aligned} \quad (1.34)$$

the first four terms represent respectively bonds, angles, dihedral and improper angles which are the interactions inside molecules or *bonded* interactions. The

last two terms represent electrostatic interactions and van der Waals interactions which are *non-bonded* interactions. These interactions do not depend on a defined number of bonds. Local interactions are represented in classical terms by harmonic potentials for stretching, bending and variation of improper angle ξ_i . Generally, bond and angle contributions are considered frozen at room temperature, due to their high energy constants. The dihedral angle is the most important function that represents a local interaction without harmonic potentials. Moreover, this is the only one which has a significantly low constant.

Non-local interactions are represented by Coulomb and van der Waals potentials. Coulomb potential is simply the homonym law extended to each charge. Van der Waals potential conversely has not a theoretical law but only an empiric description. A good one is the Lennard-Jones potential, the last term of the Eq. 1.34. The potential energy of Eq 1.34 gives the functional form of the force field which describes the behaviour of a system. The next step is to set the parameters which describe potentials properly. Generally, this is done with either empirical data and theoretical calculations. This way to model the system necessarily implies a library of parameters.

In this thesis work MD simulations have been performed with Assisted Model Building with Energy Refinement (AMBER) force field. [22]

1.3.2 Verlet Method

From the potential energy expression, it is derivable the force acting on a particle. This force allows calculating the acceleration, hence, the position as a function of time. A MD simulation is the solution of Newton's equations of motion iterated for each time-step. To solve this equation it is used the Verlet method which starts with the Taylor expansion of the position:

$$r(t + \delta t) = r(t) + v(t) + \frac{1}{2}a(t)\delta t^2 + .. \quad (1.35)$$

$$r(t - \delta t) = r(t) - v(t) + \frac{1}{2}a(t)\delta t^2 - .. \quad (1.36)$$

Adding these two expansion gives:

$$r(t + \delta t) = 2r(t) - r(t - \delta t) + a(t)\delta t^2 + .. \quad (1.37)$$

By substituting Newton's second law in Eq. 1.37, it is obtained an expression of the future position which depends on the actual and old position and also by the force applied. Now it is possible to estimate the value of velocity using the

position terms and the mean value theorem.

$$r(t + \delta t) = 2r(t) - r(t - \delta t) + \frac{F(t)}{m} \delta t^2 \quad (1.38)$$

$$v(t + \delta t) = \frac{r(t + \delta t) - r(t - \delta t)}{2\delta t} \quad (1.39)$$

Eq. 1.38 and 1.39 provide atomic positions and velocities during time from the starting coordinates. These pairs of information are the trajectory of atoms. MD simulation is the iteration of the Verlet method. This algorithm provides a useful tool to predict the position of each atom in a determinate instance.

1.3.3 Approximations Inside Molecular Dynamics Simulations

Besides the implicit approximation inside MD simulation, which is a MM method, other approximations are adopted to have a good compromise between the computational demanding and the quality of the result.

A bulk component like solvent requires an enormous number of molecules to be described correctly. The calculation related to a number of Avogadro of molecules is a computational cost impossible to pay. A MD simulation uses box of solvent with a lower number of solvent molecules. To give a better representation of a solvated system, periodic boundary conditions are used. This method consists in the generation of a finite box solvent with its translation for filling the space. Each particle of a box, moves united with the same particle that belongs to the original box. When a particle moves out of the box, it is replaced by the image of the same particle which enters from the opposite side, as if it is coming out from the box behind.

An important component of the computational cost is due to non-local or non-bonded interactions. The reason resides in the definition of this kind of interactions which are defined by non local potentials. With this definition for quantifying this potential is required to sum every combination of interacting atoms. In particular, van der Waals forces are applicable to each pair of atoms and the corresponding Lennard-Jones potential could be a serious problem for the calculation. Being this potential proportional to r^{-6} , if between two atoms the distant is significant, Lennard-Jones potential is negligible. This fact allows to put a cut-off distance beyond that potential is considered inexistent.

The last important approximation is focused on the other non-local interaction, the electrostatic interaction described by Coulomb's law. In this case, instead of van der Waals interaction, the dependence with the distance is less negligible

being proportional to r^{-1} . The Ewald summation method allows a rapid calculation of this interaction by replacing the direct summation of the interaction energy between two particles with the sum of two terms: short-range potential and long-range potential. The short-range potential is calculated in real space, the long-range potential is calculated in the Fourier space allowing a faster and cheaper calculation. The Ewald summation allows calculating the electrostatic interaction even when a cut-off is imposed.

Even using these approximations, today the computational demanding for this kind of calculation limits the time scale in the order of hundreds of nanoseconds. For observing some properties, that could not be observable in the macroscopic reality of an experimental laboratory, this is an excellent tool if the force field provides a good parameterisation of the system.

1.4 Hybrid Quantum Mechanics/Molecular Mechanics Methods

The hybrid approach Quantum Mechanics/Molecular Mechanics (QM/MM) is a simulation method which relates quantum and molecular mechanics. QM methods are fundamental to describe reactive processes. The problem is to calculate the electronic structure of big systems which are too expensive to be described with a pure QM approach. In 1976 Warshel and Levitt published one of the first studies about the QM/MM approach for a biological *host-guest* system. [23] The binding site description is carried out at the QM level while the remaining structure and the solvent is described at the MM level. The idea is to describe only the atoms directly involved in quantum processes with a QM approach.

Figure 1.2 gives a qualitative idea of the system partitioning into subsystems. The overall system (*Real*) is partitioned into a model system (*Mod*), which is described with QM methods and an outer region, the surrounding environment (*Env*), which is described with MM methods in terms of force field.

1.4.0.1 Energy of a QM/MM system

The total energy (E_{tot}) of a QM/MM system is composed by different contributions, calculated at different level of theory *i.e.* QM and MM levels. E_{tot} can be calculated with two different methods called the *additive* (Eq. 1.40) and the

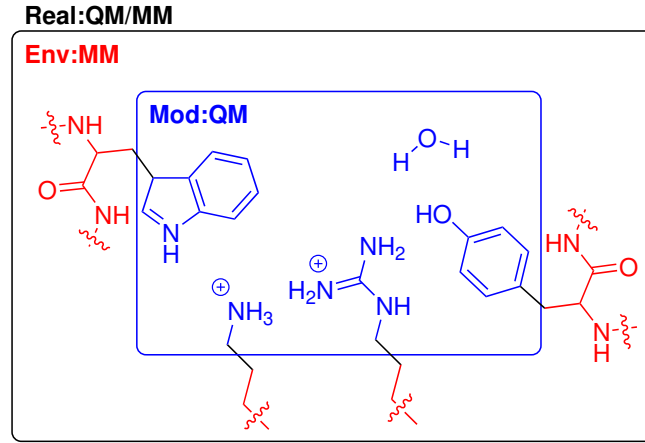


Figure 1.2: The entire system (*Real*) is partitioned into a model system (*Mod*) and an environment (*Env*). *Mod* is described with QM approach *Env* is described with MM approach.

subtractive (Eq. 1.42) method.

$$E_{QM/MM}^{Add} = E_{QM}^{Mod} + E_{MM}^{Env} + E_{QM/MM}^{Int} \quad (1.40)$$

Where E_{QM}^{Mod} is the QM energy of the model system calculated with QM methods, E_{MM}^{Env} is the MM energy derived from the force field of the environment and $E_{QM/MM}^{Int}$ is the interaction energy between the MM and the QM system. The additive scheme calculates the energy as the sum of the model system energy, obtained from quantum calculations, and the environment energy, obtained from the related force field. Moreover, an explicit coupling term to describe the interaction between the model (*Mod*) and the environment (*Env*) subsystems ($E_{QM/MM}^{Int}$) is required. This term includes bonded, van der Waals and electrostatic interaction (Eq.1.41).

$$E_{QM/MM}^{Int} = E_{QM/MM}^{Bonded} + E_{QM/MM}^{vdW} + E_{QM/MM}^{elec} \quad (1.41)$$

The *subtractive* scheme (Eq. 1.42) approaches the problem calculating the MM energy of the entire system (*Real*) and both QM and MM energy of the model system. In this way, the total QM/MM energy can be calculated as in Eq. 1.42.

$$E_{QM/MM}^{Sub} = E_{MM}^{Real} - E_{MM}^{Mod} + E_{QM}^{Mod} \quad (1.42)$$

Where E_{MM}^{Real} is the MM energy of the real system, E_{MM}^{Mod} and E_{QM}^{Mod} are the MM and QM energies of the model system. In contrast with the additive scheme, the subtractive scheme does not need an explicit coupling term. The coupling term is defined only at the MM level because the MM description is carried out on the real system and then, the MM energy of the model system is subtracted. The

subtractive scheme can be viewed as an MM approach where a system portion has been treated with the QM approach. Coupling terms between the different levels are not required. However, the force field parameters for the MM description needs to be accurate to reproduce the QM potential in the model system. As an example of a subtractive QM/MM scheme, is the IMOMM (integrated molecular orbital/molecular mechanics) developed by Morokuma and co-workers. [24] IMOMM implementation led the possibility to combine two QM methods (IMOMO [25]) and further generalized to n layers (typically, $n = 3$), all describable at the desired level of theory (QM or MM) (ONIOM, our n-layered integrated molecular orbital and molecular mechanics [26, 27]).

In this thesis, the subtractive method is the one used (Eq. 1.42). Where E_{MM}^{Real} is the total energy of the overall system under investigation (real system) described with its force field. E_{QM}^{Mod} is the energy of the model system where a QM approach is used to describe this subregion of the real system while E_{MM}^{Mod} is the same subregion described with the force field.

1.4.0.2 Electrostatic QM/MM Interactions

Differently from the additive method defined as in Eq 1.40, coupling terms which include the interaction between QM and MM regions are not specified. The subtractive method allows to calculate the interaction energy between QM and MM regions in three different ways:

- mechanical embedding;
- electrostatic embedding;
- polarized embedding.

Mechanical embedding considers the effect of the MM environment through the interaction with the MM model system. Although the real system naturally takes into account the model system, this interaction energy is described in terms of force field. This approach neglects the polarizability of the model system other than special force field which can be polarized by means of additional parameters. Electrostatic embedding, in addition to the QM/MM interactions included in the model system by means of force field, adds an interaction term in the QM hamiltonian. In this way, the model system electron density can be polarized by the surrounding charges also at the QM level. This implementation can provide better results.

It is straightforward to improve the method by introducing variable MM charges. A polarizable MM model allows taking into account the effect of the QM electron density on the MM environment. This is the polarized embedding scheme.

1.4.0.3 The Boundary region

In the easiest case, the QM and MM regions are not bonded ($E_{QM-MM}^{Bonded} = 0$). This is the case of solvation processes or reactions inside nanocontainers. A solute immersed in the solvent, or, as in this thesis work (Chapter 3), a reactant system that undergoes a chemical reaction inside a carbon nanotube. When $E_{QM-MM}^{Bonded} \neq 0$, due to a covalent bond between an atom described with QM methods and another one described with MM methods, the situation becomes more difficult. Enzymatic reaction, where the catalytic residues have their backbones with the MM region often display this situation.

A straightforward cut of “bridging” bonds would generate an open valence on the QM atom and hence, an alteration in the model subsystem wave-function. To deal with the boundary problem, three different schemes have been proposed:

- link-atom schemes introduce an additional atomic centre which cap the model system (usually a hydrogen atom). This cap is not part of the real system. It is covalently bound to saturate the free valency generated by the cut;
- in boundary-atom schemes, the MM atom in the cut bond is replaced by a special boundary atom that appears in both the QM and the MM calculation. On the QM side, it mimics the cut bond and possibly also the electronic character of the MM moiety attached to QM atom; in the MM calculation it behaves such a normal MM atom;
- localized-orbital schemes place hybrid orbitals at the boundary and keep some of them frozen. Is an alternative way to cap the cut bond instead of the link-atom scheme.

Oriented External Electric Fields

The design of new catalysts is of utmost importance in chemical reactivity. In principle, catalysts should be considered as add-on molecular units that are capable of reducing the activation barrier required by a given reaction and, thus, speed up the reaction rate, without being apparently involved in the process. Nowadays, this effect can be obtained in less conventional and more subtle ways: with nanoreactors [28], microwaves [29], ultrasounds [30], mechanical stress [31], which are all examples of recently proposed techniques that can be used to control the course of a reaction.

During the last decade in a few labs around the world an unusual new idea came to light: can an Oriented External Electric Field (OEEF) applied to reactants modify kinetics and thermodynamics of reactions? Since reactions are the results of electrons and nuclei motion, it is not odd to expect that activation barriers can be affected by an external field. This idea is consistent with the hypothesis of electrostatic catalysis occurring within the enzyme active sites. [32] The arrangement of the atoms provides a pre-organized polar environment, which originates an electric field that stabilises transition states, thus determining the catalytic rate enhancement of enzymes. Warshel and co-workers demonstrated that such stabilization is stronger than that determined by the water environment [33].

A similar problem was faced by Shaik and co-workers who, for the first time, undertook a systematic exploration of OEEFs effect on non-polar and non-redox organic reactions using a computational approach [34–40]. Shaik examined several non-redox organic reactions showing that an OEEF applied along the direction of the major electron reorganization (reaction coordinate) can significantly catalyze the reactions and control the regioselectivity and stereoselectivity [37–40]. Shaik

called it "reaction axis". It is possible to see the reaction axis as the dipole contribution to the reaction coordinate, which drives the interaction of the system with OEEF, *i.e.* the shape and the energy of the reaction profile. More qualitatively, the reaction axis can be seen as the net direction of the electron flow during a reaction.

In 2004 Shaik and co-workers carried out a first computational investigation on the effects of electric fields on the selectivity of two competing reactions involving propene, *i.e.* C-H hydroxylation vs C=C epoxidation. [34] The reaction was promoted by a heme unit (found in many metal-enzymes, such as the Cytochrome P450 family) formed by a porphyrin with Fe–O bound in the middle of the ring along its axis. In Shaik's model, this compound was binding the propene molecule and the electric field was applied along Fe–O bond. He found that the choice of the orientation of the field favors a complete C–H hydroxylation or a complete C=C epoxidation. In a subsequent paper, he carried out a systematic study at the QM/MM level of the effects of an external electric field on the catalytic cycle of P450cam (CYP101). [35] The results obtained in these preliminary works suggested that the subject was worth exploring. Thus, Shaik and co-workers examined one of the most popular organic reactions, the Diels-Alder reaction, and found that an electric field catalyzes the reaction (it is accelerated 4-6 times) and affects its endo/exo selectivity. [36] Aragoes and co-workers provided experimental evidence that non-redox reactions such as the Diels-Alder cycloaddition is accelerated by an OEEF, confirming the theoretical results previously obtained. [41]

During the last decade, other research groups around the world have examined either experimentally or theoretically the effects of external electric fields on structures, properties and reactivity of molecules. [41–48] Nowadays, the use of electric fields has been accepted as one of the possible tools to manipulate chemical processes, modifying the reaction activation barriers (catalysis), but also changing the mechanism and the outcome of a reaction. The major experimental problem concerning this approach, is to supply a strong enough electric field and, at the same time, control the orientation of molecules within the applied field. This was achieved using different techniques. In particular the experiment of Garcia et al. [44] based on AFM or Aragoes et al. [41] and Zhang et al. [47], based on STM, paved the way for the extensive use of OEEF to accelerate chemical reactions.

2.1 Computational Methods

All computations were carried out with Gaussian09 [13] software using the DFT M06-2X functional and the 6-311++G** basis set. [20] The structure of the various critical points (minima and saddle points) was fully optimized. Frequency calculations were carried out at the same level of theory to assess the nature of critical points. Atomic partial charges were evaluated with the natural bond order (NBO) population analysis. [49, 50] The effects of the OEEFs were studied in the range $\pm 15.0 \times 10^{-3}$ a.u., using the “Field=M±N” keyword, which defines orientation and magnitude of the applied field in Gaussian09 [13]. The field intensity unit N is:

$$N \times 10^{-4} \text{a.u.} = N(5.14 \times 10^7) \text{Vm}^{-1} = N(5.14 \times 10^{-2}) \text{Vnm}^{-1} \quad (2.1)$$

To understand the effects of an OEEF on the molecular energy E , the following expression derived from perturbation theory is used:

$$E = E(0) - \mu_0 F - \frac{1}{2} \alpha F^2 \quad (2.2)$$

where $E(0)$ is the energy in the absence of electric field, μ_0 is the permanent (intrinsic) dipole in the direction of the applied field F and α is the polarisability in the same direction. In the presence of an isotropic field, the polarisability is a scalar quantity that describes the tendency of the molecular electron cloud to be displaced and distorted by the external electric field (applied along a given direction). Charge distortion results in a modification of the intrinsic molecular dipole. The resultant induced dipole μ can be approximately expressed as the sum of the permanent dipole μ_0 and the product between polarisability α and electric field F :

$$\mu = \mu_0 + \alpha F \quad (2.3)$$

Using Eq. 2.3 to write Eq. 2.2 leads to Eq. 2.4:

$$E = E(0) - \mu F + \frac{1}{2} \alpha F^2 \quad (2.4)$$

Eq. 2.4 shows that retaining only the first-order contribution in the induced dipole moment expression, allows to estimate the effects of the applied field on the molecular energy.

The induced dipole is an overall parameter reflecting the total effect of molecular charge polarization due to the applied field. This parameter takes into account: (i) the effect of the field on the HOMO-LUMO energy gap and the consequent charge transfer involving the two orbitals, which leads to stabiliza-

tion/destabilization of the transition state (orbital contribution) and (ii) the effect of the field on atomic charges on passing from reactant to transition state (electrostatic contribution). However, the interpretation of the field effect on the energy barrier in terms of HOMO-LUMO energy gap and atomic net charge variation, is not obvious. This is because the final overall effect of the applied field is a complex interplay of orbital and electrostatic contributions and it is usually very difficult to envisage what the dominant factor is.

The energy of the system depends on the induced dipole moment. However, the dipole moment of charged systems depends on the chosen reference system. Considering a system composed by two point charges q_1 and q_2 with position r_1 and r_2 , respectively, in a monodimensional system as in Figure 2.1:

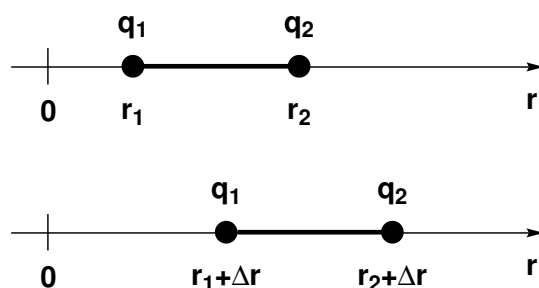


Figure 2.1: Two charges q_1 and q_2 with position r_1 and r_2 respectively (On top). The same system after a rigid translation Δr (On bottom).

the dipole moment (μ) of the system is defined as:

$$\mu = q_1 r_1 + q_2 r_2 \quad (2.5)$$

If the system is translated by a distance Δr the dipole moment is redefined as:

$$\mu' = q_1(r_1 + \Delta r) + q_2(r_2 + \Delta r) \quad (2.6)$$

$$= q_1 r_1 + q_2 r_2 + \Delta r(q_1 + q_2) \quad (2.7)$$

$$= \mu + \Delta r(q_1 + q_2) \quad (2.8)$$

If $q_1 + q_2 \neq 0$, then $\mu' \neq \mu$. Along the reaction coordinate, the dipole moment of charged systems would vary unsystematically. To deal with this modelling issue, after optimising systems with non-zero charge (*i.e.* $\text{MeCl} + \text{Cl}^-$ is a system with net charge -1), the origin of the system was translated into the charge centre. Subsequently, in this new coordinate system, a single point calculation is carried out. In this way, energies and molecular dipoles of all critical points are consistent.

2.2 Substitution Reactions

2.2.1 Introduction

The bimolecular substitution reaction (S_N2) is a fundamental type of reaction mechanism in organic chemistry. Substitution reactions are generally classified as polar reactions.

S_N2 mechanism can occur *via* two different pathways with different stereochemistry; the well-known *back-side* attack with Walden inversion of configuration and the less common *front-side* attack with retention of the configuration. This second pathway leads to a hindered transition state structure which can not handle the steric hindrance. The carbon atom, where the nucleophilic attack occurs, becomes pentavalent. *Back-side* mechanism maximises the distance between the entering nucleophile (Nu) and the leaving group (LG, Figure 2.2).

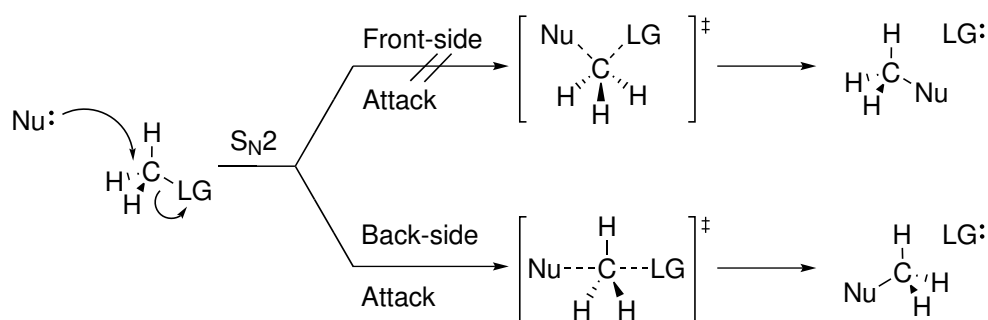


Figure 2.2: Possible S_N2 mechanism: a *front-side* attack mechanism (unfavoured) and a *back-side* attack mechanism (favoured)

Moreover, two main types of S_N2 exist: type I S_N2 where both nucleophile and leaving group are uncharged, and type II S_N2 reaction, where reactants are neutral and products are charged.



Both type I and type II S_N2 reactions can undergo either *back* or *front-side* mechanisms. In addition to the stereochemical aspects of the S_N2 reaction, both type I and type II substitutions can be strongly affected by the polarity of the environment which acts as an external perturbation. This perturbation can be non-symmetrical along the reaction coordinate, *i.e.* reactants, transition state and products can be differently affected by the same perturbation. The intensity of this perturbation also depends on the structure of Nu and LG. Nonetheless, the geometrical rearrangement of the system during the reaction, for type II

S_N2 , implies also a charge separation process (uncharged reactants and charged products). This aspect of type II S_N2 reaction makes it more sensitive to the polarity of the environment, compared to type I S_N2 .

Electrostatic aspects are therefore fundamental to describe substitution reactions. This correlation can be related to the dependence of the reaction profile on the solvation medium, having important consequences on the reaction profile.

These argumentations support the interest in the investigation of OEEF effects on these types of S_N2 reactions. In this way is possible to establish a comparison of the field-effect in relation to S_N2 reaction profile shape and hence, a better comprehension of the OEEFs effects on S_N2 mechanisms. In particular, this investigation is focused on:

- OEEFs effects on the kinetics and the stereochemistry of S_N2 mechanisms.
- OEEFs effects on both type I and type II S_N2 reactions.

2.2.2 Results and Discussion

2.2.2.1 Type I Substitution Reactions

To investigate the effect of OEEFs application on a type I S_N2 , a model reaction is required. The reaction between methyl chloride and chloride anion is a prototype of type I S_N2 reaction.



The reaction profile of this reaction is a symmetrical potential energy curve where reactants and products are equivalent (Figure 2.3).

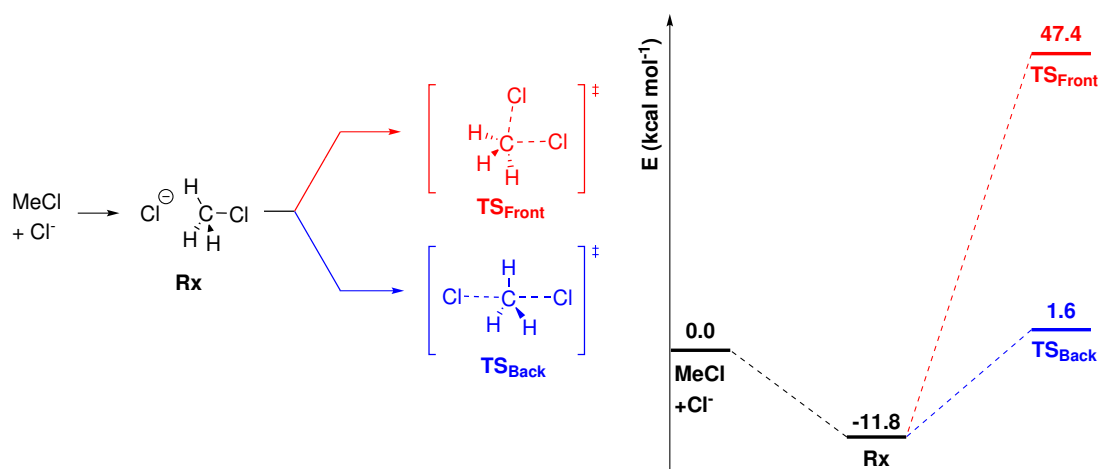


Figure 2.3: *Back* and *front-side* S_N2 mechanisms with their computed gas-phase profiles (kcal mol⁻¹) for the preliminary complex **Rx** and transition states (**TS_{Back}**, in blue lines and **TS_{Front}**, in red lines).

The approaching nucleophile Cl^- forms a preliminary complex (**Rx**) followed by a transition state for the configuration inversion (*back-side* mechanism, **TS_{Back}**) or retention of configuration (*front-side* mechanism, **TS_{Front}**).

The minimum (**Rx**) is governed by the alignment of the dipole moment of methyl chloride molecule with the chloride anion in a linear complex laying $-11.8 \text{ kcal mol}^{-1}$ lower than the asymptotic limit of the isolated reactants. The global barrier (the energy difference between the transition state energy and the asymptotic limit, $\Delta E_{\text{Glob}}^\ddagger$) is $1.6 \text{ kcal mol}^{-1}$ with an internal barrier (the energy difference between the transition state energy and the previous minimum, the reactant complex, $\Delta E_{\text{Int}}^\ddagger$) of $13.4 \text{ kcal mol}^{-1}$. Then, the *front-side* mechanism has been evaluated, finding that bent complexes for both reagents and products are absent and the global barrier ($\Delta E_{\text{Glob}}^\ddagger$) is $47.4 \text{ kcal mol}^{-1}$ with an internal barrier ($\Delta E_{\text{Int}}^\ddagger$) of $59.2 \text{ kcal mol}^{-1}$. **Front-side mechanism is forbidden with respect to the back-side mechanism by $45.8 \text{ kcal mol}^{-1}$.**

To investigate the effects of OEEFs, the various critical points along the reaction pathway have been reassessed. Structures were fully re-optimized in presence of different OEEFs in terms of intensity and orientation. To carry out this investigation it was necessary to build a coordinate system which defines the orientation of molecules and electric fields.

In Figure 2.4 the critical points and their related Cartesian systems are depicted.

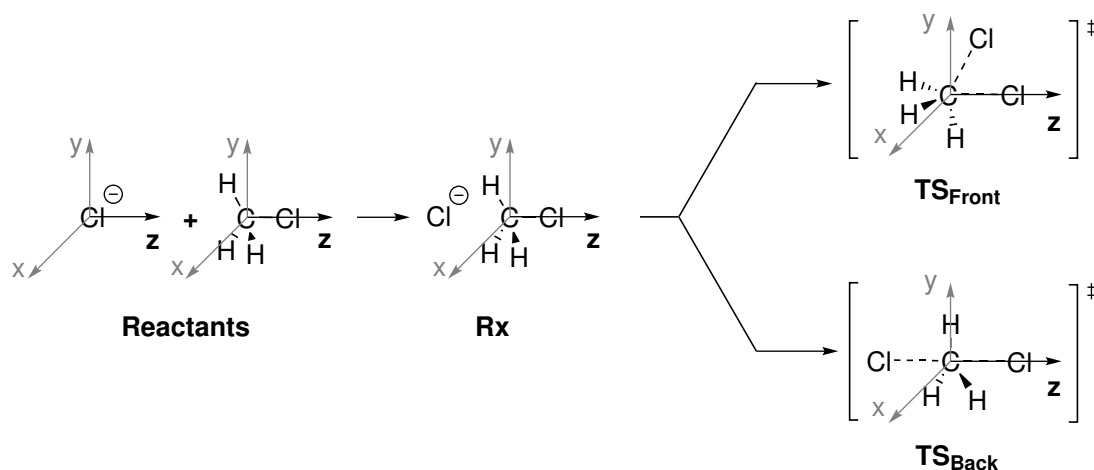


Figure 2.4: The x,y,z-directions of Reactants, **Rx**, **TS_{Back}** and **TS_{Front}** for the chlorine exchange reaction between methyl chloride and chloride anion.

Reactants. In Table 2.1 some important chemical-physical properties are reported such as: bond lengths, partial charges and relative energies of the reactant structures investigated under the perturbation of OEEFs. Fields are applied along the z -axis, in the scanned range of field intensities $R(F_z, 10^{-3} a.u.) = [-12.5; 12.5]$,

as defined in Figure 2.4.

	$(F_z, 10^{-3}a.u.)$	-12.5	-10.0	-5.0	0.0	5.0	10.0	12.5
	E (kcal mol ⁻¹)	4.9	4.2	2.4	0.0	-2.9	-6.2	-8.1
MeCl	R(C-Cl) (Å)	1.77	1.78	1.78	1.79	1.79	1.80	1.81
	q(C) (<i>a.u.</i>)	-0.57	-0.57	-0.56	-0.55	-0.54	-0.52	-0.52
	q(Cl) (<i>a.u.</i>)	-0.01	-0.02	-0.05	-0.07	-0.10	-0.13	-0.14
Cl ⁻	E (kcal mol ⁻¹)	-0.7	-0.5	-0.1	0.0	-0.1	-0.5	-0.7

Table 2.1: Bond length (R) and partial charges (q) of methyl chloride, at different intensities of the OEEF along the z-axis. Relative energies of methyl chloride and chloride anion (E) refer to the unperturbed state.

Analysing Table 2.1, an OEEF oriented along the molecular dipole enhances charge separation and increases bond length while an OEEF with the opposite direction gives the opposite trend for these parameters. When an OEEF is oriented as the molecular dipole, the energy with respect to the unperturbed system decreases, while it increases when the orientation is the opposite.

The difference between the methyl chloride energy under the influence of an OEEF F_z and $-F_z$, can be conceived as the reorganisation energy (E_{Reorg}). A free system, under the influence of OEEF, will orient itself to maximise the stabilising interaction. And, to do that, it will orient its dipole moment parallel with respect to the OEEF direction. The opposite orientation can be kept by paying E_{Reorg} defined as:

$$E_{Reorg} = E_{MeCl}^{F_z} - E_{MeCl}^{-F_z} \quad (2.9)$$

So, E_{Reorg} is the energy required to keep methyl chloride (and more generally a molecule) oriented not in its more stabilised orientation, under the influence of an OEEF (F_z in the present case).

Reactant Complexes. Reactant complexes were fully re-optimised in the presence of OEEFs, but **Rx** structure is unstable at high field values. In particular, **Rx** was optimised as a minimum only at $F_z = 5.0 \times 10^{-3}a.u.$ When $F_z > 5.0 \times 10^{-3}a.u.$, **Rx** is no more a minimum and the chloride anion motion to the positive pole overcomes the anion-dipole interaction, breaking the structure of **Rx**.

When $F_z < -5.0 \times 10^{-3}a.u.$, **Rx** undergoes chloride anion inversion of trajectory, moving to the positive pole along the z-axis. To find a stable structure at negative field values, a new **Rx** was hypothesized (**Rx2**). **Rx2** is a linear complex with the chlorine atom Cl¹ located beyond Cl², on the z-axis (Figure 2.5). If methyl chloride rotates to orient itself on the opposite verse along the z direction, the system would become evolve **Rx** in the $F_z = 5.0 \times 10^{-3}a.u.$ PES. Figure 2.5 shows a qualitative picture of **Rx** and **Rx2** structures in relation with the applied

OEEF, underlining how methyl chloride rotation would lead from **Rx2** to **Rx**.

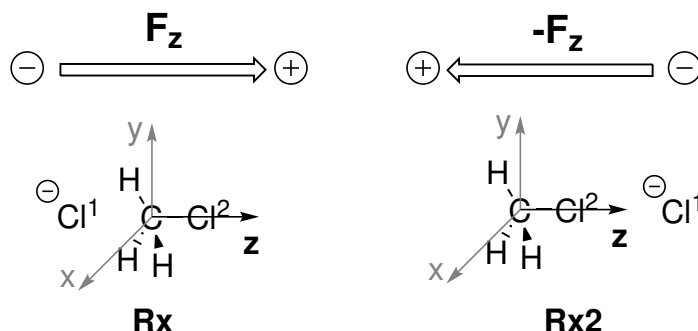


Figure 2.5: **Rx** and **Rx2** with their relative orientation in the chosen Cartesian system.

Rx2 is the only stable reactant complex found at negative field values. OEEFs can orient molecules in order to impose an unfavourable trajectory. **Rx2** is not a prereactive complex for the *back-side* mechanism because of the orientation of methyl chloride molecule.

In Table 2.2 some important chemical-physical properties are collected:

	Rx2				Rx	
$(F_z, 10^{-3}a.u.)$	-12.5	-10.0	-5.0	0.0	0.0	5.0
E (kcal mol ⁻¹)	24.5	18.7	14.5	13.3	0.0	0.1
R(Cl ¹ -C) (Å)	4.53	4.59	4.78	3.32	3.12	1.80
R(C-Cl ²) (Å)	1.80	1.78	1.78	1.78	1.83	-0.52
q(Cl ¹) (a.u.)	-0.76	-0.87	-0.94	-0.98	-0.97	-0.93
q(C) (a.u.)	-0.68	-0.64	-0.61	-0.58	-0.51	-0.48
q(Cl ²) (a.u.)	0.00	0.02	0.02	0.00	-0.17	-0.25

Table 2.2: Bond lengths: (R) and partial charges (q) of **Rx** and **Rx2** at different intensities of the OEEF along the z-axis. Relative energies of **Rx** and **Rx2** (E) refer to unperturbed **Rx**.

Interestingly, from $F_z = 0.0$ to $-12.5 \times 10^{-3}a.u.$, $q(\text{Cl}^1)$ varies from -0.98 to -0.76 $a.u.$ Nonetheless, $q(\text{Cl}^2)$ does not change with the field intensity. The charge transfer process, where $0.22e^-$ is transferred, takes place towards the methyl group. $q(\text{C})$ varies from -0.58 to -0.68 $a.u.$. Extending these considerations to the limit, *it is possible to extrapolate a field value where a Cl_2 molecule is generated and a CH_3^- anion acts as a leaving group from the nucleophilic attack of Cl^1 on Cl^2* . Figure 2.6 shows the specific hypothetical case with the related generalisation in terms of organic reactivity.

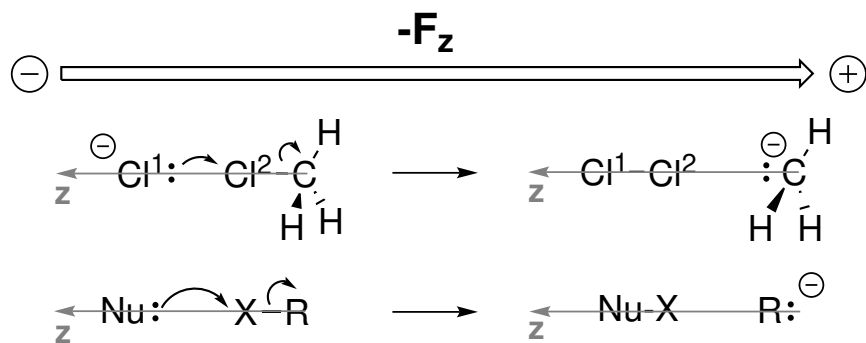


Figure 2.6: Qualitative picture of a hypothetical reaction, where chloride anion leading nucleophilic attack on chloride atom instead of the classical electrophilic carbon atom, thanks to $-F_z$ (on top). A generalisation of this behaviour (bottom).

In the methyl chloride and chloride anion case, other than a tendency, this behaviour can not be observed in the range of considered field intensities. Different chemical systems with higher polarisability (by choosing Nu, X and R properly) may show this behaviour at lower OEEF intensities.

In the present case, the phenomenon was observed from the analysis of the reactant complex in substitution reaction. However, during this PhD project, Shaik and co-workers published analogous results (2019). [51] They demonstrated that the uncommon nucleophilic displacement reaction: $(B \cdots X - Y \longrightarrow B - X + :Y^-)$ can be catalysed by OEEFs. When an OEEF is applied along the $B \cdots X \cdots Y$ reaction axis, the field acts as electric tweezers that orient the XB along the field's axis, catalysing the process, by tens of kcal mol^{-1} . Furthermore, at a critical OEEF, each $B - X$ undergoes spontaneous and barrier-free reaction. [51].

This research, together with the results obtained by Shaik and co-workers, underlines that energetically unfavoured processes such as charge separation processes can be catalysed thanks to the application of OEEFs. Both studies point out that OEEFs can reverse the electron flux displacement leading to an inverted reactivity, concerning the conventional (non-inverted) organic reactivity.

Back-Side and Front-Side Competitive Mechanisms. TS_{Back} and TS_{Front} found during the gas-phase study were reinvestigated under the effect of OEEFs. Fields are applied along the z-axis as defined in Figure 2.4.

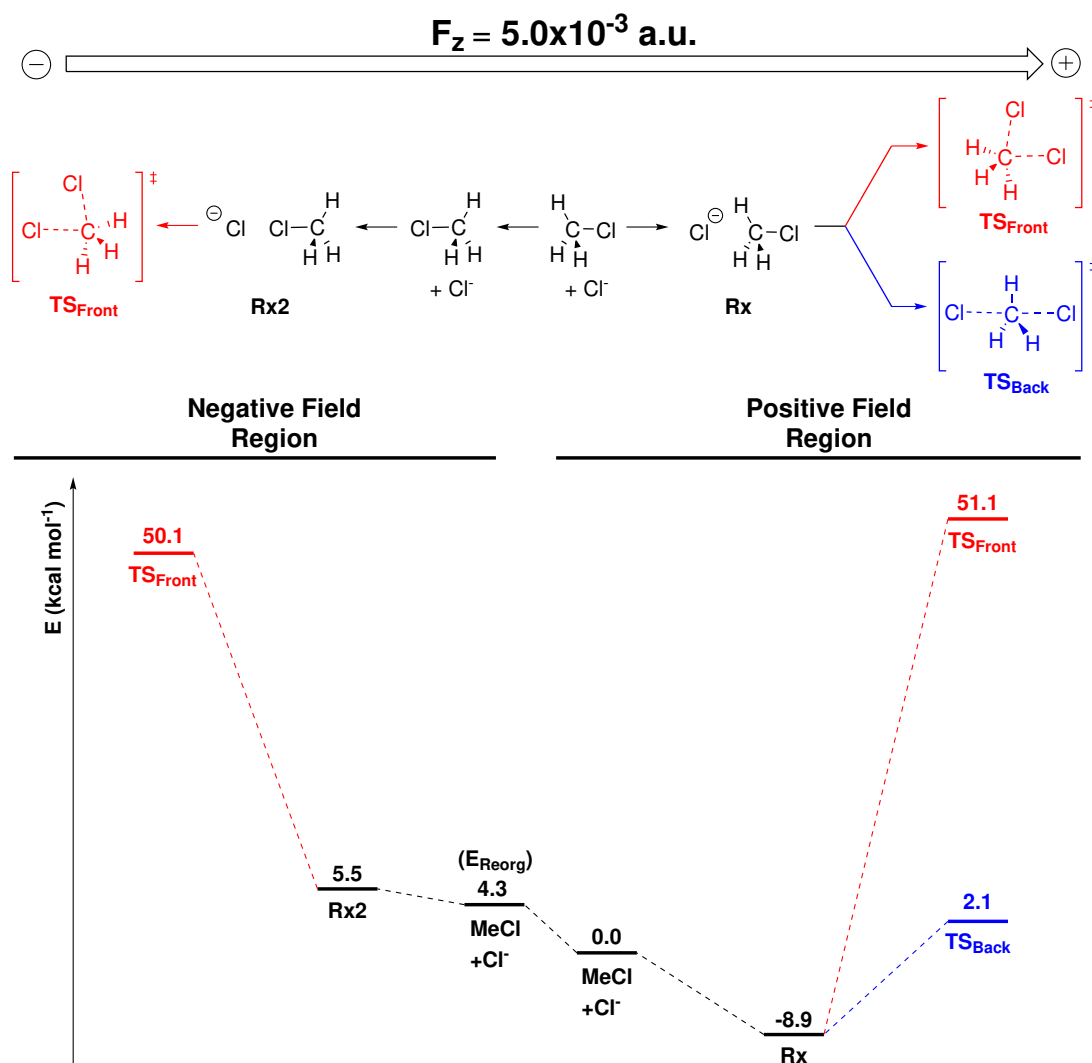


Figure 2.7: Reaction profiles of chlorine exchange reaction between methyl chloride and chloride anion under the influence of $F_z = 5.0 \times 10^{-3} \text{ a.u.}$. At $F_z = -5.0 \times 10^{-3} \text{ a.u.}$ methyl chloride molecule rotates by 180° by paying E_{Reorg} .

to discuss the OEEF effects on these competitive mechanisms, it has been initially considered a small range of intensities $R(F_z)$, $R(F_z, 10^{-3} \text{ a.u.}) = [-5.0; 5.0]$. In Figure 2.7 the reaction profiles for both mechanisms are depicted when $F_z = 5.0 \times 10^{-3} \text{ a.u.}$ Figure 2.7 shows also the relationship between the profiles as a function of the orientation of the system with respect to the OEEF. In particular, negative ($F_z = -5.0 \times 10^{-3} \text{ a.u.}$) and positive ($F_z = 5.0 \times 10^{-3} \text{ a.u.}$) field regions correspond to those region where the system is oriented conversely with respect to the applied field.

Thanks to the anisotropy of the model, when an OEEF is applied, it is possible to depict a unified model where all the critical points are connected.

The positive field region pathway is energetically favoured. TS_{Back} lays $2.1 \text{ kcal mol}^{-1}$ over the asymptotic limit and the internal barrier is $11.0 \text{ kcal mol}^{-1}$. Compared to the unperturbed profile (internal barrier of $13.4 \text{ kcal mol}^{-1}$) there is

a slight catalytic effect. This effect is rationalised in terms of induced dipole moment of $\mathbf{R}\mathbf{x}$ ($\mu_z(\mathbf{R}\mathbf{x})$) and $\mathbf{TS}_{\mathbf{Back}}$ ($\mu_z(\mathbf{TS}_{\mathbf{Back}})$). From the no-field case to $F_z = 5.0 \times 10^{-3} a.u.$ case, ($\mu_z(\mathbf{R}\mathbf{x})$) changes from -0.97 to -1.25 D. This means that $\mathbf{R}\mathbf{x}$ is stabilised when the field is applied. However, ($\mu_z(\mathbf{TS}_{\mathbf{Back}})$) changes from 0.00 to -0.71 D: the induced dipole moment variation of $\mathbf{TS}_{\mathbf{Back}}$ is higher than $\mathbf{R}\mathbf{x}$. These variations produce a net catalytic effect, observable in the internal barrier decrease. Finally, $\mu_z(\text{MeCl})$ varies from -2.11 to -3.14 D, which reflects $\mathbf{R}\mathbf{x}$ energy increase with respect to the asymptotic limit. $\mu_z(\mathbf{TS}_{\mathbf{Front}})$ changes from 0.22 to 0.07 D: $\mathbf{TS}_{\mathbf{Front}}$ is weakly destabilised, because $\mathbf{R}\mathbf{x}$ stabilisation is higher. Again, the unperturbed internal barrier is 59.2 kcal mol⁻¹, while in the presence of F_z becomes 60.0 kcal mol⁻¹.

The trend of the induced dipole moment variation, from $F_z = 0.0$ to $5.0 \times 10^{-3} a.u.$ ($\Delta\mu_z$) is: ($\Delta\mu_z(\text{MeCl})=1.02$ D) > ($\Delta\mu_z(\mathbf{TS}_{\mathbf{Back}})=0.71$ D) > ($\Delta\mu_z(\mathbf{R}\mathbf{x})=0.28$ D) > ($\Delta\mu_z(\mathbf{TS}_{\mathbf{Front}})=0.15$ D). This is reflected in the relative variation of each critical point energy on the field-perturbed reaction profile.

Moreover, PES topology changes can be appreciated by the lack of a $\mathbf{TS}_{\mathbf{Back}}$ structure at high field values outside the range $R(F_z)$. At $F_z > |5.0 \times 10^{-3}| a.u.$ no $\mathbf{TS}_{\mathbf{Back}}$ structures were found and $\mathbf{TS}_{\mathbf{Back}}$ is no longer a saddle point. *Transition state structure isolation is not possible because the chlorine exchange reaction with back-side mechanism becomes a barrier-free process.* Charge separation and migration to the electric field poles govern the transformation of the reaction profile. On the other hand, $\mathbf{TS}_{\mathbf{Front}}$ is still a transition state and its energy is lowered by the OEEF.

Higher field values in an extended range $R(F_z, 10^{-3} a.u.) = [-12.5; 12.5]$ emphasize this behaviour. $\mathbf{R}\mathbf{x}$ and $\mathbf{TS}_{\mathbf{Back}}$ disappear and only $\mathbf{R}\mathbf{x}2$ and $\mathbf{TS}_{\mathbf{Front}}$ remain identifiable critical points along the high-field reaction profile. $\mathbf{TS}_{\mathbf{Front}}$ is still a transition state because of its bent geometry which allows the OEEF ($F_z > |5.0 \times 10^{-3}| a.u.$) to interact with only one C-Cl bond, differently from $\mathbf{TS}_{\mathbf{Back}}$ (Figure 2.8).

The negative field region contains the energetically favoured pathway. With the disappearance of $\mathbf{TS}_{\mathbf{Back}}$ the activation energies trend is reversed and $\mathbf{TS}_{\mathbf{Front}}$ can occur progressively easier at high negative field values.

If $F_z = -10.0 \times 10^{-3} a.u.$, $\mathbf{TS}_{\mathbf{Front}}$ lays 54.8 kcal mol⁻¹ (ΔE_{Glob}^{\neq}) over the asymptotic limit and the internal barrier (ΔE_{Int}^{\neq}) is 41.4 kcal mol⁻¹. Compared to the unperturbed profile ($\Delta E_{Int}^{\neq} = 59.2$ kcal mol⁻¹) there is a strong catalytic effect with an internal barrier decrease of 17.8 kcal mol⁻¹, a value which is consistent with enzymatic catalysis.

This trend is emphasised when $F_z = -12.5 \times 10^{-3} a.u.$ $\mathbf{TS}_{\mathbf{Front}}$ lays 57.8 kcal mol⁻¹ over the asymptotic limit (ΔE_{Glob}^{\neq}) and the internal barrier (ΔE_{Int}^{\neq}) is 36.5

kcal mol⁻¹. Compared to the unperturbed profile ($\Delta E_{Int}^\ddagger = 59.2$ kcal mol⁻¹) there is an internal barrier decrease of 22.8 kcal mol⁻¹.

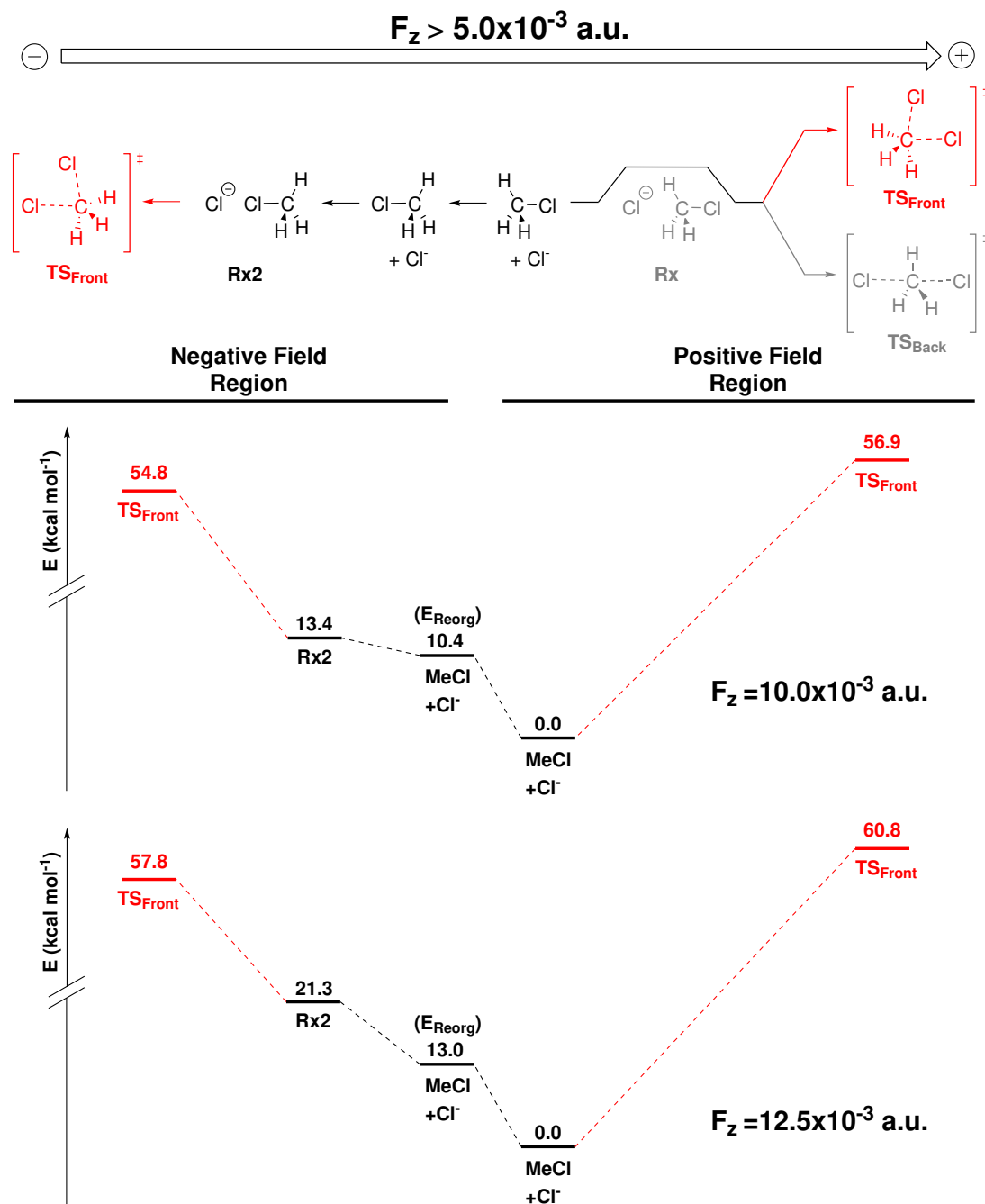


Figure 2.8: Reaction profiles of chlorine exchange reaction between methyl chloride and chloride anion under the influence of $F_z = 10.0 \times 10^{-3}$ a.u. At $F_z = -10.0 \times 10^{-3}$ a.u. methyl chloride molecule rotates by 180° by paying E_{Reorg} . The same reaction profile under the influence of $F_z = 12.5 \times 10^{-3}$ a.u. is reported below. The picture underlines that **Rx** is not a critical point anymore.

In Table 2.3 the chemical-physical properties of TS_{Back} and TS_{Front} are reported. TS_{Back} is more sensitive, and hence, less stable to OEEFs effects: from

$(F_z, 10^{-3}a.u.)$	TS _{Back}		TS _{Front}						
	0.0	5.0	-12.5	-10.0	-5.0	0.0	5.0	10.0	12.5
ΔE_{Glob}^\ddagger	1.6	2.1	57.8	54.8	50.1	47.4	51.1	56.9	60.8
ΔE_{Int}^\ddagger	13.4	11.0	36.5	41.4	44.6	59.2	60.0	56.9	60.8
R(C ¹ -C) (Å)	2.31	2.49	2.37	2.37	2.40	2.45	2.50	2.60	2.67
R(C-C ²) (Å)	2.31	2.15	2.39	2.40	2.42	2.45	2.50	2.57	2.60
q(C ¹) (a.u.)	-0.62	-0.73	-0.58	-0.58	-0.59	-0.62	-0.64	-0.69	-0.72
q(C) (a.u.)	0.37	-0.38	-0.40	-0.39	-0.36	-0.32	-0.28	-0.20	-0.15
q(C ²) (a.u.)	-0.62	-0.51	-0.53	-0.55	-0.58	-0.62	-0.66	-0.70	-0.72

Table 2.3: Bond lengths (R), partial charges (q), global (ΔE_{Glob}^\ddagger) and internal (ΔE_{Int}^\ddagger) barriers of TS_{Back} and TS_{Front} at different intensities of the OEEF along the z-axis

$F_z = 0.0$ to $F_z = 5.0 \times 10^{-3}a.u.$, $\Delta R(C-C^{1})=0.18\text{\AA}$ and $\Delta R(C-C^{2})=0.16\text{\AA}$. On the contrary, for TS_{Front} $\Delta R(C-C^{1})=\Delta R(C-C^{2})=0.05\text{\AA}$: TS_{Front} is more stable at high field values $F_z > 5.0 \times 10^{-3}a.u.$ This computational analysis of the OEEFs effects on S_N2 reaction between methyl chloride and chloride anion can be summarised as follows: *when a negative field is applied along the z-axis, the system will rotate with the aim of orienting the C-Cl bond with the field as in the positive field case. In this way the back-side mechanism can occur barrier-free. However, if the methyl chloride is forced to be oriented negatively along the z-axis, when a negative field is applied Cl⁻ can not approach the back-side of methyl chloride. In this case the back-side mechanism can not occur and only the front-side mechanism occurs.*

2.2.2.2 Case Study: OEEF-Functional Group Relationship

Norbornane is a bicyclic hydrocarbon (C₇H₁₂). The carbon skeleton is derived from the cyclohexane ring with a methylene bridging the 1,4-positions. This compound is a prototype for strained bicyclic compounds.

In Figure 2.9 a norbornane molecule with the carbon atoms numeration is depicted. The methylene bridge C1-C7-C4 is highly strained and makes S_N2 reactions difficult to occur. Experimental studies demonstrated that S_N2 reaction can occur easily in presence of a carbonyl group at C2 position. [52] Further computational studies showed a relation between the local electric field generated by functional groups and the rate of substitution reaction in C7 position. [53]

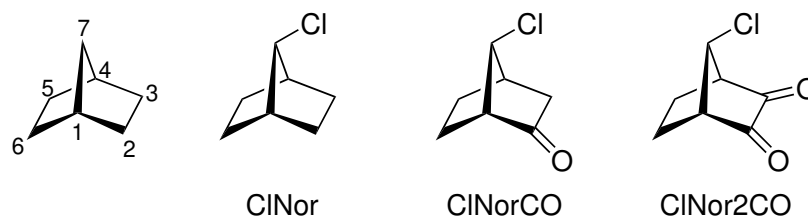


Figure 2.9: From the left to the right side, norbornane structure with the relative carbon atoms numeration, 7-chloronorbornane (ClNor), syn-7-chloro-2-norbornanone (ClNorCO) and syn-7-chloro-2,3-norbornandione (ClNor2CO)

The results of these studies suggest to evaluate whether an OEEF could be used to affect the reactivity analogously to functional groups. The synthetic strategy of inducing reactivity by modifying the chemical structure is a well known approach. An OEEF used to induce a reactivity in unreactive compounds, instead of modifying the chemical structure, can be a synthetic shortcut.

The unperturbed reaction profiles presented in this thesis (Figure 2.10) show an energetic trend depending of the number of carbonyl groups. A slight decrease in internal barrier values (ClNor, 32.3 kcal mol⁻¹) → (ClNorCO, 31.2 kcal mol⁻¹) → (ClNor2CO, 25.4 kcal mol⁻¹) can be appreciated. Both reactants (**Rx**) and transition state (**TS**) decrease in energy: functional groups translate the reaction profile at lower energies with respect to the asymptotic limit. Nonetheless, the higher **TS** stabilisation compared to the **Rx** stabilisation produces a net decrease of the internal barrier.

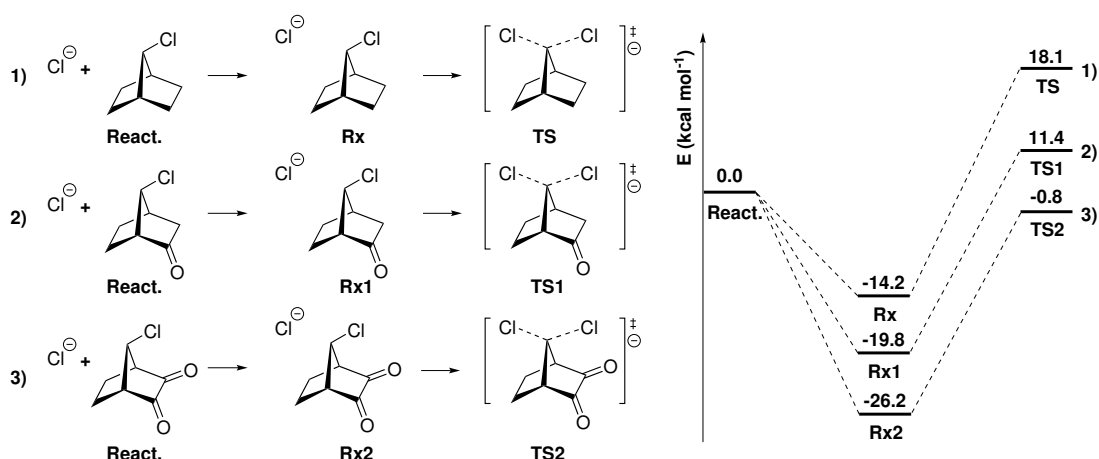


Figure 2.10: Reaction mechanisms (on the left) and profiles (on the right) for chlorine exchange reaction between chloride anion and 1) ClNor, 2) ClNorCO and 3) ClNor2CO.

Subsequently, fields-effect on the chlorine exchange reaction between 7-chloronorbornane and chloride anion was investigated. In particular different OEEF

orientations were tested and compared with the unperturbed cases reported in Figure 2.10. Figure 2.11 shows the 7-chloronorbornane molecule where the S_N2 reaction was investigated under the influence of an OEEF along z -axes z , z' and z'' .

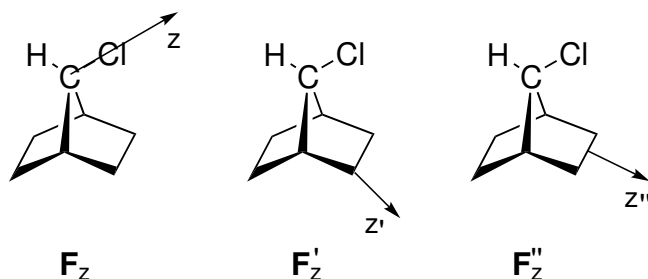


Figure 2.11: OEEF orientations for the ClNor molecule. Three cases from left to right: F_z, F'_z and F''_z .

Z -axes were chosen to emulate the carbonyl groups. In the ketone case (ClNorCO), the system is subject to a field along a z -axis which is parallel to the carbonyl group (F'_z), while in the diketone case (ClNor2CO) the field is applied along the bisector of the carbonyl groups angle (F''_z). Finally, F_z is an additional orientation, chosen due to the previous results on the catalytic effect of an OEEF along the C-Cl bond: catalytic effects on the chlorine exchange reaction encourage to test this orientation, also in the case of 7-chloronorbornane where S_N2 reaction on C7 is difficult to achieve.

During this investigation, the interest was focused on analysing the effect of an OEEF mimicking the effect of a functional group dipole.

The effect of an electric field oriented as in the model cases depicted in Figure 2.11 was evaluated in the scanned range of intensities $R(F_z, 10^{-3} a.u.) = [-5.0; 5.0]$. The various critical points along the reaction profile of ClNor (Figure 2.11, profile 1) were fully re-optimised in the presence of F_z, F'_z and F''_z , to obtain the different field-perturbed profiles.

Reactant Complex. As demonstrated from the previous study on the relationship between an applied field and type I- S_N2 mechanism, the effect of OEEFs on \mathbf{R}_x geometry can be very important. In particular, the anion-dipole interaction between the chloride anion and 7-chloronorbornane molecule can be easily overwhelmed by an OEEF. Norbornane case emphasises this aspect (Figure 2.12): \mathbf{R}_x geometry under the influence of F_z and F'_z changes significantly, already at low field magnitude ($\pm 2.5 \times 10^{-3} a.u.$). No \mathbf{R}_x structures were found when F_z and $F'_z > |2.5 \times 10^{-3}| a.u.$

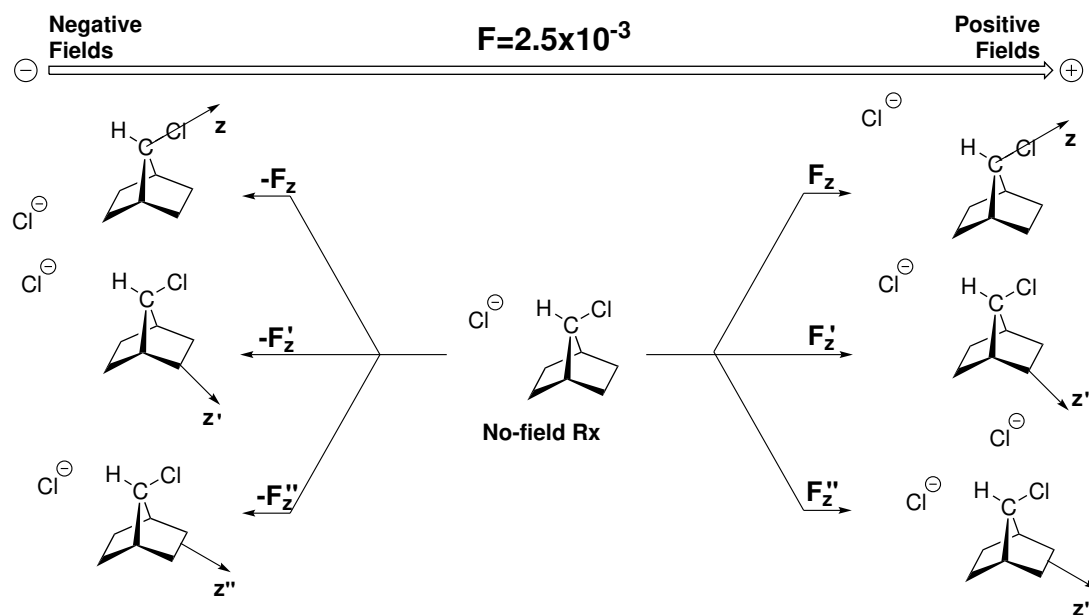


Figure 2.12: **Rx** geometry changing when $F_z = \pm 2.5 \times 10^{-3} a.u.$ for the z -axis orientation considered (F_z , F'_z and, F''_z).

The only stable reactant complex, which does not rearrange significantly its geometry, is **Rx** under the influence of F''_z . Norbornane molecule acts as a structural barrier against the chloride anion motion along the F''_z -induced trajectory. This investigation on reactant complexes shows already that an OEEF acts differently on the system, compared to the local electric field generated by a functional group. Chloride anion position and chemical-physical properties (Table 2.4) are strongly influenced by the OEEF. Moreover, norbornane, instead of methyl group, is not able to produce an analogous of **Rx2** and hence, no **Rx2**-like structures were isolated.

Transition States and reaction profiles. At low field value $F = \pm 2.5 \times 10^{-3} a.u.$ all field orientations produce a net catalytic effect similar to the one produced by carbonyl groups. However, the reaction profiles when an OEEF is applied are intrinsically different (Figure 2.13).

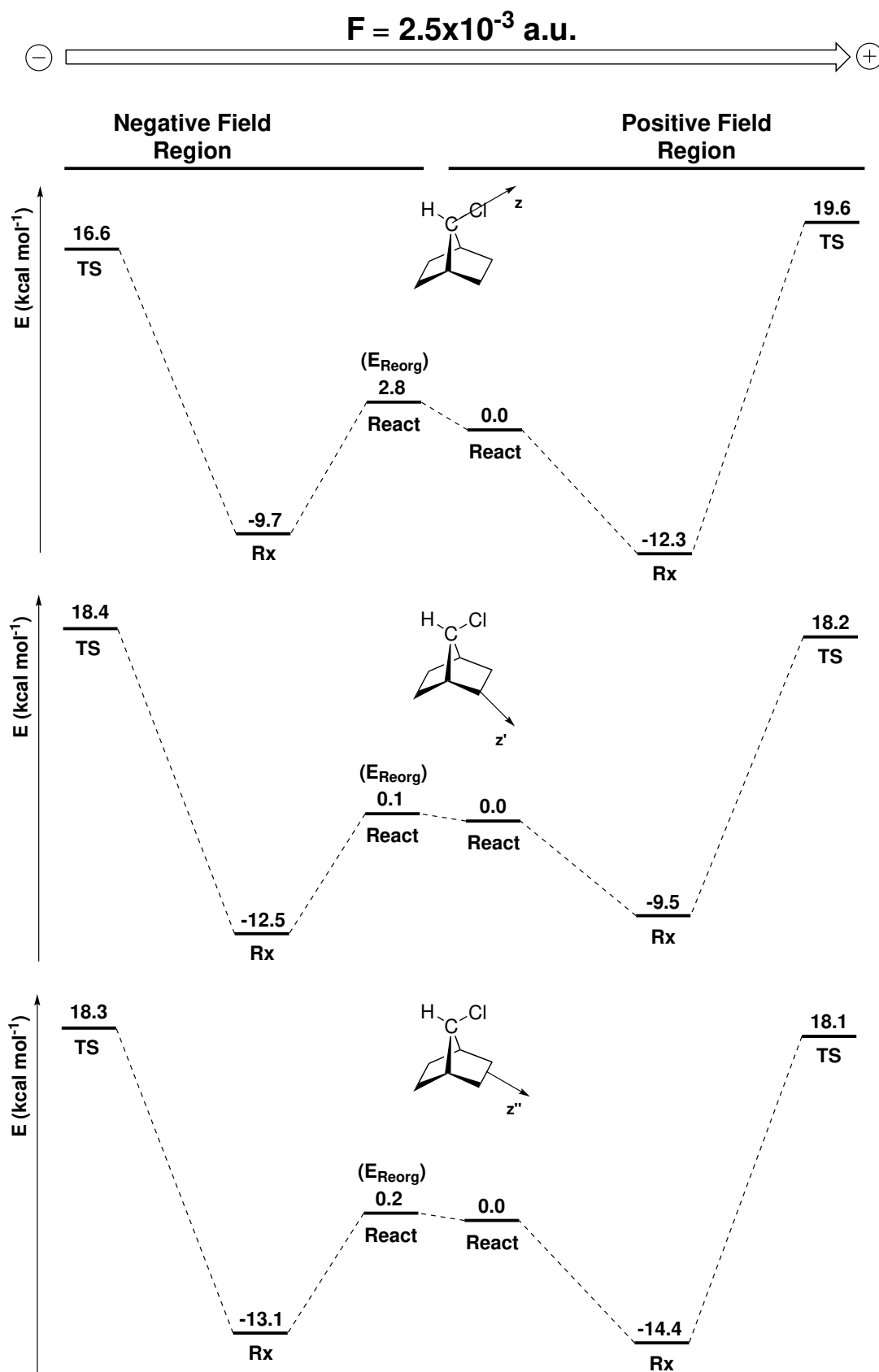


Figure 2.13: Reaction profiles of chlorine exchange reaction between 7-chloronorbornane and chloride anion under the influence of $F = 2.5 \times 10^{-3} \text{ a.u.}$. At $F = -2.5 \times 10^{-3} \text{ a.u.}$ 7-chloronorbornane molecule rotates by 180° by paying E_{Reorg} . F_z is applied on the system (top), F'_z is applied on the system (middle), F''_z is applied on the system (bottom).

Carbonyl groups have a larger stabilising effect on TS structures than **Rx** structures. Indeed, OEEFs destabilise **Rx** complexes by modifying their geometries. This trend is emphasised when $F_z = \pm 5.0 \times 10^{-3} a.u.$, where **Rx** is no longer a critical point (when F_z and F_z' are applied, Figure 2.14)

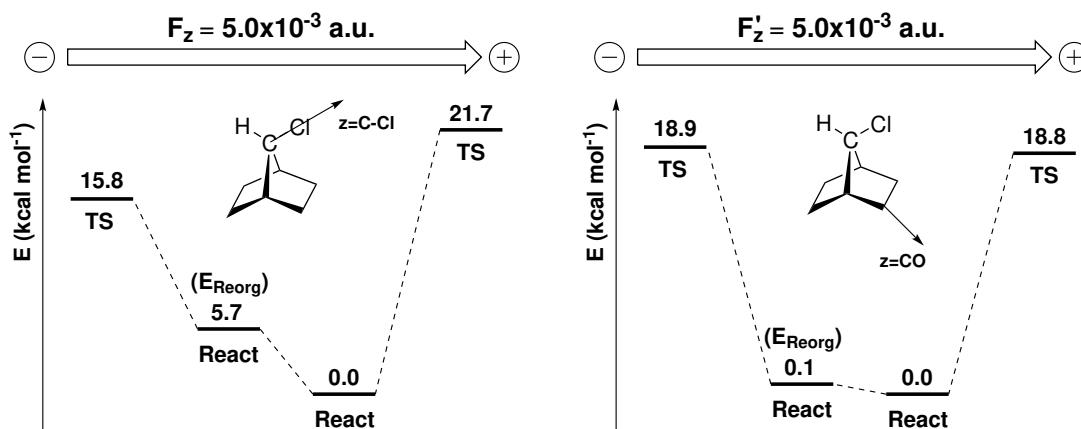


Figure 2.14: Reaction profiles of chlorine exchange reaction between 7-chloronorbornane and chloride anion under the influence of $F = 5.0 \times 10^{-3} a.u.$. At $F = -5.0 \times 10^{-3} a.u.$ 7-chloronorbornane molecule rotates by 180° by paying E_{Reorg} . F_z is applied on the system (left), F_z' is applied on the system (right).

Only F_z'' maintains the critical point nature of **Rx** thanks to its orientation which forbids the chloride anion to "escape" due to the norbornane structural barrier. Nonetheless, the destabilisation of **Rx**, in this case, is still observed (Figure 2.15).

This case study points out that *OEEFs oriented along a functional group dipole moment can lower activation barriers of a similar extent but with different action mechanisms, compared to structural modifications. In particular, OEEFs act by modifying the nucleophile and electrophile relative orientation in Rx structures, in addition to the stabilisation of the TS structures.* (Table 2.4)

$(F_z, 10^{-3} a.u.)$	-5.0		-2.5		0.0		2.5		5.0	
Crit. Point	Rx	TS								
R(C1 ¹ -C) (Å)		2.48	5.79	2.53	3.57	2.59	3.42	2.64		2.69
R(C-C1 ²) (Å)		2.64	1.81	2.62	1.82	2.59	1.83	2.56		2.54
q(C1 ¹) (a.u.)		-0.68	-0.99	-0.70	-0.97	-0.72	-0.96	-0.72		-0.77
q(C) (a.u.)		0.17	-0.19	0.19	-0.21	0.20	-0.21	0.21		0.23
q(H) (a.u.)		0.27	0.21	0.26	0.29	0.26	0.31	0.26		0.27
q(C1 ²) (a.u.)		-0.73	-0.09	-0.73	-0.12	-0.72	-0.14	-0.75		-0.72
$(F'_z, 10^{-3} a.u.)$	-5.0		-2.5		0.0		2.5		5.0	
Crit. Point	Rx	TS								
R(C1 ¹ -C) (Å)		2.57	3.70	2.58	3.57	2.59	5.67	2.60		2.61
R(C-C1 ²) (Å)		2.68	1.82	2.63	1.82	2.59	1.81	2.55		2.51
q(C1 ¹) (a.u.)		-0.73	-0.98	-0.73	-0.97	-0.72	-0.98	-0.72		-0.72
q(C) (a.u.)		0.24	-0.20	0.22	-0.21	0.20	-0.18	0.19		0.17
q(H) (a.u.)		0.26	0.28	0.26	0.29	0.26	0.21	0.27		0.27
q(C1 ²) (a.u.)		-0.78	-0.12	-0.75	-0.12	-0.72	-0.10	-0.70		-0.68
$(F''_z, 10^{-3} a.u.)$	-5.0		-2.5		0.0		2.5		5.0	
Crit. Point	Rx	TS								
R(C1 ¹ -C) (Å)	4.04	2.56	3.71	2.57	3.57	2.59	3.47	2.60	3.40	2.61
R(C-C1 ²) (Å)	1.81	2.69	1.82	2.64	1.82	2.59	1.82	2.53	1.83	2.48
q(C1 ¹) (a.u.)	-0.98	-0.73	-0.98	-0.72	-0.97	-0.72	-0.96	-0.72	-0.95	-0.72
q(C) (a.u.)	-0.20	0.23	-0.20	0.22	-0.21	0.20	-0.21	0.18	-0.21	0.16
q(H) (a.u.)	0.28	0.26	0.28	0.26	0.29	0.26	0.31	0.27	0.31	0.27
q(C1 ²) (a.u.)	-0.12	-0.78	-0.12	-0.75	-0.12	-0.72	-0.13	-0.69	-0.13	-0.67

Table 2.4: Bond length (R) and partial charges (q) of the transition state for the *back-side* mechanism, at different intensities of the OEEF along the z , z' and z'' -axis.

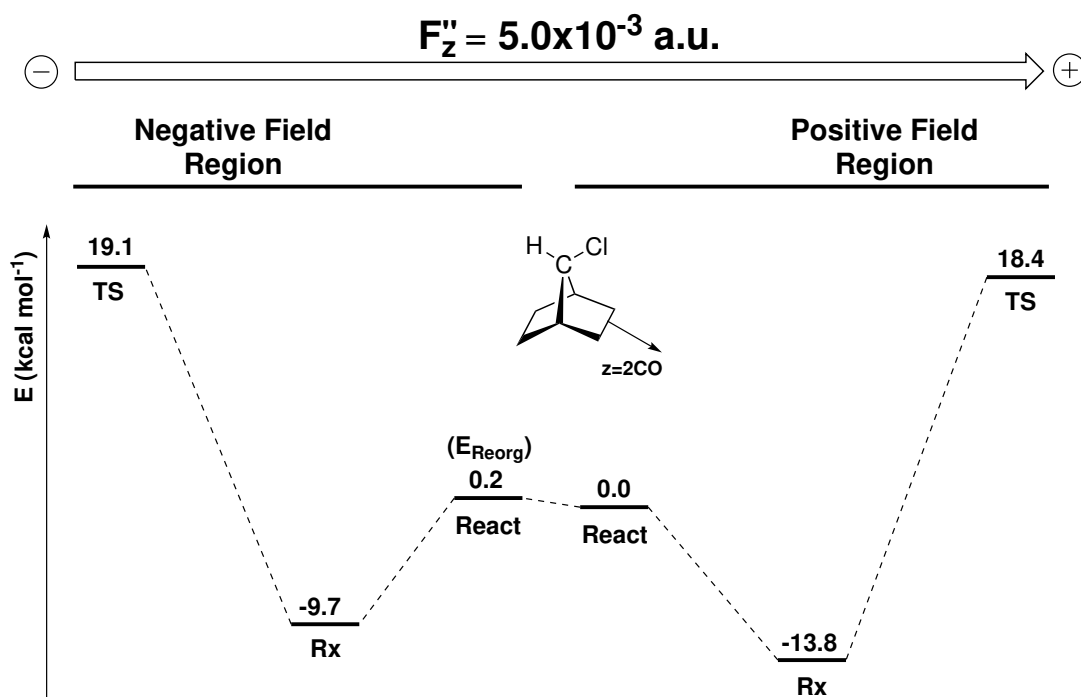
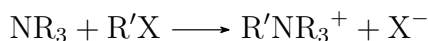


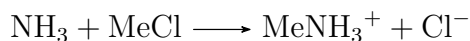
Figure 2.15: Reaction profile of the chlorine exchange reaction between 7-chloronorbornane and chloride anion under the influence of $F_z'' = 5.0 \times 10^{-3} a.u.$ At $F_z'' = -5.0 \times 10^{-3} a.u.$ 7-chloronorbornane molecule rotate by 180° by paying E_{Reorg} .

2.2.2.3 Type II Substitution Reactions

The OEEFs effects on substitution reactions of a type II S_N2 was investigated. The Menshutkin reaction [54] is the prototype of type II S_N2 reaction. In this reaction, an amine reacts with an alkyl halide in order to generate an ammonium salt.



In particular, to be consistent with the previous investigation, the Menshutkin reaction between methyl chloride and ammonia was taken into account.



This kind of S_N2 reaction has been extensively studied both experimentally [55,56] and theoretically [57,58] for the dependence of the reaction rate and equilibrium constant from the polarity of the solvent. Moreover, this reaction is conceivable as the simplest model of amine alkylation, *via* substitution reaction.

The reaction profile strongly depends on the polarity of the solvation media, with a dramatic decrease of the activation energy and the switch from endothermic to exothermic reaction profile. These characteristics, make Menshutkin reaction a benchmark test for new solvation models validation. [59,60]

Due to the large amount of theoretical and experimental data available in the literature and the high sensitivity of the reaction profile with respect to polarising environments such as solvents, this kind of reaction profile is a good choice to test the effects of OEEFs.

Unperturbed Profile. The reaction profile for the hypothetical gas-phase prototype reaction $\text{NH}_3 + \text{MeCl} \longrightarrow \text{MeNH}_3^+ + \text{Cl}^-$ computed with the M06-2X functional is an asymmetric double-well potential, very similar to that obtained by Uko Maran et al [58] (Figure 2.16).

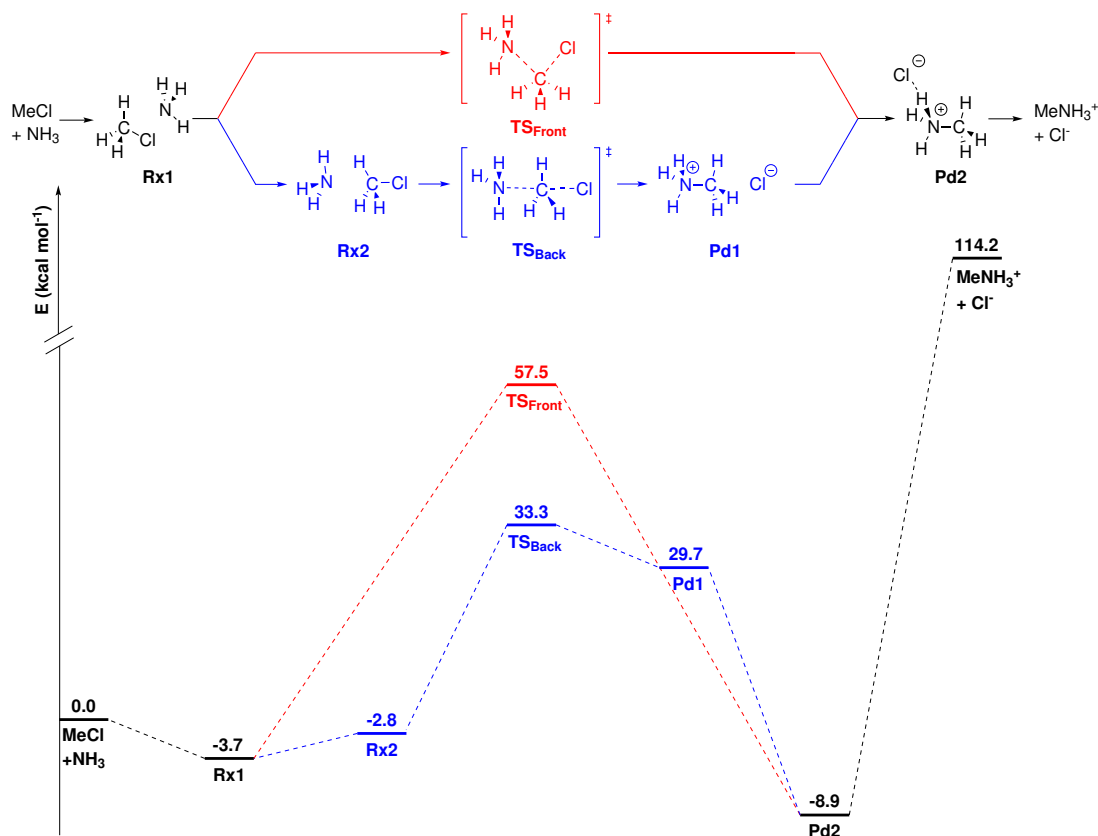


Figure 2.16: *Back* and *front-side* S_N2 mechanisms with their reaction profiles (kcal mol^{-1}).

The first minimum (**Rx1**) is an adduct interacting through the nitrogen of ammonia and the weakly polarized hydrogen of methyl chloride in a sort of bent complex. The next minimum corresponds to the alignment of reactants dipoles in a linear complex (**Rx2**). These two minima lay at $3.7 \text{ kcal mol}^{-1}$ (bent complex, **Rx1**) and $2.9 \text{ kcal mol}^{-1}$ (linear complex, **Rx2**) lower than the asymptotic limit of the isolated reactants respectively. Even in the product region, two minima were identified which can be geometrically distinguished as linear (**Pd1**, $29.7 \text{ kcal mol}^{-1}$) and bent (**Pd2**, $-8.9 \text{ kcal mol}^{-1}$) complexes. The global barrier (ΔE_{Glob}^\ddagger) for the *back-side* mechanism is $33.3 \text{ kcal mol}^{-1}$, the internal barrier (ΔE_{Int}^\ddagger) is $36.1 \text{ kcal mol}^{-1}$, in agreement with previous theoretical studies on this reaction in gas-phase. [58] After the evaluation of the reaction profile for this S_N2 with nucleophilic *back-side* attack, the *front-side* attack was evaluated. In this case, linear complexes for both reactants and products are absent and the global barrier (ΔE_{Glob}^\ddagger) for the *back-side* mechanism is $57.5 \text{ kcal mol}^{-1}$, while the internal barrier (ΔE_{Int}^\ddagger) is $61.2 \text{ kcal mol}^{-1}$. **Front-side mechanism is forbidden with respect to the back-side mechanism by $25.1 \text{ kcal mol}^{-1}$.**

Finally, isolated products lay $114.2 \text{ kcal mol}^{-1}$ over the asymptotic limit. The reaction energy is extremely high because it keeps into account the charge sep-

aration process in gas-phase, which is extremely unfavourable and the system converges to **Pd2**.

Cartesian System Building. The various critical points along the reaction pathways were reinvestigated. The structures were fully re-optimized in the presence of different OEEFs in terms of intensity and orientation. To carry out this investigation it was necessary to build a coordinate system which defines the orientation of molecules and electric fields (Figure 2.17).

In the case of **TS_{Front}** two different orientations were considered, namely **TS_{Front}^a** and **TS_{Front}^b** where the z-axis is defined along the breaking C-Cl bond and forming C-N bond respectively. **TS_{Back}** does not require this distinction thanks to its linear geometry.

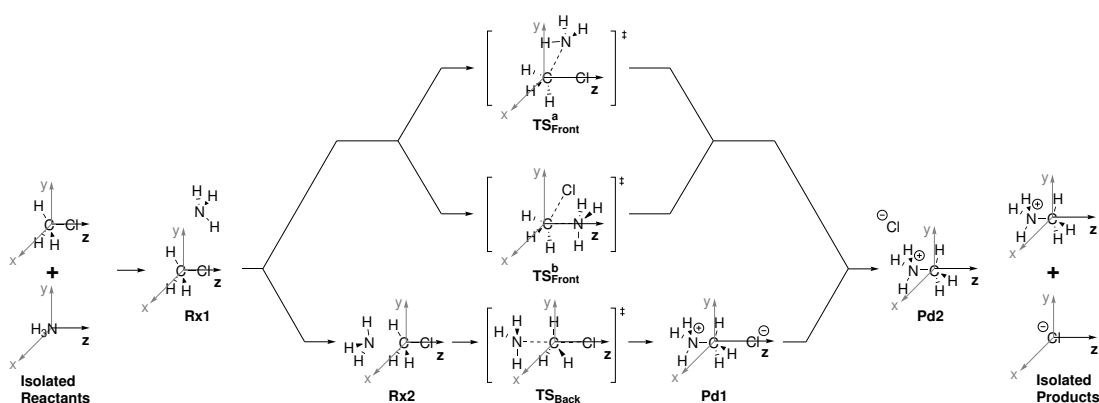


Figure 2.17: The x-,y-,z-directions for the Mentschutkin reaction between ammonia and methyl chloride.

Reactants and Products Reactants and products were fully re-optimized in the presence of OEEFs along the z-axis in the range $R(F_z), R(F_z, 10^{-3}a.u.) = [-12.5; 12.5]$ (Figure 2.18). For ammonia, it was not identified a minimum at

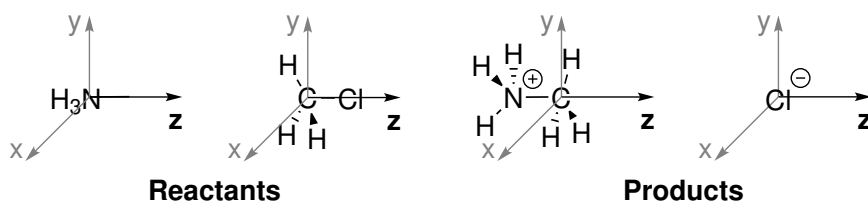


Figure 2.18: The x-,y-,z-directions for isolated reactants and products.

$-F_z$. The PES of ammonia perturbed by $-F_z$ is a monotonically increasing function until the inversion of configuration, which makes ammonia experiences the opposite and stabilizing OEEF (F_z).

	$(F_z, 10^{-3} a.u.)$	-12.5	-10.0	-5.0	0.0	5.0	10.0	12.5
MeCl	E (kcal mol ⁻¹)	4.9	4.2	2.4	0.0	-2.9	-6.2	-8.1
	R(C-Cl) (Å)	1.77	1.78	1.78	1.79	1.79	1.80	1.81
	q(C) (a.u.)	-0.57	-0.57	-0.56	-0.55	-0.54	-0.52	-0.52
	q(Cl) (a.u.)	-0.01	-0.02	-0.05	-0.07	-0.10	-0.13	-0.14
NH ₃	E (kcal mol ⁻¹)				0.0	-2.3	-4.8	-6.2
	A(H-N-H) (Deg)				107.73	106.64	105.67	105.24
	q(N) (a.u.)				-1.05	-1.07	-1.08	-1.08
MeNH ₃ ⁺	E (kcal mol ⁻¹)	34.6	28.3	14.5	0.0	-15.2	-31.1	-39.8
	R(C-N) (Å)	1.50	1.50	1.51	1.51	1.51	1.51	1.51
	q(C) (a.u.)	-0.37	-0.37	-0.37	-0.37	-0.36	-0.36	-0.36
	q(N) (a.u.)	-0.68	-0.68	-0.69	-0.69	-0.69	-0.69	-0.70
Cl ⁻	E (kcal mol ⁻¹)	-0.7	-0.5	-0.1	0.0	-0.1	-0.5	-0.7

Table 2.5: Geometrical parameters Bond lengths: (R), angles: (A) and partial charges (q) of reagents and products at different intensities of the OEEF along the z -axis. Relative energies reported refer to the unperturbed state.

Methyl chloride properties (Table 2.5) variations correspond to those that were already discussed (see section 2.2.2.1). Methyl ammonium shows similar, but emphasised, results being a charged molecule: OEEFs act more intensely and $E_{Reorg} = 74.4$ kcal mol⁻¹, when $F_z = 12.5 \times 10^{-3} a.u.$ Products are more affected from OEEFs, compared to reactants. Reaction energy (ΔE_{React}) varies from the no field case ($F_z = 0.0 a.u.$, $\Delta E_{React} = 114.2$ kcal mol⁻¹) to the field-perturbed case ($F_z = 12.5 \times 10^{-3} a.u.$, $\Delta E_{React} = 88.0$ kcal mol⁻¹) of 26.2 kcal mol⁻¹.

If charge separation process occurs during a reaction, OEEFs lower the reaction energy enhancing the thermodynamics of the reaction.

Reactant Complex. Reactant complexes were fully re-optimised in the presence of OEEFs, as done for reactants. Three different reactant complexes were evaluated under the influence of OEEFs, namely **Rx1**, **Rx2** (from the gas-phase study) and **Rx3** (hypothesised from the type I investigation, see subsection 2.2.2.1, Figure 2.19).

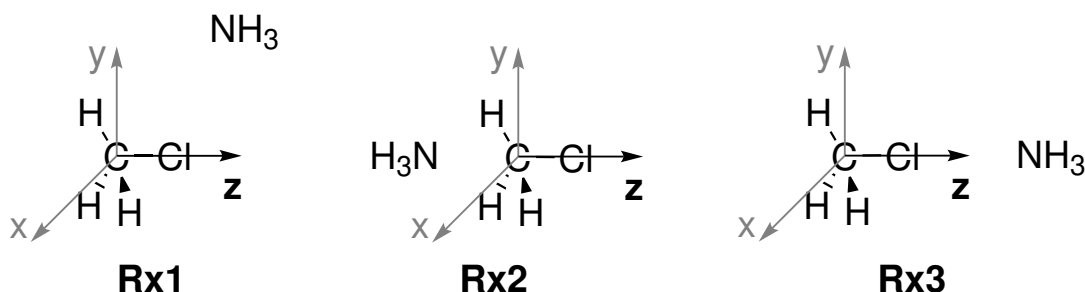


Figure 2.19: The x -, y -, z -directions for **Rx1**, **Rx2**, **Rx3**.

At positive field values, **Rx2** is stabilised thanks to the alignment along the z -axis of the system dipole. **Rx2** structure is more stable compared to its type I

S_N2 analogous and is still a critical point even at high negative values. However, in the case of Menschutkin reaction, **Rx1** showed lower energy compared to **Rx2** in the negative field region.

Rx properties (Table 2.6) do not change significantly as function of the applied

Complex Type	Rx1				Rx2		
$(F_z, 10^{-3}a.u.)$	-12.5	-10.0	-5.0	0.0	5.0	10.0	12.5
E (kcal mol ⁻¹)	9.5	7.0	1.5	-3.7	-3.4	-4.2	-4.7
R(N-C) (Å)	3.57	3.36	3.33	3.32	3.04	3.01	2.98
R(C-Cl) (Å)	1.78	1.78	1.79	1.79	1.81	1.82	1.83
q(N) (a.u.)	-1.09	-1.09	-1.08	-1.09	-1.07	-1.08	-1.09
q(C) (a.u.)	-0.58	-0.57	-0.56	-0.56	-0.52	-0.51	-0.50
q(Cl) (a.u.)	-0.03	-0.04	-0.05	-0.07	-0.13	-0.16	-0.18

Table 2.6: Bond lengths (R) and partial charges (q) of **Rx1**, **Rx2**, **Rx3** at different intensities of the OEEF along the z-axis. Relative energies refer to the most stable **Rx**.

field. A negative field is a destabilising perturbation and the system needs to rearrange to a geometry less sensitive to the applied field. On the contrary, positive field region is stabilising because the system can align its dipole with it. **Rx2** represents the geometry which can better interact with the field to maximise the stabilisation.

Albeit linear reactant complex in type II S_N2 reaction showed enhanced stability, **Rx2** was not isolated as a minimum when $F_z < -5.0 \times 10^{-3}a.u.$. Under the influence of high negative fields, the lone-pair on ammonia nitrogen atom is oriented to the positive pole. **Rx1** and **Rx3** are stable structures at negative field values while **Rx2** is not. **Rx3**-like geometry was found as the most stable for type I S_N2 . In type II S_N2 **Rx3** is still stable but slightly higher in energy when compared to **Rx2** (Table 2.7)

Rx1 and **Rx3** lay at similar energies with an energy difference which is de-

	$(F_z, 10^{-3}a.u.)$	-12.5	-10.0	-5.0	0.0
	E_{Reorg} (kcal mol ⁻¹)	13.0	10.4	5.3	0.0
Rx	E (kcal mol ⁻¹)	9.5	7.0	1.5	-3.7
	ΔE (kcal mol ⁻¹)	-3.5	-3.4	-3.8	-3.7
Rx3	E (kcal mol ⁻¹)	10.5	8.5	4.0	-1.1
	ΔE (kcal mol ⁻¹)	-2.5	-1.9	-1.3	-1.1
	$\Delta\Delta E$ (kcal mol ⁻¹)	1.0	1.5	2.5	2.6

Table 2.7: Energies of **Rx1** and **Rx3** E (kcal mol⁻¹) referred to reactants in their positive field value and relative energies referred to reactants in their negative field value by considering E_{Reorg} . Finally, energy difference between **Rx1** and **Rx3**: $\Delta\Delta E$ (kcal mol⁻¹).

ing with the magnitude of the field, and $\Delta\Delta E$ varies from 2.6 ($F_z = 0.0 a.u.$) to

1.0 kcal mol⁻¹ ($F_z = 12.5 \times 10^{-3} a.u.$). Moreover, recalling that all energies are always reported with respect to the isolated reactants referring to that positive field value (which is the lower one), the reported energies keep into account E_{Reorg} . This contribution points out that reactant complexes are still more stable than the isolated reactants under the influence of that field but with opposite sign.

As in the type I substitution case, **Rx3** is stabilised by an OEEF and again, OEEFs acted as electric tweezers. [51] To have **Rx3** as the most stable complex an higher field outside from scanned $R(F_z)$, is required. Nevertheless, the comparison between **Rx3** for type II substitution and **Rx2** for type I substitution reaction, which share the same type of geometry, reveals that **Rx3** is more stabilised (type I-**Rx2** $\Delta E = 8.3$ kcal mol⁻¹, type II-**Rx3** $\Delta E = -2.5$ kcal mol⁻¹). In this case the field contribution is sufficient to overcome the repulsion between chlorine and nitrogen atoms. The system shows higher chemical compatibility to be tweezed by OEEF.

Back-Side Mechanism. TSs found during the gas-phase study were reinvestigated under the effect of OEEFs. Structures were fully re-optimized with different fields in terms of intensity and orientation. The first reinvestigated TS is the one derived from the *back-side* attack (**TS_{Back}**). The field applied is again along the z-axis in a Cartesian system defined as in Figure 2.20.

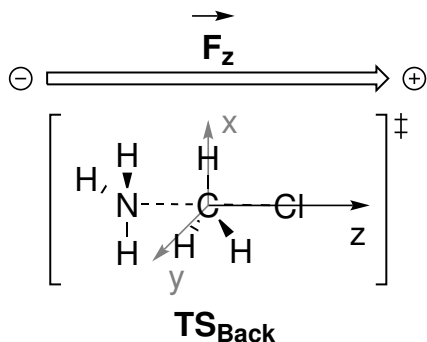


Figure 2.20: The x-,y-,z-directions for **TS_{Back}**.

In Table 2.8 are reported the chemical-physical properties of **TS_{Back}**. Both internal (ΔE_{Int}^\ddagger) and global (ΔE_{Glob}^\ddagger) barriers are reported.

The decrease of the energy barriers (Table 2.8) points out that the transition state stabilisation is more significant than the stabilization of both reactants and reactant complex. Being the transition state dipole, the connection between the reactants and products dipoles, a type II S_N2 transition state is very sensitive to OEEFs. Geometrical data show how the transition state structure changes with the magnitude of the field, in agreement with the Hammond postulate, and

	$(F_z, 10^{-3} a.u.)$	-5.0	0.0	5.0	10.0	12.5
TS_{Back}	ΔE_{Glob}^\ddagger (kcal mol ⁻¹)	54.6	33.3	22.8	13.3	9.1
	ΔE_{Int}^\ddagger (kcal mol ⁻¹)	53.1	36.1	26.2	16.7	13.8
	R(N-C) (Å)	1.69	1.81	1.92	2.03	2.09
	R(C-Cl) (Å)	2.55	2.45	2.38	2.31	2.27
	q(N) (a.u.)	-0.78	-0.83	-0.86	-0.90	-0.92
	q(C) (a.u.)	-0.38	0.35	-0.33	-0.32	-0.32
	q(Cl) (a.u.)	-0.77	-0.71	-0.66	-0.61	-0.59

Table 2.8: Internal (ΔE_{Int}^\ddagger) and global (ΔE_{Glob}^\ddagger) barriers of the *back-side* mechanism. Bond lengths (R) and partial charges (q) of **TS_{Back}**, at different intensities of the OEEF along the z-axis.

becomes more similar to the reactants structure (Figure 2.21).

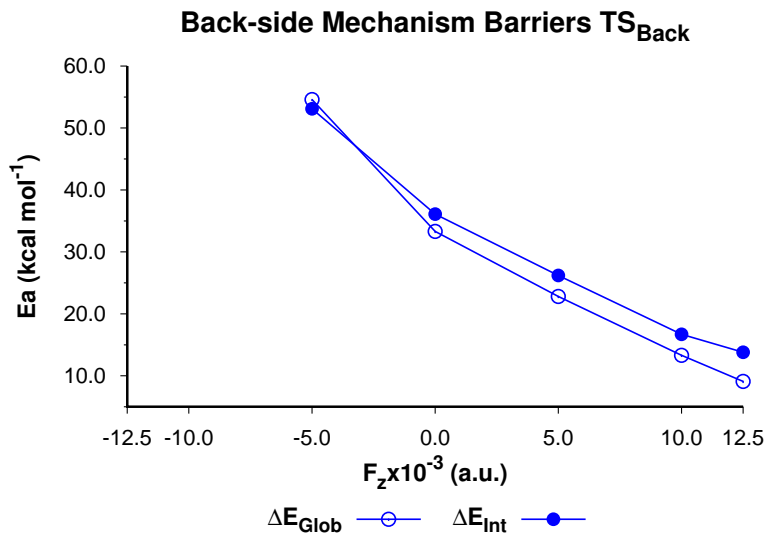


Figure 2.21: Internal (ΔE_{Int}^\ddagger) and global barriers (ΔE_{Glob}^\ddagger) of the *back-side* mechanism as a function of the field intensity in the scanned range $R(F_z, 10^{-3} a.u.)$.

Positive Field Region. The calculated profiles show that *positive fields along the reaction axis strongly catalyse Menshutkin reaction. In particular, when $F_z = 12.5 \times 10^{-3} a.u.$ the internal barrier is lowered by 22.3 kcal mol⁻¹*. This stabilization is in the order of magnitude of activation barriers found in enzymatic catalysis. Furthermore, the reaction profile differs from the gas-phase profile for the lack of **Rx1**. The trajectory of ammonia toward methyl chloride becomes linear along the field direction with a more linear motion defined by the particles migration to the opposite pole. This effect implies a stabilization of those adducts which have a dipole oriented along the field.

The induced dipole moment analysis rationalises these results: $\mu_z(\mathbf{Rx2})$ varies from -4.32 D ($F_z = 0.0 a.u.$) to -6.18 D ($F_z = 12.5 \times 10^{-3} a.u.$); $\mu_z(\mathbf{TS}_{Back})$

	MeCl	NH ₃	MeCl + NH ₃	Rx	TS_{Back}
$F_z = 0.0 \text{ a.u.}$	-2.11	-1.73	-3.84	-4.32	0.00
$F_z = 12.5 \times 10^{-3} \text{ a.u.}$	-3.14	-2.22	-5.36	-6.18	-12.08
$\Delta\mu_z \text{ (D)}$	1.03	0.49	1.52	1.86	12.08

Table 2.9: Induced dipole moment along z-axis: μ_z (D) of methyl chloride, ammonia, reactants, **Rx** and **TS_{Back}** when $F_z = 0.0$ to $12.5 \times 10^{-3} \text{ a.u.}$. The last row is the induced dipole moment variation $\Delta\mu_z$ (D) per critical point.

varies from 0.00 D ($F_z = 0.0 \text{ a.u.}$) to -12.08 D ($F_z = 12.5 \times 10^{-3} \text{ a.u.}$). This great difference in the induced dipole moment variation *per* critical point is observable in the stabilisation of **TS_{Back}**, and reflects in the dramatic decrease of the internal barrier (22.3 kcal mol⁻¹). Isolated reactants induced dipoles have the same behaviour and the sum of the induced dipole moments varies less than $\mu_z(\mathbf{TS}_{\mathbf{Back}})$: $\mu_z(\text{MeCl} + \text{NH}_3)$ varies from -3.83 D ($F_z = 0.0 \text{ a.u.}$) to -5.36 D ($F_z = 12.5 \times 10^{-3} \text{ a.u.}$) (Table 2.9).

The trend of induced dipole moment variation from $F_z = 0.0$ to $12.5 \times 10^{-3} \text{ a.u.}$ ($\Delta\mu_z$) is: ($\Delta\mu_z(\mathbf{TS}_{\mathbf{Back}})$, 12.08 D) > ($\Delta\mu_z(\mathbf{Rx})$, 1.86 D) > ($\Delta\mu_z(\text{MeCl} + \text{NH}_3)$, 1.53 D). This behaviour is reflected in a global lowering of the reaction profile energy which becomes more intense from isolated reactants to **TS_{Back}**. Figure 2.22 shows the unperturbed profile and the profile computed for $F_z = 12.5 \times 10^{-3} \text{ a.u.}$, both referred to the unperturbed isolated reactants.

The unperturbed reaction coordinate is becoming a downhill to a minimum which is the charge separation state at high field values and the overall process is becoming barrier-less.

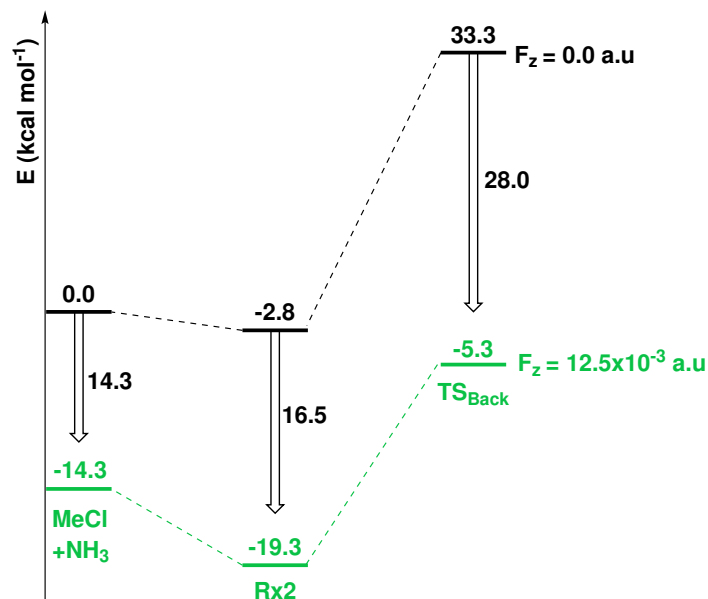


Figure 2.22: OEEF effect on the *back-side* mechanism on the unperturbed case (black lines) when $F_z = 12.5 \times 10^{-3} a.u.$ (green lines). All points refer to the unperturbed isolated reactants.

Negative Field Region. This region is characterised by the lack of a stable structure for TS_{Back} .

When $F_z < -5.0 \times 10^{-3} a.u.$, back-side mechanism can not occur. The pathway from reactants to products going through TS_{Back} is a monotonically increasing energy function without any minimum necessary to define a saddle point, as in type I $\text{S}_{\text{N}}2$.

When $F_z < -5.0 \times 10^{-3} a.u.$, the system will rotate with the aim of be oriented with the C-Cl bond as in the case $F_z > -5.0 \times 10^{-3} a.u.$. However, if methyl chloride is forced to be oriented negatively along the z-axis and $F_z < -5.0 \times 10^{-3} a.u.$ is applied, the back-side mechanism can not occur.

Front-Side Mechanism. As previously shown in Figure 2.16, the no-field gas-phase study shows that the front side attack is energetically forbidden, being $25.1 \text{ kcal mol}^{-1}$ higher than the *back-side* attack. TS_{Front} structure was fully re-optimised under the influence of OEEFs in two different relative orientations with respect to z-axis named $\text{TS}_{\text{Front}}^{\text{a}}$ and $\text{TS}_{\text{Front}}^{\text{b}}$ (Figure 2.23 and Table 2.10).

	F (10^{-3} , a.u.)	-12.5	-10.0	-5.0	0.0	5.0	10.0	12.5
TS_{Front}^a	$\Delta E_{Glob}^{\ddagger}$ (kcal mol ⁻¹)	85.4	79.9	68.8	57.5	55.3	52.8	51.4
	$\Delta E_{Int}^{\ddagger}$ (kcal mol ⁻¹)	75.8	72.9	67.3	60.3	58.8	57.1	56.1
	R(N-C) (Å)	2.09	2.11	2.13	2.16	2.19	2.23	2.26
	R(C-Cl) (Å)	2.42	2.42	2.43	2.44	2.47	2.50	2.54
	q(N) (a.u.)	-0.92	-0.92	-0.92	-0.93	-0.94	-0.95	-0.96
	q(C) (a.u.)	-0.34	-0.32	-0.29	-0.25	-0.21	-0.15	-0.12
	q(Cl) (a.u.)	-0.52	-0.53	-0.56	-0.59	-0.63	-0.67	-0.69
TS_{Front}^b	$\Delta E_{Glob}^{\ddagger}$ (kcal mol ⁻¹)	63.3	62.3	60.1	57.5	60.4	70.0	72.7
	$\Delta E_{Int}^{\ddagger}$ (kcal mol ⁻¹)	53.7	55.3	58.5	60.3	67.4	74.2	77.4
	R(N-C) (Å)	2.31	2.26	2.21	2.16	2.13	2.11	2.09
	R(C-Cl) (Å)	2.59	2.55	2.49	2.45	2.41	2.38	2.37
	q(N) (a.u.)	-0.99	-0.97	-0.95	-0.93	-0.91	-0.90	-0.89
	q(C) (a.u.)	-0.12	-0.16	-0.21	-0.25	-0.28	-0.30	-0.31
	q(Cl) (a.u.)	-0.66	-0.64	-0.61	-0.59	-0.58	-0.56	-0.56

Table 2.10: Internal ($\Delta E_{Int}^{\ddagger}$) and global ($\Delta E_{Glob}^{\ddagger}$) barriers of **TSs_{Front}^{a,b}**. Bond lengths (R) and partial charges (q) of the transition state for the *front-side* nucleophilic attack, at different intensities of the OEEF along the z-axis.

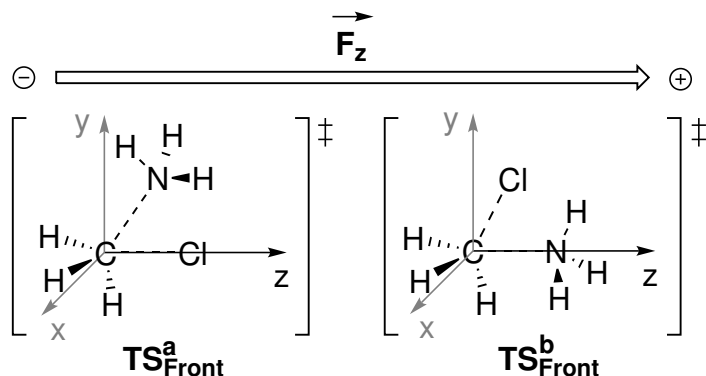


Figure 2.23: The x-,y-,z-directions for **TSs_{Front}** of the Menshutkin reaction. **TS_{Front}** with nucleophilic attack from the *front-side* with the C-Cl bond oriented along the z-axis **TS_{Front}^a**. TS with nucleophilic attack from the *front-side* with the C-N bond oriented along the z-axis **TS_{Front}^b**.

When $F_z < -5.0 \times 10^{-3}$ a.u., Menshutkin reaction takes place with *front mechanism*. This ideal system, under the influence of a fixed OEEF of $F_z = 12.5 \times 10^{-3}$ a.u., will react quantitatively with *back-side mechanism*. *Front-side* mechanism could take place when the system is oriented in the opposite way and, there is enough energy for supporting a process which costs 52.4 kcal mol⁻¹. *Front-side* mechanism trends of the activation barriers are different from the *back-side* attack (Figure 2.24).

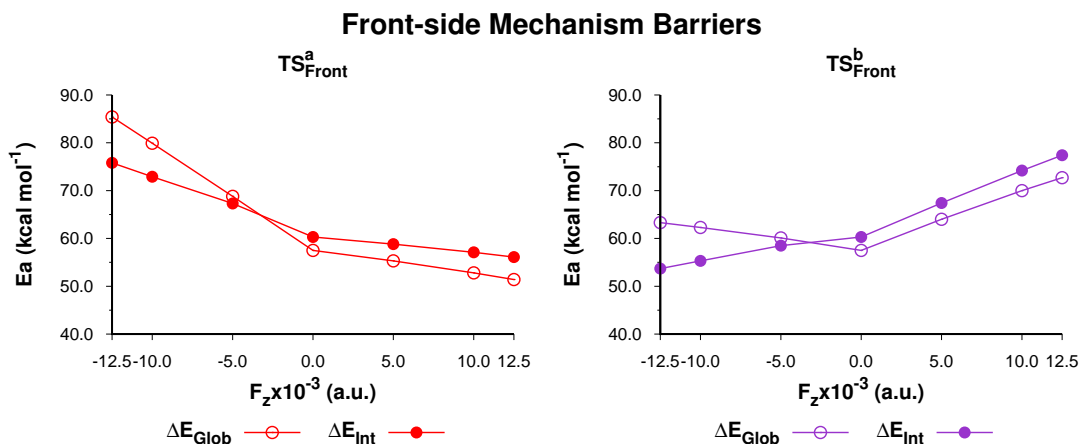


Figure 2.24: $\Delta E_{\text{Int}}^{\neq}$ and global barriers ($\Delta E_{\text{Glob}}^{\neq}$) of the *front-side* mechanism as function of the field intensity in the scanned range $R(F_z, 10^{-3} \text{ a.u.})$. On the left. $\text{TS}_{\text{Front}}^{\text{a}}$. On the right. $\text{TS}_{\text{Front}}^{\text{b}}$.

Positive Field Region. The calculated barriers, reported in Figure 2.24, show that $F_z = 12.5 \times 10^{-3} \text{ a.u.}$ along the reaction axis acts by lowering the internal barrier by $4.2 \text{ kcal mol}^{-1}$. This stabilization is much lower than the one obtained for TS_{Back} ($22.3 \text{ kcal mol}^{-1}$).

Furthermore, the lack of **Rx1**, in the positive field region, means that the trajectory of the ammonia toward the methyl chloride to reach TS_{Front} requires to deviate against the field. On the contrary, at negative fields value **Rx1** is the most stable reactant complex and **Rx2** structure lacks. The field-induced trajectory of ammonia assists TS_{Front} .

From Figure 2.24 it is possible to note that $\text{TS}_{\text{Front}}^{\text{a,b}}$ show an opposite trends. This difference is due to the relative orientation of nucleophile and leaving group. During the front mechanism, the entering ammonia and the leaving group have non linear trajectory. During *back-side* mechanism, the trajectory of the entering and leaving groups is straight. During *front-side* mechanism, the OEEF will support only one of the internal coordinate which composes the reaction coordinate and will destabilize the other one. $\text{TS}_{\text{Front}}^{\text{a}}$ is subject to an OEEF which stabilizes the exit of the chloride anion and hinders the enter of ammonia. The dominant contribution of C–Cl internal coordinate implies that positive field values, which support the C–Cl bond breaking, provide a stabilisation of $\text{TS}_{\text{Front}}^{\text{a}}$.

The opposite holds for $\text{TS}_{\text{Front}}^{\text{b}}$ this effect destabilises the transition state structure.

Differently from *back-side* mechanism, *positive field values can both catalyze and inhibit the front-side mechanism, depending on the orientation of the C–Cl and C–N bonds with respect to the positive field*. Again, the induced dipole moment analysis rationalises these results.

	MeCl	NH ₃	MeCl + NH ₃	Rx1	Rx2	TS _{Front} ^a	TS _{Front} ^b
$F_z = 0.0 \text{ a.u.}$	-2.11	-1.73	-3.84	-0.04	-4.32	-5.45	-1.59
$F_z = -12.5 \times 10^{-3} \text{ a.u.}$	-1.10	-2.22	-3.32	0.94		-3.45	3.84
$\Delta\mu_z \text{ (D)}$	-1.01	0.49	-0.52	0.90		-2.00	5.43
$F_z = 0.0 \text{ a.u.}$	-2.11	-1.73	-3.84	-0.04	-4.32	-5.45	-1.59
$F_z = -12.5 \times 10^{-3} \text{ a.u.}$	-3.14	-2.22	-5.36		-6.18	-7.86	-1.10
$\Delta\mu_z \text{ (D)}$	1.03	0.49	1.52		1.86	2.41	0.49

Table 2.11: Induced dipole moment along z-axis: μ_z (D) of methyl chloride, ammonia, reactants, \mathbf{Rx} , $\mathbf{TS}_{\text{Front}}^{\text{a}}$ and $\mathbf{TS}_{\text{Front}}^{\text{b}}$ when $F_z = 0.0$ to $\pm 12.5 \times 10^{-3} \text{ a.u.}$. The forth and the last rows is the induced dipole moment variation $\Delta\mu_z$ (D) per critical point.

In the positive field region: $(\Delta\mu_z(\mathbf{TS}_{\text{Front}}^{\text{a}}), 2.41 \text{ D}) > (\Delta\mu_z(\mathbf{Rx2}), 1.86 \text{ D}) > (\Delta\mu_z(\text{MeCl} + \text{NH}_3), 1.53 \text{ D}) > (\Delta\mu_z(\mathbf{TS}_{\text{Front}}^{\text{b}}), 0.49 \text{ D})$. The trend of induced dipole moment variation justifies the inverted trend of reaction barriers.

Note that $(\Delta\mu_z(\text{MeCl} + \text{NH}_3))$ is the one calculated at positive field. Global barriers are referred to the same but positive field value to take into account E_{Reorg} .

Negative Field Region. Negative field values act oppositely, destabilising $\mathbf{TS}_{\text{Front}}^{\text{a}}$. In the negative field region: $(\Delta\mu_z(\mathbf{TS}_{\text{Front}}^{\text{b}}), 5.43 \text{ D}) > (\Delta\mu_z(\text{MeCl} + \text{NH}_3), 1.53 \text{ D}) > (\Delta\mu_z(\mathbf{Rx1}), 0.90 \text{ D}) > (\Delta\mu_z(\mathbf{TS}_{\text{Front}}^{\text{a}}), -2.00 \text{ D})$. This trend justifies the lowered internal barrier passing through $\mathbf{TS}_{\text{Front}}^{\text{b}}$ and the increased internal barrier passing through $\mathbf{TS}_{\text{Front}}^{\text{a}}$ (Table 2.11).

The calculated data for both *back* and *front-side* mechanisms allow an overall comparison of the OEEFs effects on the kinetics of Menshutkin reaction. Figure 2.25 shows the ratio between all the calculated barriers.

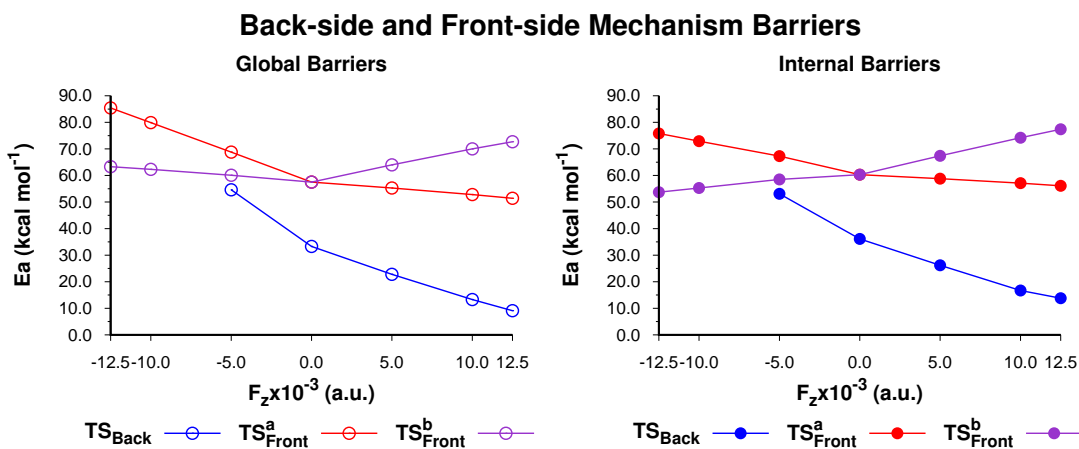


Figure 2.25: Global ($\Delta E_{\text{Glob}}^{\ddagger}$) barrier of *back-side* and *front-side* mechanism as function of the field intensity in the scanned range $R(F_z, 10^{-3} \text{ a.u.})$ (left); internal ($\Delta E_{\text{Int}}^{\ddagger}$) barrier of *back-side* and *front-side* mechanism as function of the field intensity in the scanned range $R(F_z, 10^{-3} \text{ a.u.})$. (right) for the Menshutkin reaction between methyl chloride and ammonia.

Even if TS_{Back} structure at $F_z < -5.0 \times 10^{-3} a.u.$ does not exist, it is possible to virtually see, from the trends, an intersection which means a mechanistic switch from the *back-side* to *front-side* mechanism.

Figure 2.25 shows that *Menshutkin reaction occurs with back-side mechanism in the absence of OEEFs. Positive field values strongly catalyse back-side mechanisms. However, when $F_z < -5.0 \times 10^{-3} a.u.$ the back-side mechanism is inhibited and, only the front-side mechanism can occur.* Shaik and co-workers published analogous results in 2018, while these results were already obtained. They demonstrated that: "EEFs can also catalyze the frontside nucleophilic displacement reaction, thus violating the Walden-inversion paradigm." [61]. Other than catalysis/inhibition on Menshutkin reaction, the authors show how an OEEF can affect the electronic structure of reactants if they are anchored to a gold cluster which is used to carry out OEEF-catalysed reaction experimentally. In particular, gold thiolate moiety can alter the spin state of reactants, while an OEEF is applied, leading to a ground open-shell singlet state due to the charge transfer from gold to reactants. [61] This process catalyses the reaction and makes gold thiolate, if present, a sort of co-catalyst which provides an additional effect. However, the pure effect of OEEFs without considering gold thiolate was investigated too, confirming the results obtained during this PhD.

Product Complexes. Finally, product complexes were fully re-optimised in the presence of OEEFs. Three different reactant complexes were evaluated under the influence of OEEFs, namely **Pd1**, **Pd2** and **Pd3** (Figure 2.26).

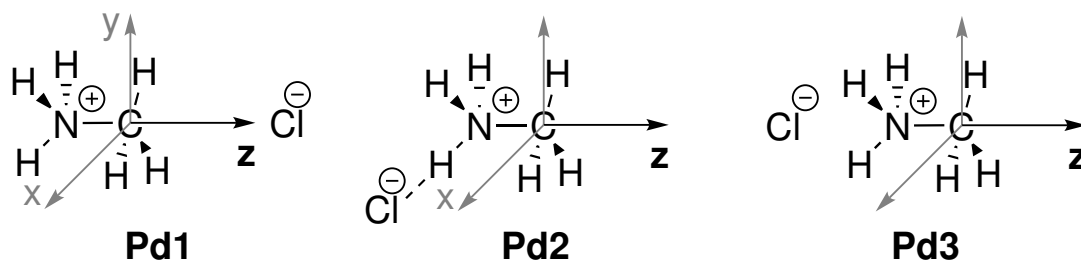


Figure 2.26: The x-,y-,z-directions for **Pd1**, **Pd2**, **Pd3**.

As a consequence of type II substitution, product complexes are charged. Charged products display a higher sensitivity to OEEFs. At positive field values, **Pd1** is the only on stable complex thanks to the alignment along the z-axis of the system dipole and hence, this critical point is stabilised. At negative field values,

Pd3 structure is the only one stable complex thanks to the counterbalance between the applied field and the electrostatic interaction between chloride anion and ammonium cation. **Pd2**, the most stable complex in absence of OEEFs, is also the most "fragile" complex and was not isolated in presence of OEEFs (Tables 2.12).

A negative field is a destabilising perturbation (in the chosen Cartesian system)

Complex Type	Pd3			Pd2	Pd1		
$F_z(10^{-3} a.u.)$	-12.5	-10.0	-5.0	0.0	5.0	10.0	12.5
$E(\text{kcal mol}^{-1})$	9.5	7.0	1.5	-3.7	-3.4	-4.2	-4.7
R(N-C) (Å)	3.57	3.36	3.33	3.32	3.04	3.01	2.98
R(C-Cl) (Å)	1.78	1.78	1.79	1.79	1.81	1.82	1.83
q(N) (a.u.)	-1.09	-1.09	-1.08	-1.09	-1.07	-1.08	-1.09
q(C) (a.u.)	-0.58	-0.57	-0.56	-0.56	-0.52	-0.51	-0.50
q(Cl) (a.u.)	-0.03	-0.04	-0.05	-0.07	-0.13	-0.16	-0.18

Table 2.12: Bond lengths (R) and partial charges (q) of **Pd1**, **Pd2**, **Pd3** at different intensities of the OEEF along the z-axis. Relative energies refer to the most stable **Pd**.

and the system needs to arrange into a geometry which is less sensitive to the applied field. On the contrary, positive field region is stabilising because the system can align its dipole with it. **Pd1** represents the geometry which can better interact with the field to maximise the stabilisation. The geometry changes, from negative to positive fields, correspond to the switch from a geometry which can poorly interact with a destabilising field, to a geometry which can strongly interact with a stabilising field.

The OEEF effects analysis allows to figure out Menshutkin reaction mechanism changes, depending on the field intensity and orientation (Figure 2.27).

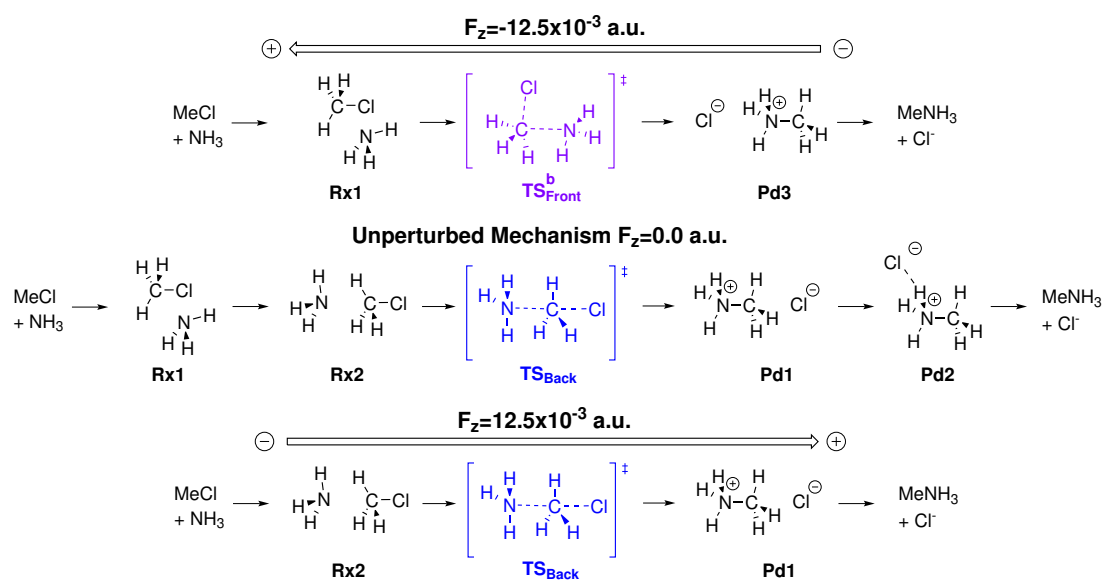


Figure 2.27: Reaction mechanism of Menshutkin reaction in presence of OEEFs. $F_z = 12.5 \times 10^{-3} \text{ a.u.}$ (top), $F_z = 0.0 \text{ a.u.}$ (middle) $F_z = 12.5 \times 10^{-3} \text{ a.u.}$ (bottom).

2.3 Electrocyclic Reactions

2.3.1 Introduction

Electrocyclic reactions are a class of pericyclic reactions. In this case study, the ring opening of substituted cyclobutene molecules was considered. Cyclobutene ring opening involves 2σ electrons and 2π electrons which become 4π electrons leading to the formation of butadiene.

Electrocyclic reactions are depicted as being concerted and the understanding of its mechanism can be done by means of Woodward-Hoffmann (WH) rules. [62] The basic concept of WH theory, *i.e.* the conservation of orbital symmetry in the reactant-product transformation, establishes that the thermal ring-opening of cyclobutene must proceed in a *conrotatory* manner. If the substituents on sp^3 carbon atoms rotate in the same direction the ring opening is called *conrotatory*, while if the substituents on sp^3 carbon atoms rotate in opposite direction the ring opening is called *disrotatory* (Figure 2.28).

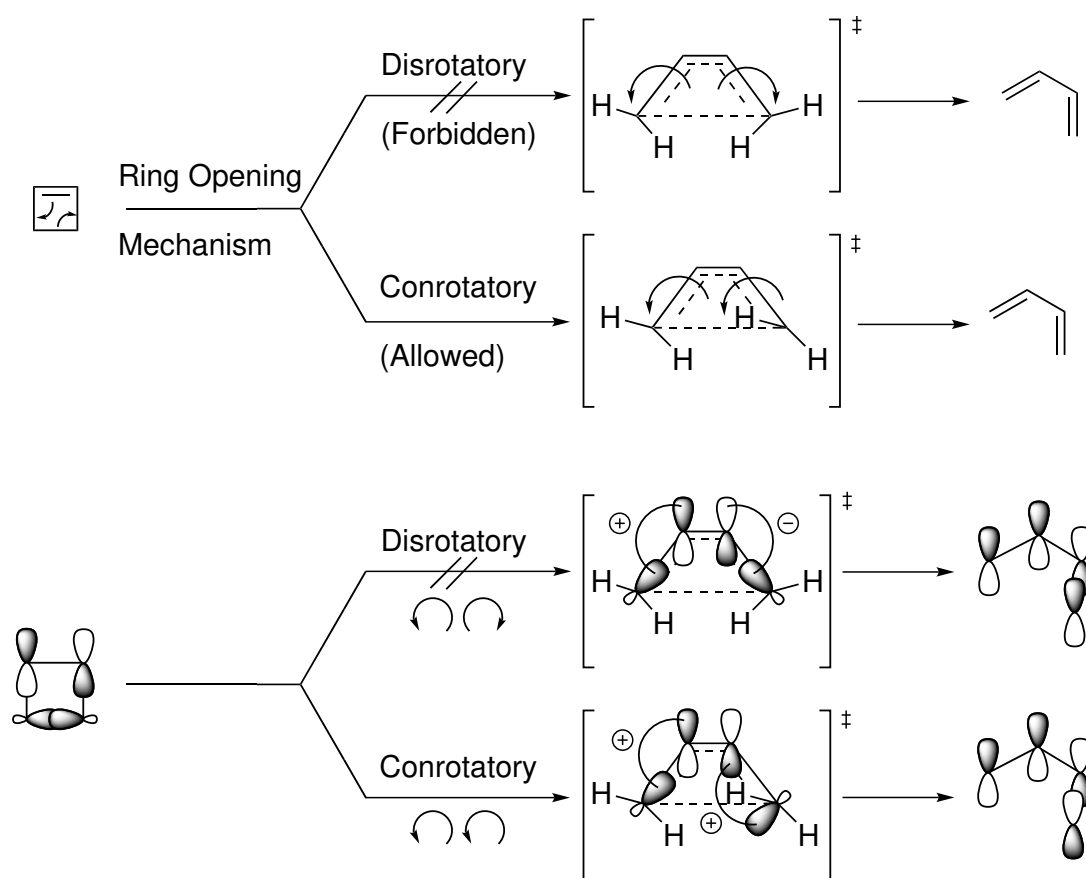


Figure 2.28: Possible ring opening mechanisms for the 4-electron electrocyclic ring opening of cyclobutene: a *disrotatory* mechanism (forbidden) and a *conrotatory* mechanism (allowed).

Frontier Molecular Orbital (FMO) theory states that the total energy change of the reactants on approach of the transition state is described by the Klopman-Salem equation, derived from perturbation MO theory. HOMO-LUMO interaction is considered primary, based on the fact that the largest contribution in the filled-unfilled interaction term of the Klopman-Salem equation derives from molecular orbitals that are the closest in energy. From these observations, FMO theory simplifies the prediction of reactivity to the analysis of the interaction between the more energetically matched HOMO-LUMO pairing of the two reactants.

Woodward-Hoffmann rules and the FMO theory both state that for pericyclic reaction there is a conservation of the orbital symmetry. This rule implies that for a 4-electrons electrocyclic ring opening, the *disrotatory* mechanism is forbidden and only the *conrotatory* mechanism can occur (Figure 2.28).

By considering only the allowed *conrotatory* mechanism, it is possible to evaluate two different types of ring opening, with different stereochemistry, depending on the direction of rotation of the two dihedral angles. These rotations are called *inward* and *outward* rotation. Especially for substituted cyclobutenes, the different rotation implies a different stereochemistry of the product (Figure 2.29).

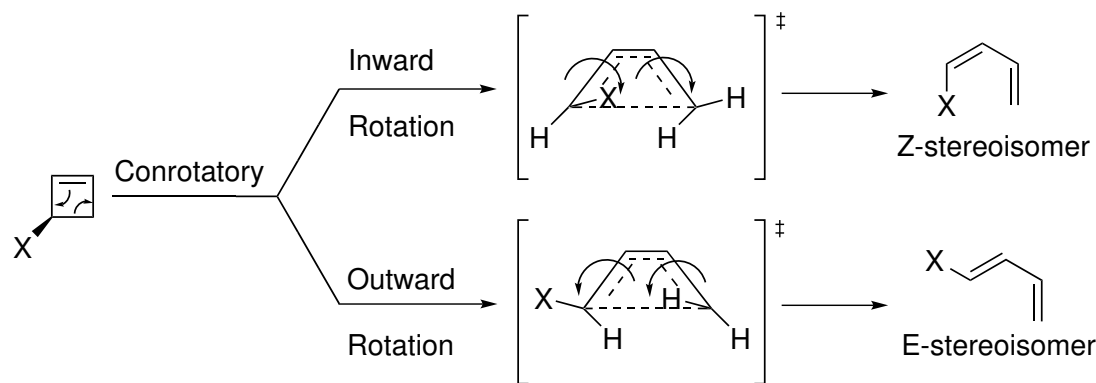


Figure 2.29: Possible rotations for the allowed *conrotatory* mechanism. An *inward* and a *outward* rotation could occur

Previous research demonstrated that the nature of the X group can affect the rotation, and this phenomenon is called *torquoselectivity*. [63–67] Based on these rules, it is possible to predict the reaction mechanism and its stereochemistry. Differently from the WH rules, which depend on the number of π -electrons, the *torquoselectivity* seems more manipulable, depending on the chemical nature of the X group. For this reason, it is not possible to obtain a substituted diene with a stereochemistry opposite to the natural stereochemistry allowed for that X group, due to the *torquoselectivity* principle. Thanks to the functional group interconversion, it is possible to produce the desired alkene, even if extra steps

in the synthetic route are necessary. Kinetics and thermodynamics studies, on various 3 and 3,4-disubstituted cyclobutenes, questioned this interpretation. In a series of papers, [63–67] Houk and co-workers carried out systematic theoretical investigations on the *conrotatory* ring opening of 3 and 3,4-disubstituted cyclobutenes showing that donor substituents favor *outward* rotation while, with strong acceptors, the *inward* rotation is preferred. They rationalized these results in terms of FMO theory. Eventually, it became definitively clear that electronic effects, and not steric effects, are dominant in determining the stereochemical output of the ring opening of substituted cyclobutenes.

It is evident that *torquoselectivity* can be circumvented with different approaches; hence the question is if OEEFs can be used to change the *torquoselectivity* of the reaction and more generally to catalyze the ring opening reaction for the case of monosubstituted cyclobutenes. OEEFs demonstrated to be a tool which can change reaction paths, both from computational and experimental studies. The interaction of the field with the reactants dipole moment can modify the favoured orientation of the molecules and modify the reaction channel. An example is the Diels-Alder reaction between cyclopentadiene and maleic anhydride: the application of an OEEF along a direction which is perpendicular to the “reaction axis” induces the formation of the *endo* product instead of the favourite *exo* product, thanks to the interaction between the field and the molecular dipole. [36] Other than *exo/endo* selectivity, alternate OEEFs can also induce the formation of a single enantiomer product. [37] Moreover the catalytic effect of OEEF has been recently experimentally demonstrated, corroborating the role of dipole moment as a valuable descriptor of how OEEFs modify the reaction profiles. [41]

The present study aims to show, by means of DFT computational approach, the effect of OEEFs on the kinetics and mechanism of conversion reaction of 3-substituted cyclobutenes to butadienes and their effect on the stereochemical output.

2.3.2 Results and Discussion

The influence of OEEFs is examined along the three Cartesian axes (in positive and negative directions) on the *conrotatory* ring opening of 3-substituted cyclobutenes (Figure 2.30).

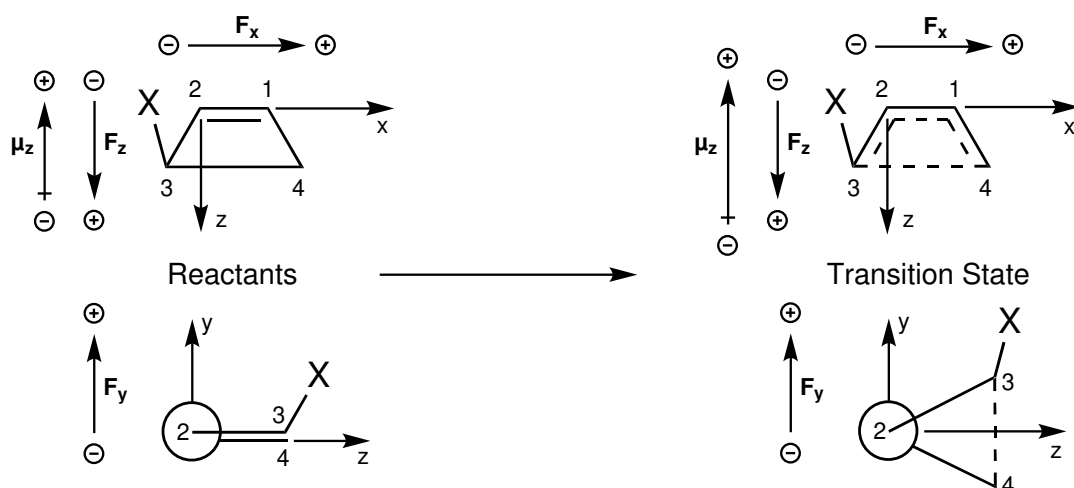


Figure 2.30: The orientation of the coordinate system and applied field and representation of the induced dipole moment in reactants (**R_x**) and transition state (**TS**). Two different perspectives are given: along the y-axis (top) and along the x-axis (bottom). The relative orientations of the electric field F_z (positive) and dipole μ_z (negative) shown in the picture stabilize the system. The increase of the dipole from reactants to transition state (top) stabilizes more **TS** than **R_x** and lowers the activation barrier

The x-axis is centered on carbon atom 2 and coincides with the C1-C2 double bond. The z-axis is defined in such a way that in transition states and products (where the structure is not planar) lay in a plane bisecting the C4-C1-C2-C3 dihedral angle (Figure 2.30). In the same scheme the positive direction (following the convention of Gaussian09) for the applied field along the three axes is schematically represented.

If a positive field is oriented along z-axis ($F_z > 0$) and the molecular dipole moment is oppositely aligned along the same axis (μ_z), this relative orientation stabilizes the molecular system. Thus, if such dipole, increases on passing from reactants to transition state, the effect of the OEEF is a stronger stabilization of transition state with respect to reactants with a consequent decrease of the activation barrier (catalysis). *Vice versa*, a decrease of the dipole component causes an increase of the activation barrier (inhibition). In the absence of OEEF, the *inward* and *outward conrotatory* ring opening of cyclobutene is degenerate, and the value of the energy barrier (ΔE^\ddagger) is 36.6 kcal mol⁻¹ while the reaction energy (ΔE_{React}) is -7.6 kcal mol⁻¹: The ring opening of cyclobutene is practically insensitive to the presence of OEEF.

The importance of the Cartesian system was already underlined during the investigation of the OEEFs effects on substitution reactions. However, the reaction coordinate in the transition state is not dominated by internal coordinates belonging to the stretching of breaking and forming bonds, as in substitution reaction.

Electrocyclic reaction transition states have an important contribution in the dihedral rotation C4-C1-C2-C3. This contribution generates difficulties in the identification of the reaction axis and require a more detailed analysis of OEEF orientations. Hence, this investigation also required additional attentions on the x-axis and y-axis definition.

Moreover, due to the mono-molecularity of the reaction, instead of the well-known bi-molecularity of S_N2 reactions, a single and more general activation energy (ΔE^\ddagger) was calculated.

2.3.2.1 Electron-Donor Substituents

In absence of OEEF, for both CH_3 and NH_2 , the *outward* rotation is favoured and the energetic preference to rotate *outward* increases as the π -donor nature of the substituent increases: for CH_3 (a weak donor) the *outward* and *inward* activation barriers (ΔE^\ddagger) are 35.1 and 41.1 kcal mol⁻¹, while for NH_2 (a strong π -donor) these values become 24.3 and 40.8 kcal mol⁻¹, respectively (Figure 2.31).

X=CH₃. Positive fields along x-axis catalyse the reaction (the barrier for the preferred *outward* rotation changes from 35.1 to 31.9 kcal mol⁻¹ at $F_x = 15.0 \times 10^{-3} a.u.$), while negative values leave the activation barrier almost unchanged (35.2 kcal mol⁻¹ at $F_x = -15.0 \times 10^{-3} a.u.$). The effect of the applied field is almost negligible or very small along y-axis and z-axis. In the former case the *outward* barrier becomes 34.8 kcal mol⁻¹ (TS_{Out} , $F_y = -15.0 \times 10^{-3} a.u.$) and 35.2 kcal mol⁻¹ ($\Delta E^\ddagger(\text{TS}_{\text{Out}})$, $F_y = 15.0 \times 10^{-3} a.u.$). In the latter case the corresponding values are 33.1 kcal mol⁻¹ and 35.7 kcal mol⁻¹ (Figure 2.32 and Table 2.13).

The trends observed above for the two electron-donating substituents, are readily explained by the different polarization (and the consequent change of the induced dipole) of reactants (\mathbf{Rx}) and transition state (\mathbf{TS}) when negative or positive fields are applied.

For $\text{X}=\text{CH}_3$ and $F_x = 15.0 \times 10^{-3} a.u.$, the induced dipole along x-axis is negatively oriented and stabilizing. Since its value changes from -2.56 to -3.87 D, the induced dipole (*i.e.* the effect of polarization) has a more relevant stabilising effect on the transition state (TS_{Out}) with respect to the reactants (\mathbf{Rx}), with a consequent decrease of the activation barrier similarly to what happens in enzymes. [68, 69] Small changes of the induced dipole are observed along y (from -2.03 to -1.98 D) and z-axis (from -2.05 to -1.99 D). Small changes of the dipole characterize the application of negative fields along the three directions. In all cases very small changes of the activation barrier were computed.

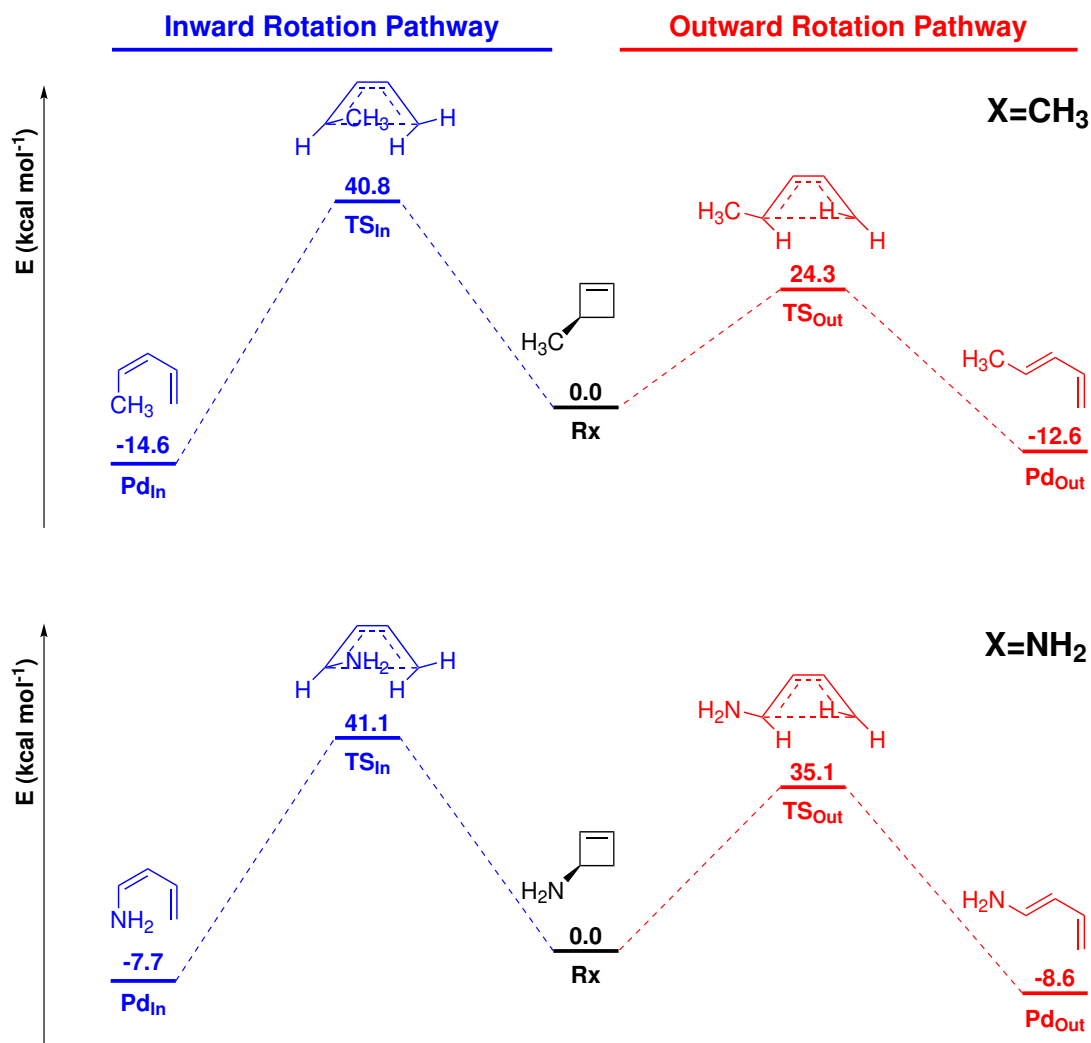


Figure 2.31: Reaction profiles (kcal mol⁻¹) for the *conrotatory* (*inward* and *outward* rotation pathways) ring opening reaction of 3-methylcyclobutene and 3-aminocyclobutene in the absence of OEEF.

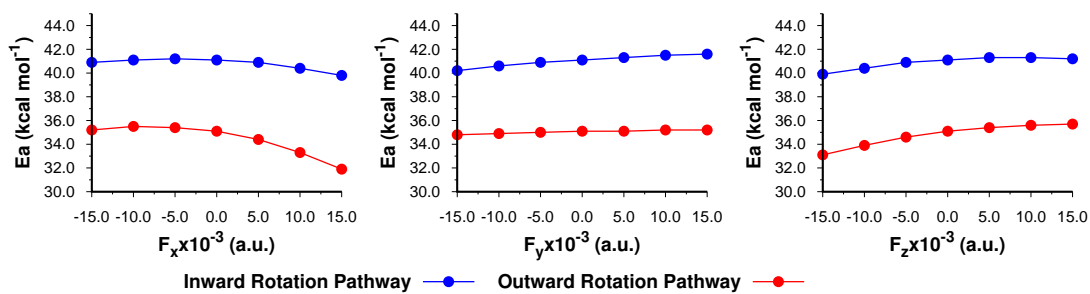


Figure 2.32: Activation energies (ΔE^\ddagger , kcal mol⁻¹) for the *conrotatory* ring opening reaction of 3-methylcyclobutene as a function of the applied field along the three axes ($F, 10^{-3} a.u.$). In red *outward* rotation pathway (TS_{Out}), in blue *inward* rotation pathway (TS_{In}).

$(F, 10^{-3}a.u.)$		-15.0	-10.0	-5.0	0.0	5.0	10.0	15.0
X-Axis	TS _{In}	40.9	41.1	41.2	41.1	40.9	40.4	39.8
	TS _{Out}	35.2	35.5	35.4	35.1	34.4	33.3	31.9
	Pd _{In}	-8.0	-7.8	-7.7	-7.7	-7.9	-8.2	-8.8
	Pd _{Out}	-8.3	-8.1	-8.2	-8.6	-9.3	-10.3	-11
Y-Axis	TS _{In}	40.2	40.6	40.9	41.1	41.3	41.5	41.6
	TS _{Out}	34.8	34.9	35.0	35.1	35.1	35.2	35.2
	Pd _{In}	-8.4	-8.1	-7.9	-7.7	-7.5	-7.3	-7.0
	Pd _{Out}	-9.1	-8.9	-8.7	-8.6	-8.4	-8.2	-8.1
Z-Axis	TS _{In}	39.9	40.4	40.9	41.1	41.3	41.3	41.2
	TS _{Out}	33.1	33.9	34.6	35.1	35.4	35.6	35.7
	Pd _{In}	-8.3	-8.0	-7.8	-7.7	-7.7	-7.8	-8.0
	Pd _{Out}	-8.3	-8.3	-8.4	-8.6	-8.7	-9.0	-9.2

Table 2.13: Activation energies (ΔE^\ddagger , kcal mol⁻¹) and reaction energies (ΔE_{React} for the *conrotatory* ring opening of 3-methylcyclobutene at different fields ($F, 10^{-3}a.u.$) applied along the three Cartesian axes.

X=CH ₃							
Field Intensity	Axis	Rx	TS _{In}	TS _{Out}	Pd _{In}	Pd _{Out}	
$F = 15.0 \times 10^{-3}a.u.$	x	-2.56	-3.18	-3.87	-3.14	-3.94	μ_x
	y	-2.03	-1.97	-1.99	-1.84	-1.88	μ_y
	z	-2.05	-2.15	-1.99	-2.25	-2.24	μ_z
$F = 0.0 a.u.$	x	-0.06	-0.20	-0.46	-0.15	-0.50	μ_x
	y	-0.03	0.16	0.06	0.13	0.10	μ_y
	z	0.22	0.39	0.53	0.26	0.10	μ_z
$F = -15.0 \times 10^{-3}a.u.$	x	2.43	2.70	2.74	2.70	2.76	μ_x
	y	1.98	2.32	2.02	2.26	2.17	μ_x
	z	2.49	3.02	3.21	2.82	2.48	μ_x

Table 2.14: Induced dipole ($\mu_{x,y,z}$) along the direction of the applied field ($F_{x,y,z}, 10^{-3}a.u.$) for the various critical points located for the thermal ring-opening of 3-methylcyclobutene.

X = NH₂. The effect of the OEEF is more pronounced. This is consistent with the stronger π -donor character of NH₂ and the consequent increase of electron density on the cyclobutene ring, allowing a stronger polarization when the external field is applied.

The most important catalytic effect is observed on the *outward* mechanism when positive fields are applied along the x direction. When $F_x = 15.0 \times 10^{-3}a.u.$, $\Delta E^\ddagger(\text{TS}_{\text{Out}})$ varies from 24.3 to 17.7 kcal mol⁻¹. Smaller catalytic effects are observed for negative values of the field along y and z, the corresponding activation energies (ΔE^\ddagger) being 22.9 and 20.6 kcal mol⁻¹. Furthermore, the reaction is inhibited when negative fields are applied along x-axis ($\Delta E^\ddagger = 30.1$ kcal mol⁻¹) and positive fields are applied along y-axis and z-axis ($\Delta E^\ddagger = 26.4$ and 30.2 kcal mol⁻¹) (Figure 2.33 and Table 2.15).

When $F_x = 15.0 \times 10^{-3}a.u.$, the x component of the induced dipole is -

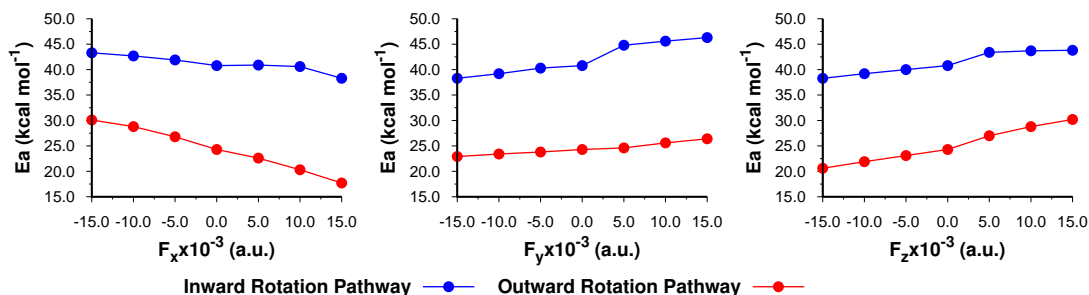


Figure 2.33: Activation energies (ΔE^\ddagger , kcal mol⁻¹) for the *conrotatory* ring opening reaction of 3-aminocyclobutene as a function of the applied field along the three axes ($F, 10^{-3}a.u.$). In red *outward* rotation pathway (TS_{Out}), in blue *inward* rotation pathway (TS_{In}).

	($F, 10^{-3}a.u.$)	-15.0	-10.0	-5.0	0.0	5.0	10.0	15.0
X-Axis	TS_{In}	43.3	42.7	41.9	40.8	40.9	40.6	38.3
	TS_{Out}	30.1	28.8	26.8	24.3	22.6	20.3	17.7
	Pd_{In}	-8.3	-10.1	-12.2	-14.6	-15.5	-16.5	-17.8
	Pd_{Out}	-4.8	-6.8	-9.4	-12.6	-15.4	-18.4	-22.4
Y-Axis	TS_{In}	38.3	39.2	40.3	40.8	44.8	45.6	46.3
	TS_{Out}	22.9	23.4	23.8	24.3	24.6	25.6	26.4
	Pd_{In}	-18.8	-17.4	-16.0	-14.6	-16.5	-16.8	-17.0
	Pd_{Out}	-17.0	-15.6	-14.3	-12.6	-14.8	-15.0	-15.2
Z-Axis	TS_{In}	38.3	39.2	40.0	40.8	43.4	43.7	43.8
	TS_{Out}	20.6	21.9	23.1	24.3	27.0	28.8	30.2
	Pd_{In}	-17.0	-15.8	-15.0	-14.6	-12.8	-11.2	-9.9
	Pd_{Out}	-13.5	-13.1	-12.9	-12.6	-12.0	-11.0	-10.2

Table 2.15: Activation energies (ΔE^\ddagger , kcal mol⁻¹) and reaction energies (ΔE_{React} , kcal mol⁻¹) for the *conrotatory* ring opening of 3-aminocyclobutene at different fields ($F, 10^{-3}a.u.$) applied along the three Cartesian axes.

X=NH ₂							
	Axis	Rx	TS _{In}	TS _{Out}	Pd _{In}	Pd _{Out}	
$F = 15.0 \times 10^{-3}a.u.$	x	-3.16	-6.04	-5.39	-4.47	-6.92	μ_x
	y	-3.17	-2.60	-2.53	-3.38	-3.41	μ_y
	z	-3.47	-3.44	-2.47	-2.58	-2.88	μ_z
$F = 0.0 a.u.$	x	1.22	0.16	-1.13	-0.81	-1.73	μ_x
	y	0.12	0.38	0.52	1.28	0.58	μ_y
	z	0.55	1.10	1.50	0.72	0.72	μ_z
$F = -15.0 \times 10^{-3}a.u.$	x	3.84	3.46	2.92	2.48	2.49	μ_x
	y	2.23	3.57	2.54	3.37	3.42	μ_x
	z	3.02	3.86	4.05	4.12	3.30	μ_x

Table 2.16: Induced dipole ($\mu_{x,y,z}$) along the direction of the applied field ($F_{x,y,z}, 10^{-3}a.u.$) for the various critical points located for the thermal ring-opening of 3-aminocyclobutene.

3.16 D in \mathbf{R}_x and its absolute value increases significantly in \mathbf{TS}_{Out} (-5.39 D). This stabilizes significantly the transition state and explains the significant catalytic effect of OEEF ($\Delta E^\ddagger = 17.7 \text{ kcal mol}^{-1}$). Inhibition and catalysis observed along y-axis and z-axis for positive and negative values of the applied field can be similarly explained. For instance, the considerable inhibition observed for $F_x = -15.0 \times 10^{-3} a.u.$ is determined by an induced dipole which is positively oriented and changes from 3.84 (\mathbf{R}_x) to 2.92 D (\mathbf{TS}_{Out}), causing a destabilization of the transition state. A positively oriented dipole along z-axis, which increases from 3.02 (\mathbf{R}_x) to 4.05 D (\mathbf{TS}_{Out}), explains likewise the catalytic effect for $F_z = -15.0 \times 10^{-3} a.u.$

Interestingly, the effect of the electric field along x-axis and z-axis is significantly more relevant than along y-axis. Since the molecular frame is approximately planar, in the presence of the electric field the change of polarization from reactants to transition state mainly involves the x and z directions. The change of polarization along y-axis depends mainly on the position of the NH_2 group in \mathbf{R}_x and \mathbf{TS}_{Out} . However, this position does not change dramatically and the effect of polarization along y-axis is much less important. For instance, for $F_y = -15.0 \times 10^{-3} a.u.$, the C1-C4-N angle and the torsion C2-C1-C4-N are 115.5° and 127.6° in \mathbf{R}_x and 121.2° and 138.2° in \mathbf{TS}_{Out} ; in accordance with these structural parameters only a small change of the dipole along y direction (from 2.23 to 2.54 D) was observed.

For $X=\text{NH}_2$, positive fields along the x-axis and negative fields along y and z-axis catalyse both inward and outward mechanisms. Negative fields along the y and z-axis and positive field along x-axis inhibit both inward and outward mechanisms.

2.3.2.2 Electron-Acceptor Substituents

It was demonstrated that π -acceptor substituents can reverse the ratio between *outward* and *inward* rotation, the latter becoming competitive with the former. This trend is evident from these results: for $X=\text{CHO}$ the *inward* and *outward* activation barriers are 29.2 and 34.2 kcal mol^{-1} , respectively, for $X=\text{NO}$ they are 28.6 and 32.8 kcal mol^{-1} , while for $X=\text{BH}_2$ (a rather strong π -acceptor) they become 13.6 and 32.3 kcal mol^{-1} (Figure 2.34). This finding agrees with the experimental evidence and previous computational results reported by Houk and co-workers. [63–67]

X = CHO. Positive and negative fields along x-axis inhibit the reaction (the barrier for the preferred *inward* rotation changes from 29.2 to 34.6 kcal mol^{-1} for

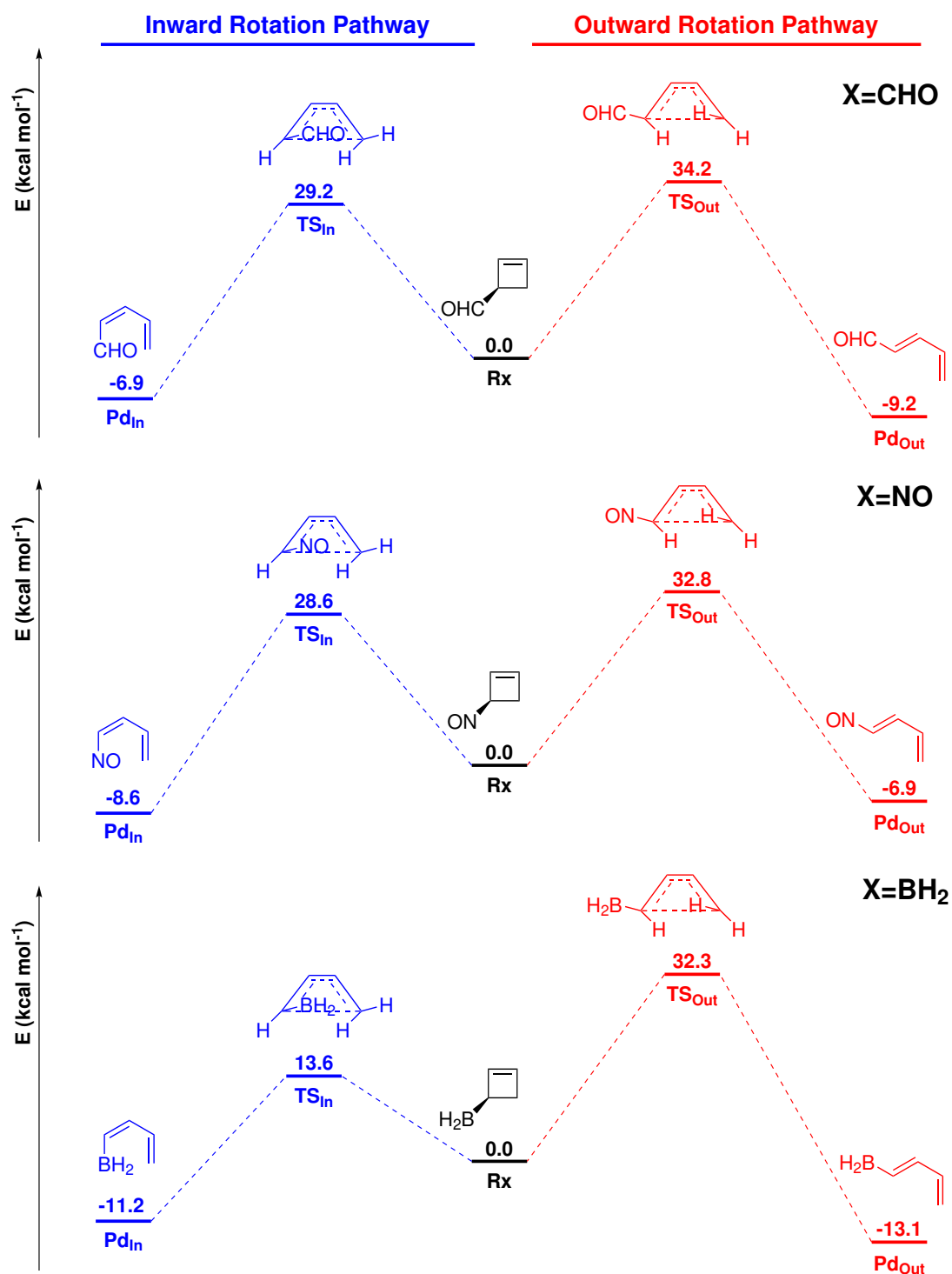


Figure 2.34: Activation energies (ΔE^\ddagger , kcal mol⁻¹) for the *conrotatory* ring opening reaction of a) 3-nitrosocyclobutene; b) cyclobut-2-en-1-ylborane and c) 3-formylcyclobutene, as a function of the applied field along the three axes (F , $10^{-3}a.u.$).

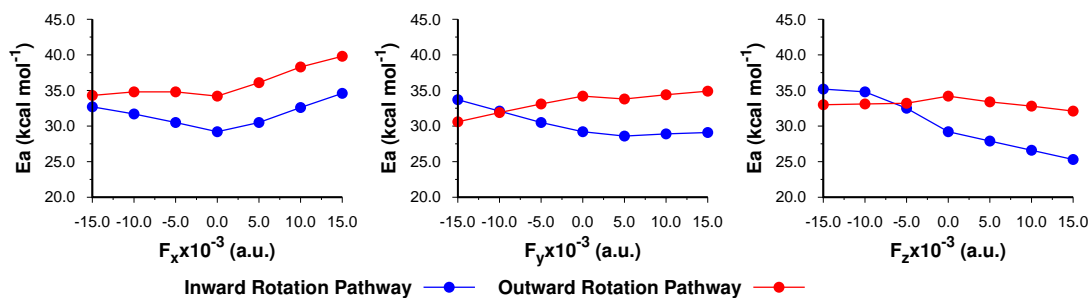


Figure 2.35: Activation energies (ΔE^\ddagger , kcal mol⁻¹) for the *conrotatory* ring opening reaction of 3-formylcyclobutene, as a function of the applied field along the three axes (F , $10^{-3}a.u.$). In red *outward* rotation pathway (TS_{Out}), in blue *inward* rotation pathway (TS_{In}).

	(F , $10^{-3}a.u.$)	-15.0	-10.0	-5.0	0.0	5.0	10.0	15.0
X-Axis	TS_{In}	32.7	31.7	30.5	29.2	30.5	32.6	34.6
	TS_{Out}	34.3	34.8	34.8	34.2	36.1	38.3	39.8
	Pd_{In}	-7.7	-7.8	-8.2	-6.9	-6.6	-3.8	-1.5
	Pd_{Out}	-12.5	-10.7	-9.7	-9.2	-6.3	-3.0	-0.2
Y-Axis	TS_{In}	33.7	32.1	30.5	29.2	28.6	28.9	29.1
	TS_{Out}	30.6	31.9	33.1	34.2	33.8	34.4	34.9
	Pd_{In}	-10.2	-9.3	-8.8	-8.7	-13.5	-15.7	-18.6
	Pd_{Out}	-17.2	-15.0	-12.9	-9.2	-9.9	-8.4	-7.2
Z-Axis	TS_{In}	35.2	34.8	32.5	29.2	27.9	26.6	25.3
	TS_{Out}	33.0	33.1	33.2	34.2	33.4	32.8	32.1
	Pd_{In}	2.9	-0.8	-5.2	-8.7	-10.0	-11.3	-12.6
	Pd_{Out}	-13.6	-12.5	-11.4	-9.2	-11.0	-11.0	-11.0

Table 2.17: Activation energies (ΔE^\ddagger , kcal mol⁻¹) and reaction energies (ΔE_{React} , kcal mol⁻¹) for the *conrotatory* ring opening of 3-formylcyclobutene at different fields (F , $10^{-3}a.u.$) applied along the three Cartesian axes.

$F_x = 15.0 \times 10^{-3}a.u.$ and 32.7 kcal mol⁻¹ for $F_x = -15.0 \times 10^{-3}a.u.$. The reaction is also inhibited for negative fields along y and z-axis ($\Delta E^\ddagger = 33.7$ kcal mol⁻¹ when $F_y = -15.0 \times 10^{-3}a.u.$ and $\Delta E^\ddagger = 35.2$ kcal mol⁻¹ when $F_z = -15.0 \times 10^{-3}a.u.$). The effect of the field is negligible for positive fields along y direction, while a significant catalytic effect is observed for positive fields applied along the z-axis ($\Delta E^\ddagger = 25.3$ kcal mol⁻¹ when $F_z = 15.0 \times 10^{-3}a.u.$). These trends are evidenced in the diagrams of Figure 2.35, which highlight also a very interesting effect: for negative fields applied along y and z-axis the *outward* rotation becomes favoured. The effect begins to appear when $F_{y,z} = -10.0 \times 10^{-3}a.u.$, and $F_{y,z} = -15.0 \times 10^{-3}a.u.$ the effect is rather evident, the *outward* barriers being 30.6 (y) and 33.0 (z) kcal mol⁻¹ and the corresponding *inward* barriers 33.7 and 35.2 kcal mol⁻¹ (Figure 2.35 and Table 2.17).

These results can be rationalized in terms of the different polarization (and the consequent change of the induced dipole) of reactants and transition state in the presence of OEEF. In particular, the different induced dipole in the two transition states (*inward*, $\Delta E^\ddagger(\text{TS}_{\text{In}})$ and *outward*, $\Delta E^\ddagger(\text{TS}_{\text{Out}})$) with respect

X=CHO							
Field Intensity	Axis	R _x	TS _{In}	TS _{Out}	Pd _{In}	Pd _{Out}	
$F = 15.0 \times 10^{-3} a.u.$	x	-3.47	-1.87	-2.51	-1.87	-1.45	μ_x
	y	-4.85	-4.80	-4.42	-7.59	-4.14	μ_y
	z	-5.14	-6.32	-5.68	-6.24	-5.16	μ_z
$F = 0.0 a.u.$	x	2.44	1.36	2.61	2.03	2.76	μ_x
	y	-0.92	-1.96	-1.87	-1.03	-0.45	μ_y
	z	-1.90	-2.99	0.67	-3.06	1.61	μ_z
$F = -15.0 \times 10^{-3} a.u.$	x	5.77	5.09	6.46	5.92	7.55	μ_x
	y	2.20	0.79	3.19	3.13	4.14	μ_x
	z	3.44	3.18	3.60	0.86	4.41	μ_x

Table 2.18: Induced dipole ($\mu_{x,y,z}$) along the direction of the applied field ($F, 10^{-3}a.u.$) for the various critical points located for the thermal ring-opening of 3formylcyclobutene.

to reactants, can explain the inversion for the preferred rotation between *inward* and *outward* when F_y and $F_z = -15.0 \times 10^{-3}a.u.$

When $F_y = -15.0 \times 10^{-3}a.u.$, the *inward* transformation is strongly inhibited. Inhibition is due to a significant decrease of the positively oriented induced dipole along y on passing from reactants (+2.20 D) to transition state (+0.79 D), with a consequent decrease of stabilization. The effect is the opposite for the *outward* rotation, the corresponding barrier changing from 34.2 (no field) to 30.6 kcal mol⁻¹ (applied field). This catalytic effect is due to a significant increase of the positively oriented induced dipole which varies from 2.20 D (**R_x**) to 3.19 D (**TS_{Out}**). The final result is a preferred *outward* rotation. A similar argument can be used to explain the inversion when $F_z = -15.0 \times 10^{-3}a.u.$ The inhibition for the *inward* rotation is even stronger and is caused by a decrease of the positively oriented dipole along z from 3.44 D (**R_x**) to 3.18 D (**TS_{In}**). The simultaneous decrease of the barrier for the *outward* process (from 34.2 to 33.0 kcal mol⁻¹) is equally explained by an increase of the dipole that becomes 3.60 D in the **TS_{Out}**. Contrary to what observed for X=NH₂, in the case of X=CHO the effect of the field applied along y-axis is rather important. This reflects the significant change of the position of the CHO group in the *inward* and *outward* transition states with respect to reactants.

For X=CHO, OEEFs can both catalyse and inhibit the inward rotation pathway. Moreover, negative fields along y and z-axis lead to the mechanistic switch and the outward rotation mechanism becomes the favourite one.

X=NO. The inversion of the preferred rotation (from *inward* to *outward*) is also observed when X = NO, for negative fields applied along x and z-axis (Figure 2.36 and Figure 2.37). In the absence of applied fields, the barriers for the

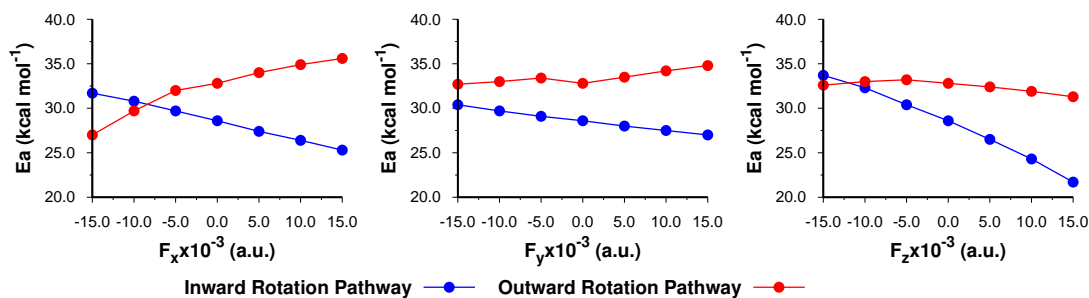


Figure 2.36: Activation energies (ΔE^\ddagger , kcal mol⁻¹) for the *conrotatory* ring opening reaction of 3-nitrosocyclobutene as a function of the applied field along the three axes ($F, 10^{-3}a.u.$). In red *outward* rotation pathway (TS_{Out}), in blue *inward* rotation pathway (TS_{In}).

	($F, 10^{-3}a.u.$)	-15.0	-10.0	-5.0	0.0	5.0	10.0	15.0
X-Axis	TS_{In}	31.7	30.8	29.7	28.6	27.4	26.4	25.3
	TS_{Out}	27.0	29.7	32.0	32.8	34.0	34.9	35.6
	Pd_{In}	-7.7	-7.3	-7.7	-8.6	-9.8	-11.1	-12.5
	Pd_{Out}	-22.3	-17.6	-13.9	-6.9	-8.5	-6.4	-4.8
Y-Axis	TS_{In}	30.4	29.7	29.1	28.6	28.0	27.5	27.0
	TS_{Out}	32.7	33.0	33.4	32.8	33.5	34.2	34.8
	Pd_{In}	-15.1	-12.8	-10.7	-8.6	-6.7	-4.9	-3.2
	Pd_{Out}	-18.0	-15.6	-13.3	-6.9	-8.6	-6.2	-3.9
Z-Axis	TS_{In}	33.7	32.3	30.4	28.6	26.5	24.3	21.7
	TS_{Out}	32.6	33.0	33.2	32.8	32.4	31.9	31.3
	Pd_{In}	-1.5	-3.7	-6.2	-8.6	-11.0	-13.6	-16.3
	Pd_{Out}	-11.8	-10.0	-8.5	-6.9	-10.4	-9.9	-9.6

Table 2.19: Activation energies (ΔE^\ddagger , kcal mol⁻¹) and reaction energies (ΔE_{React} , kcal mol⁻¹) for the *conrotatory* ring opening of 3-nitrosocyclobutene at different fields ($F, 10^{-3}a.u.$) applied along the three Cartesian axes.

inward and *outward* rotation are 28.6 and 32.8 kcal mol⁻¹ (Figure 2.34). When a negative field ($15.0 \times 10^{-3}a.u.$) is applied along x-axis, these barriers become 31.7 and 27.0 kcal mol⁻¹. Thus, the strong catalysis of the *outward* process and the less important inhibition of the *inward* process, reverse the stereochemical outcome of the reaction. A similar effect, even if less pronounced, characterizes the application of a negative field along z-axis. At $F_z = -15.0 \times 10^{-3}a.u.$ the relative magnitude of the *inward* and *outward* rotation barriers is again reversed, being 33.7 and 32.6 kcal mol⁻¹. No stereochemical inversion is observed when negative fields are applied along y direction, even if the two barriers become rather close: 30.4 and 32.7 kcal mol⁻¹.

These results are also consistent with the change of the induced dipole observed in the *inward* and *outward* transition states with respect to reactants. When $F_x = -15.0 \times 10^{-3}a.u.$, the positively oriented dipole along x-axis decreases in the TS_{In} (from 5.02 D in reactants to 4.39 D) with a consequent decrease of stabilization and increase of the activation barrier (inhibition). Once again, the opposite effect was observed for the *outward* rotation: in that case the positively oriented

X=NO							
Field Intensity	Axis	Rx	TS _{In}	TS _{Out}	Pd _{In}	Pd _{Out}	
$F = 15.0 \times 10^{-3} a.u.$	x	-1.07	-1.95	-0.65	-2.27	0.09	μ_x
	y	-4.11	-4.50	-3.66	-2.83	-2.20	μ_y
	z	-4.27	-6.44	-4.80	-6.54	-4.09	μ_z
$F = 0.0 a.u.$	x	1.82	0.93	2.86	0.97	3.65	μ_x
	y	-1.86	-2.73	-0.95	-1.15	0.09	μ_y
	z	-1.37	-2.49	-1.86	-3.09	0.05	μ_z
$F = -15.0 \times 10^{-3} a.u.$	x	5.02	4.39	7.43	5.60	9.25	μ_x
	y	0.43	-0.16	0.67	2.33	2.42	μ_x
	z	1.26	0.40	1.73	-0.26	2.90	μ_x

Table 2.20: Induced dipole ($\mu_{x,y,z}$) along the direction of the applied field ($F, 10^{-3}a.u.$) for the various critical points located for the thermal ring-opening of 3-nitrosocyclobutene.

dipole changes from 5.02 D to 7.43 D with a consequent increase of stabilization and lowering of the activation barrier (catalysis). When $F_z = -15.0 \times 10^{-3}a.u.$, the *inward* barrier increases because the positively oriented dipole decreases from 1.26 D to 0.40 D. At the same time for the *outward* process the dipole varies from 1.26 D to 1.73 D, causing a stabilization of the transition state and a catalytic effect which makes the *outward* transformation favoured.

The most important catalytic effect for X = NO was observed when a positive field is applied along the z-axis, with a decrease of the *inward* barrier from 28.6 to 21.7 kcal mol⁻¹. This is consistent with a pronounced increase of the z component of the negatively oriented dipole (from -4.27 in **Rx** to 6.43 D in TS), which strongly stabilizes the transition state.

The conformation of the nitrosyl substituent (Figure 2.37) is strongly affected by the orientation of the OEEF determining, during the course of the reaction, the variation of the molecular net dipoles previously discussed. In fact, the local NO dipole tends to orient oppositely with respect to the OEEF, controlling the favourite *inward/outward* ring-opening pathway. The stronger the local dipole, as in the case of the NO substituent, the higher is the effect on the reactive pathway, due to the presence of the OEEF.

As for X=CHO, **for X=NO, OEEFs can both catalyse and inhibit the inward rotation pathway. Moreover, negative field values along the x and z-axis lead to the mechanistic switch and the outward rotation mechanism becomes the favourite one.**

X=BH₂ (the strongest electron withdrawing group examined here) either catalysis or inhibition for both *inward* and *outward* transformations were observed (Figure 2.38). For instance, when positive fields ($F = -15.0 \times 10^{-3}a.u.$) are applied along the three axis, the *inward* barrier decreases from 13.6 to 11.8 (x), 10.7 (y) and 7.9 (z) kcal mol⁻¹ (Figure 2.38). In all three cases the dipole is nega-

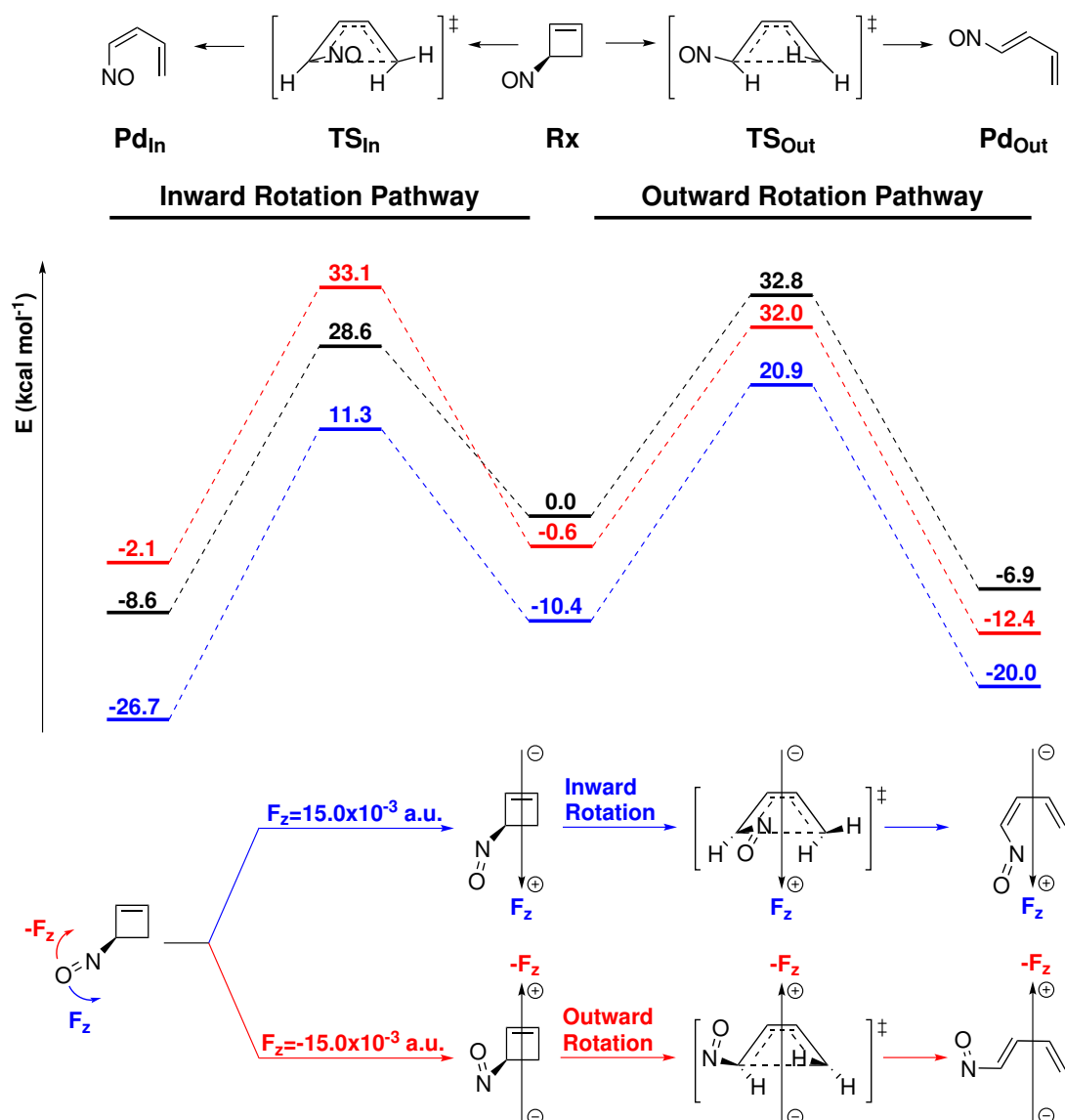


Figure 2.37: Activation energies (ΔE^\ddagger , kcal mol⁻¹) for the *conrotatory* ring opening reaction of 3-nitrosocyclobutene as a function of the applied field along the three axes ($F, 10^{-3}$ a.u.). In red *outward* rotation pathway (TS_{Out}), in blue *inward* rotation pathway (TS_{In}).

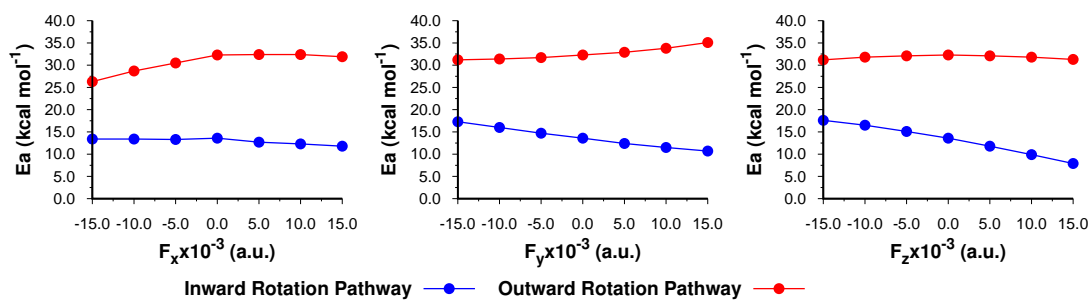


Figure 2.38: Activation energies (ΔE^\ddagger , kcal mol⁻¹) for the *conrotatory* ring opening reaction of cyclobut-2-en-1-ylborane as a function of the applied field along the three axes ($F, 10^{-3}$ a.u.). In red *outward* rotation pathway (TS_{Out}), in blue *inward* rotation pathway (TS_{In}).

	$(F, 10^{-3}a.u.)$	-15.0	-10.0	-5.0	0.0	5.0	10.0	15.0
X-Axis	TS _{In}	13.4	13.4	13.3	13.6	12.7	12.3	11.8
	TS _{Out}	26.3	28.7	30.5	32.3	32.4	32.4	31.9
	Pd _{In}	-13.5	-12.5	-12.0	-11.2	-11.8	-12.1	-12.7
	Pd _{Out}	-22.4	-18.5	-15.7	-13.1	-12.3	-11.5	-11.4
Y-Axis	TS _{In}	17.3	16.0	14.7	13.6	12.4	11.5	10.7
	TS _{Out}	31.2	31.4	31.7	32.3	32.9	33.8	35.1
	Pd _{In}	-12.0	-11.8	-11.6	-11.2	-10.8	-10.4	-9.8
	Pd _{Out}	-15.6	-14.9	-14.1	-13.1	-11.9	-10.3	-8.3
Z-Axis	TS _{In}	17.6	16.5	15.1	13.6	11.8	9.9	7.9
	TS _{Out}	31.2	31.8	32.1	32.3	32.1	31.8	31.3
	Pd _{In}	-9.3	-9.6	-10.3	-11.2	-12.5	-14.0	-15.8
	Pd _{Out}	-13.1	-13.0	-13.0	-13.1	-13.3	-13.7	-14.1

Table 2.21: Activation energies (ΔE^\ddagger , kcal mol⁻¹) and reaction energies (ΔE_{React} , kcal mol⁻¹) for the *conrotatory* ring opening of cyclobut-2-en-1-ylborane at different fields ($F, 10^{-3}a.u.$) applied along the three Cartesian axes.

X=BH ₂							
Field Intensity	Axis	Rx	TS _{In}	TS _{Out}	Pd _{In}	Pd _{Out}	
$F = 15.0 \times 10^{-3}a.u.$	x	-2.09	-2.48	-2.79	-2.63	-2.20	μ_x
	y	-3.43	-3.90	-2.31	-2.96	-1.64	μ_y
	z	-2.40	-4.09	-2.95	-3.99	-2.81	μ_z
$F = 0.0 a.u.$	x	0.52	0.13	1.11	0.42	1.72	μ_x
	y	-0.77	-1.71	-0.29	-0.47	0.14	μ_y
	z	-0.16	-1.50	-0.14	-1.05	-0.31	μ_z
$F = -15.0 \times 10^{-3}a.u.$	x	2.84	2.88	5.10	3.78	6.48	μ_x
	y	1.53	0.48	1.64	1.68	2.06	μ_x
	z	2.06	1.25	2.58	1.95	2.21	μ_x

Table 2.22: Induced dipole ($\mu_{x,y,z}$) along the direction of the applied field ($F, 10^{-3}a.u.$) for the various critical points located for the thermal ring-opening of cyclobut-2-en-1-ylborane

tively oriented and stabilizes the system. Additionally, it increases from reactants to transition state. The most important change of the dipole occurs when the field is applied along z-axis (from -2.40 to -4.09 D), in agreement with the most relevant observed catalytic effect. Importantly, in the absence of the applied field, the difference between the *inward* and *outward* barrier is much more substantial (13.6 and 32.3 kcal mol⁻¹) than in the previous cases (CHO and NO). As a consequence, the simultaneous catalysis and inhibition of the *outward* and *inward* transformation are not large enough to determine a stereochemical inversion, as observed for CHO and NO.

2.4 Conclusions

A computational investigation was carried out at the DFT (M06-2X) level of theory on the effects of OEEFs on substitution reactions. In particular, type I S_N2

reaction between methyl chloride and chloride anion and on type II Menshutkin reaction between methyl chloride and ammonia were investigated, both in absence or presence of OEEFs. In the unperturbed scenario, *Back-side* mechanism is largely preferred compared to *front-side* mechanism by 45.8 and 25.1 kcal mol⁻¹, for both type I and II S_N2, respectively.

The OEEF was applied along the z-axis in either positive or negative direction, with the orientation of the molecule kept frozen within the reference system. The induced dipole was used to roughly estimate the effects of the applied field on reactant and transition state energies, and the consequent effect on internal and global barriers. The computational results suggest that OEEF catalyses *back-side* mechanism at positive field values, while at negative field values it inverts the classical S_N2 stereochemical outcome by preferring the *front-side* and inhibiting *back-side* mechanism.

Catalysis and inhibition are rather weak for Type I S_N2 and become more important for type II S_N2. This is consistent with charge separation process which characterises type II S_N2 and allows a stronger polarization when an external field is applied. Inhibition and catalysis are consistent with the change of the induced dipole along the direction of the OEEF. In general, with positive electric fields, an increase of a negatively oriented dipole from **Rx** to **TS** determines a stabilization of **TS** and a lower barrier. Similarly, a catalytic effect occurs when a positively oriented induced dipole decreases in the same direction. Inhibition occurs when a negatively oriented dipole decreases or a positively oriented dipole increases. An opposite behaviour was observed for negative electric fields.

This effect is also governed by important geometrical rearrangements of reactant complexes in the presence of the field and, it was emphasised in the case study of the chlorine exchange reaction of 7-chloronorbornane where the reactant complex geometry significantly changes passing from the no-field case to the field-perturbed case.

The tuning of catalysis and inhibition of the *back-side* and *front-side* transformation leads to a reversed ratio between mechanisms, with the latter being favoured (stereochemical inversion from a mechanism with inversion of configuration to a mechanism with retention of configuration).

Subsequently, moving from a polar to an orbital-controlled reaction, the effects of OEEFs on activation barriers and stereochemical output of the thermal ring-opening of 3-substituted cyclobutenes C₄H₅X to butadienes was carried out. π -electron-donor substituents (X = CH₃, NH₂) and π -electron-acceptor substituents (X = CHO, NO, BH₂) were considered. In the former case the *conrotatory outward* rotation is preferred, in the latter the *conrotatory inward* process is favored, due to *torquoselectivity* principle.

The OEEF was applied along the three axes x, y and z in either positive or negative direction with the orientation of the molecule kept frozen within the reference system. Again, the induced dipole was used to roughly estimate the effects of the applied field on reactants and transition state energy and the consequent effect on activation barriers. For X = CH₃, NH₂ the OEEF does not change the preference for the *outward* rotation even if both processes (*inward* and *outward*) are either catalysed or inhibited. Catalysis and inhibition are rather weak for 3-methylcyclobutene and become more important for 3-aminocyclobutene. This is consistent with the stronger π -donor character of NH₂ and the consequent associated increase of electron density on the cyclobutene ring, which allows a stronger polarization when the external field is applied.

Also with π -acceptor substituents (X = CHO, NO, BH₂), either catalysis or inhibition were observed in the presence of an OEEF. However, with X = CHO and NO, the tuning of catalysis and inhibition of the *outward* and *inward* transformation lead to a reversed ratio between *outward* and *inward* transformation, circumventing the *torquoselectivity* principle. This was observed when negative fields were applied along y and z for X = CHO and along x and z for X = NO. Due to the π -acceptor character of these two substituents, the *outward* rotation becomes favoured. The consequence of this mechanistic switch is a reversed E-Z ratio in the stereochemical output of the reaction products. Again, catalysis, inhibition and, consequently, inversion between *outward* and *inward* processes were consistent with the change of the induced dipole from reactants to transition state in the presence of positively and negatively oriented electric fields.

For X = BH₂ (the strongest π -acceptor examined here), in the absence of the applied field, the difference between the *inward* and *outward* barrier is much more substantial (13.6 and 32.3 kcal mol⁻¹) with respect to CHO and NO. As a consequence, catalysis or inhibition of the *inward* and *outward* transformations are not large enough to determine a stereochemical inversion.

3.1 Introduction

Host-guest chemistry is emerging as a novel way to confine reactive systems (*guests*) inside containers (*hosts*) to manipulate reactivity. [70]

Reaction mechanisms of several molecules inside nanoreactors such as calixarenes, cucurbiturils, cyclodextrins, metal-organic frameworks (MOF) and zeolites, can be highly affected by confinement effects. [71] These effects act on the PES topology by modifying kinetics (catalysing and inhibiting reaction channels) but also by changing the thermodynamics of a reaction. [72] *Host*-confinement affects geometry when the volume and the shape of the host cavity are compatible with the guest system. Experimentally, structural changing as a sum of all interactions between the *host* and the *guest* is observed. [72]

Carbon NanoTubes (CNTs) are allotropic forms of carbon alongside diamond, graphite, fullerenes and graphene. CNTs are formed by sp^2 carbon atoms covalently bonded in a cylindrical structure which implies a high π -electron density localisation. This is reflected on the chemical-physical properties of CNTs which have low conductivity, an high mechanical and thermal resistance. Moreover, CNTs are characterised by great chemical inertia. The cylindrical shape allows CNTs to easily embed molecules [73–81]. The low reactivity and high stability of CNTs makes possible to carry out reactions inside these structures [75] under harsh reaction conditions differently from other nanoreactors.

The diameter is one of the parameters which can be used to distinguish guest molecules. CNTs can be viewed as a rolled graphene sheet; depending on the way they are rolled, different CNTs can be obtained. To describe the rolling pro-

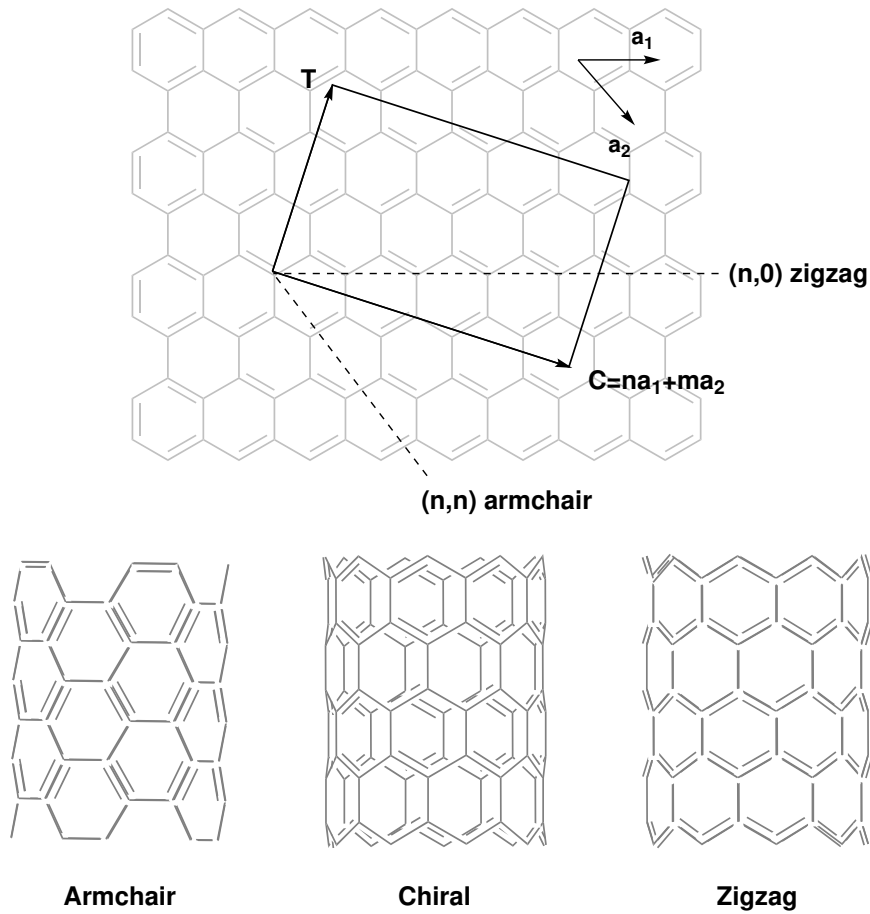


Figure 3.1: Elicity vector C (top) different CNT types (bottom)

cess, a helicity vector is defined. If a_1 and a_2 are basis vectors which define the graphene crystal reticule, the helicity vector is defined as $C = na_1 + ma_2$. Each CNT is described by an index (n,m) which represents C and hence, it is possible to define:

- an armchair CNT if $n = m$;
- a zigzag CNT if $m = 0$;
- a chiral CNT if $n \neq m$.

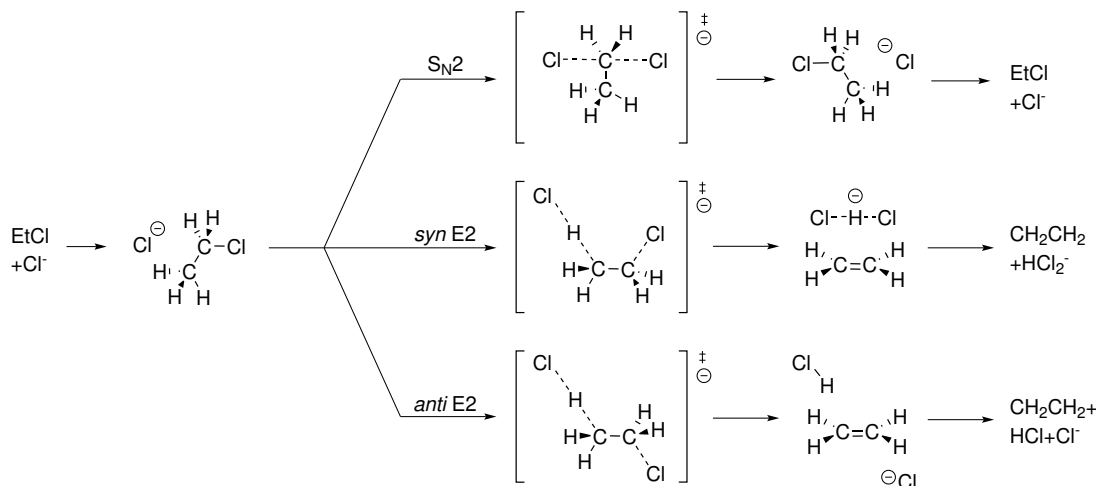
Figure 3.1 shows the helicity vector and different types of CNT. Coefficients n and m are connected with the CNT diameter, and hence, with the CNT circumference. CNT diameter can be written as in Eq. 3.1.

$$D = \left(\frac{a_C - c\sqrt{3}}{\pi} \right) \sqrt{n^2 + nm + m^2} \quad (3.1)$$

Table 3.1 resumes the diameter and circumference values, depending on n and m for armchair CNTs. Previous theoretical studies have explored the effects of confinement inside CNTs on hydrogen bond ability, [82] isomerisation reactions, [83–86] proton transfer, [86,87] decomposition reactions, [84,85,88–91] and

Index	(6,6)	(7,7)	(8,8)	(9,9)	(10,10)	(11,11)	(12,12)
Diameter (Å)	8.30	9.68	11.06	12.44	13.83	15.21	16.59
Circumference (Å)	26.05	30.39	34.73	39.07	43.42	47.76	52.10

Table 3.1: Diameter and circumference (Å) of armchair CNTs from (6,6) to (12,12)

Figure 3.2: S_N2 , *syn* E2 and *anti* E2 mechanisms.

several other reactions. [92–97] Our research group has already studied the reaction between methyl chloride and chloride anion, inside the confined environment of armchair CNTs of different sizes. That study aimed to understand the role of the carbon nanotube and the effect of the confinement on the reactants. [98] Subsequently, Khlobystov and co-workers showed experimentally, for the first time, the possibility of using CNTs as effective nanoreactors for preparative chemical reactions. [70] They found that the spatial confinement of reactant molecules inside the nanotube drastically affects both the regioselectivity and kinetics of aromatic halogenation reactions. [70] Again, our research group investigated the experimental results obtained by Khlobystov and co-workers to model the aromatic bromination of phenylacetaldehyde inside an (8,8) CNT. [99]

In the present research, the investigated reactive system is the ethyl chloride molecule reacting with the chloride anion inside armchair CNTs as *host* system. Interestingly, ethyl chloride can undergo an elimination mechanism other than substitution mechanism (the only mechanism methyl chloride can undergo). In this way, it is possible to investigate how competitive S_N2 and E2 mechanisms can be affected by the CNT environment. Two possible E2 mechanisms *via* two stereochemical pathways exist. These different stereochemical pathways depend on the *syn* (*syn*-E2) and *anti* (*anti*-E2) periplanarity of the exiting chloride anion and the β -proton abstraction. Figure 3.2 depicts these mechanisms.

A computational investigation of these confined reactions inside CNTs can help to understand which factors affect the reactivity of *guest* systems. However, due

to the dimensions of the *host*, it is unfeasible to treat the *host* fully quantum mechanically, since QM methods would require a tremendous computational cost. Hybrid QM/MM methods allow to study these *host-guest* systems by partitioning the system with different levels of theory. Under the assumption of a non reactive *host* as container, its description is based on MM level, while the *guest*, that is the reactive system, is described at the QM level.

3.2 Computational Methods

All the reported reaction profiles were calculated in gas phase at the DFT level with M06-2X functional. [20] The functional was chosen on the basis of previous benchmark studies. [100,101] Three different basis sets 6-311++G*, 6-311++G**, 6-311++G(2df,2p) [102] were tested to check which one better reproduce the highest level of theory results reported in literature [100] (Coupled Cluster CCSD and CCSD(T) methods), at infinite basis sets extrapolation, with contributions of inner-shell correlation, scalar relativistic effects, and first-order spin-orbit coupling (CCSD(T)/CBS). This level of theory is considered the highest level of theory available.

For each mechanism (S_N2 , *syn* and *anti*-E2), reaction profiles (based on the mechanistic study of Bento and co-workers [100]) were computed. Table 3.2 shows the benchmark results.

The best agreement with the CCSD(T)/CBS values obtained by Bento *et*

	Basis Set	S_N2		<i>syn</i> E2			<i>anti</i> E2		
		Rx	TS	TS	Pd	Prod.	TS	Pd	Prod.
M06-2X	6-311+G**	-12.9	4.4	27.7	-5.7	-1.5	17.9	12.6	24.4
	6-311++G**	-13.1	4.3	27.7	-5.8	-1.5	17.8	12.6	24.5
	6-311++G(2df,2p)	-12.8	4.8	27.8	-5.9	-1.8	17.9	12.3	23.8
CCSD(T)	CBS	-11.7	5.8	30.9	-4.8	-1.4	18.2	9.8	22.2

Table 3.2: Critical points energy (kcal mol⁻¹) for the S_N2 and E2 (*syn* and *anti*) mechanisms. Energies are calculated with M06-2X functional with different basis set (6-311+G**, 6-311++G** and 6-311++G(2df,2p)) with the reference CCSD(T)/CBS value obtained by Bento *et al.* [100].

al. [100] is with the level of theory M06-2X/6-311++G(2df,2p), in agreement with the results obtained by Truhlar and co-workers. [101]

Nanotubes were built using the Nanotube Builder plugin, as implemented in VMD. [103] All reported computations were carried out with the Gaussian09 [13] software. ONIOM calculations [104] were performed considering mechanical and electrostatic embedding. [105] The high-level layer (the reactive guest system ethyl chloride and chloride anion) was described at the M06-2X/6-311++G(2df,2p)

level of theory. The low-level layer (the host CNT) was described using Universal Force Field (UFF [106]) methods. In the MM calculations partial atomic (point) charges were used to compute the electrostatic interactions. These charges were calculated using the QEq formalism. [107] The structure of the various critical points (minima and saddle points) was fully optimized. Frequency calculations were carried out at the same level of theory to check the nature of critical points.

3.3 Results and Discussion

3.3.1 Gas Phase Reaction Profiles

In Figure 3.3 are reported the gas-phase reaction profiles calculated at the M06-2X/6-311++G(2df,2p) level of theory. Considering the reaction outside the CNT, the reactant complex (**Rx**) corresponds to the chloride anion position aligned with the dipole moment of the ethyl chloride molecule. From this minimum the system can follow three main paths, for which the reaction profiles were calculated. S_N2 reaction pathway: this mechanism is the favourite one with the lowest transition state (**TS_{S_N2}**) energy. The internal barrier (ΔE_{Int}^\ddagger) is 17.0 kcal mol⁻¹ and the global barrier (ΔE_{Glob}^\ddagger) is 4.8 kcal mol⁻¹. S_N2 mechanism leads to a product complex that corresponds to **Rx**, being the nucleophile and the leaving group the same specie (Cl⁻). Alternatively, the system can undergo an *anti*-E2 mechanism passing through **TS_{antiE2}**. The internal barrier (ΔE_{Int}^\ddagger) is 17.9 kcal mol⁻¹ and the global barrier (ΔE_{Glob}^\ddagger) is 30.7 kcal mol⁻¹. *Syn*-E2 mechanism results slower than *anti*-E2 mechanism, $\Delta E_{Int}^\ddagger = 40.6$ kcal mol⁻¹ and $\Delta E_{Glob}^\ddagger = 27.8$ kcal mol⁻¹. *Syn*-E2 leads to a stable product complex (**Pd_{synE2}**, -5.9 kcal mol⁻¹) thanks to the formation of an adduct between the formed alkene and HCl₂⁻ specie while **Pd_{antiE2}** lays 12.3 kcal mol⁻¹ over the asymptotic limit. Substitution mechanism is the faster process and its products are the most stable (**Pd_{S_N2}=Rx**, -12.8 kcal mol⁻¹). Finally, isolated *syn*-E2 products lay -1.8 kcal mol⁻¹ lower the asymptotic limit while *anti*-E2 products lay 23.8 kcal mol⁻¹ over the asymptotic limit.

3.3.2 Carbon Nanotube Confined Reaction Profiles

The description of the CNT confined reaction, with a QM/MM approach, requires some initial assumptions. Since the asymptotic limit of isolated reactant and products are always affected by entropic contributions, the diffusive process of the guest inside the CNT should be considered. Because of the nature of the QM/MM computations, the mechanistic model here presented considers reactants

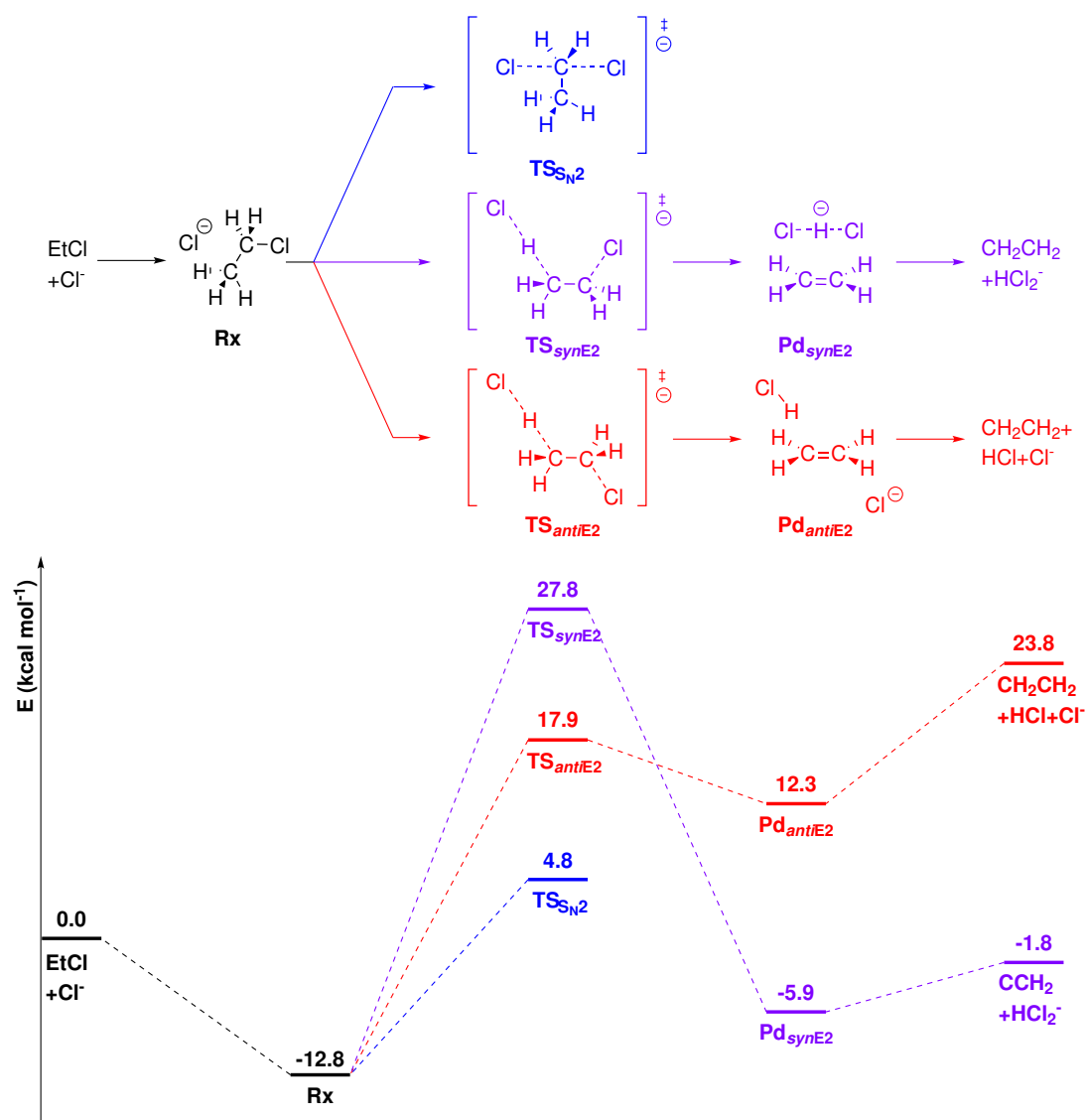


Figure 3.3: S_N2, *syn* E2 and *anti*-E2 mechanisms (on top). Reaction profiles (kcal mol⁻¹) computed at the M06-2X level for the gas-phase reaction mechanisms (on bottom).

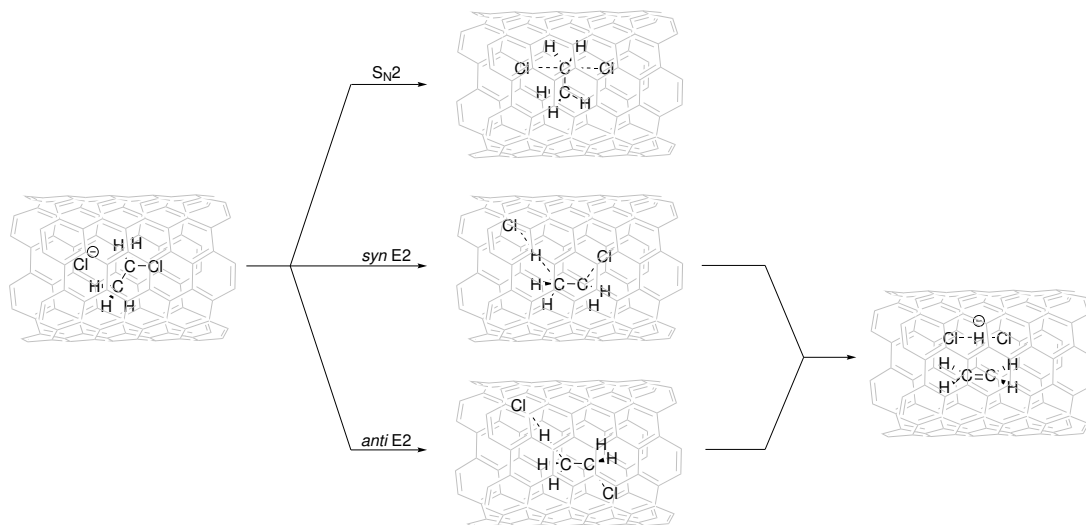


Figure 3.4: S_N2 , *syn* E2 and *anti* E2 model mechanisms inside a CNT.

already inside the CNT and, does not evaluate the extrusion of the products. Internal barriers (ΔE_{Int}^\ddagger) are not affected by this approximation and will be the only barrier considered. Figure 3.4 depicts the critical points investigated inside the CNT cavity.

It is conceivable that the relative importance of the interactions between the CNT and the reactive system in **Rx**, **TSs** and **Pd** can be significantly affected by a change in the CNT radius. These interactions could lead to catalysis/inhibition of different mechanisms. To elucidate the actual effect of the CNT size on S_N2 , *syn* and *anti*-E2 mechanisms, various CNTs of different diameter were examined: (6,6), (7,7), (8,8), (9,9), (10,10), (12,12) CNTs and, as a limit case, a graphene sheet.

Again, considering the results of previous works on S_N2 reactions, the CNT length was kept fixed at 24 Å, since it was previously reported that CNT lengths greater than 24.4 Å does not significantly affect the activation barrier (the barrier reached an asymptotic value) [98, 108]

3.3.3 Substitution Mechanism

Reactant complex (**Rx**) and S_N2 transition state (**TS_{S_N2}**) were fully re-optimised inside the range of CNT diameters considered. In Figure 3.5 calculated activation energies (ΔE^\ddagger) are reported. It is evident that **CNTs can both catalyse and inhibit S_N2 mechanism, depending on the CNT diameter**. The highest inhibition is calculated when the reaction takes place inside (12,12) CNT, the activation energy (ΔE^\ddagger) is 29.2 kcal mol⁻¹, 11.6 kcal mol⁻¹ higher than the gas phase reaction. On the other hand, (7,7), (8,8) and (9,9) CNTs show catalytic

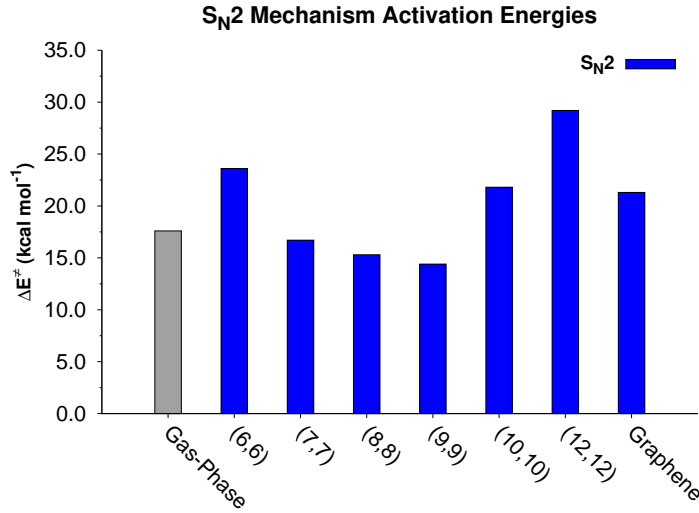


Figure 3.5: S_N2 mechanism activation energies (ΔE^\ddagger , kcal mol⁻¹) versus CNT diameter. In grey the unperturbed gas-phase activation energy.

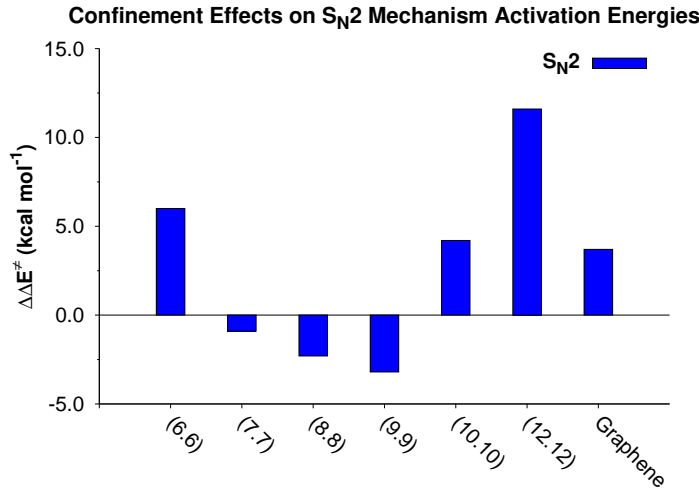


Figure 3.6: Activation energy difference ($\Delta\Delta E^\ddagger$) between the confined reaction ($\Delta E^\ddagger(CNT)$) and the unperturbed gas phase reaction ($\Delta E^\ddagger(Gas)$).

effect with a decrease in activation energies of 0.9, 2.3 and 3.2 kcal mol⁻¹, respectively (Figure 3.6).

The activation energy variation ($\Delta\Delta E^\ddagger$) between the confined reaction and the gas phase reaction is defined as:

$$\Delta\Delta E^\ddagger = \Delta E^\ddagger(CNT) - \Delta E^\ddagger(Gas) \quad (3.2)$$

to deeply understand which contributions govern the CNT confinement effects on $\Delta\Delta E^\ddagger$, an energy decomposition analysis was carried out. The way $\Delta\Delta E^\ddagger$ is modelled by considering the subtractive scheme implemented in the ONIOM method allows to rewrite $\Delta\Delta E^\ddagger$:

$$\Delta\Delta E^\ddagger = \Delta E_{MM}^{Real} - \Delta E_{MM}^{Model} + \Delta E_{QM}^{Model} - \Delta E^\ddagger(Gas) \quad (3.3)$$

A van der Waals contribution is defined as:

$$\Delta E^\neq(vdW) = \Delta E_{MM}^{Real} - \Delta E_{MM}^{CNT} - \Delta E_{MM}^{Model} \quad (3.4)$$

By substituting ΔE_{MM}^{Real} from Eq. 3.4 into Eq. 3.3

$$\Delta\Delta E^\neq = \Delta E(vdW) + \Delta E_{MM}^{CNT} + \Delta E_{QM}^{Model} - \Delta E^\neq(Gas) \quad (3.5)$$

The remaining terms are ΔE_{MM}^{CNT} which is the geometrical distortion of CNT due to the change of the cavity shape when the guest is confined. ΔE_{QM}^{Model} is the confinement effect on the model QM system calculated because of the electrostatic embedding scheme adopted. This term also contains the geometrical distortion contribution of the guest.

The difference between this term (ΔE_{QM}^{Model}) and ($\Delta E^\neq(Gas)$) is the sum of the geometrical distortion and electrostatic contribution.

$$\Delta E_{QM}^{Model} - \Delta E^\neq(Gas) = \Delta E(Elec) + \Delta E(Geom, guest) \quad (3.6)$$

By substituting Eq. 3.6, and assuming ΔE_{MM}^{CNT} itself as the geometrical distortion of CNT ($\Delta E(Geom, host)$), $\Delta\Delta E^\neq$ can be rewritten:

$$\Delta\Delta E^\neq = \Delta E(vdW) + \Delta E(Geom, host) + \Delta E(Elec) + \Delta E(Geom, guest) \quad (3.7)$$

within this formulation, the confinement effect on the kinetics of S_N2 mechanism is decomposed into a sum of contributions with a chemical meaning, providing a better comprehension of the confinement effect generated by the CNT cavity on the reactive system (in this case, ethyl chloride molecule and chloride anion). To obtain these energy values, after the geometry optimisation of the critical points, a single point computation of the isolated *guest* and *host* systems in the previous optimised geometry were carried out at both QM and MM levels.

This decomposition analysis allows to distinguish a distortion contribution due to geometrical rearrangements and an interaction contribution due to the interaction between the *host* and the *guest*. This approach is similar to the Activation Strain Model (ASM) proposed by van Zeist and Bickelhaupt, [109] a theoretical approach used to understand which factors govern the reactivity of a chemical system. ASM has been recently adopted by Houk and co-worker to investigate the Diels-Alder reaction between butadiene and CNT walls of different size. [110] However, differently from the ASM that aims to investigate the distortion/interaction between reactants, this analysis aims to investigate the distortion/interaction between the *host* and the *guest* systems to understand the effect of the CNT diameter upon

the activation energy. Moreover, the analysis reported in this thesis decomposes the interaction energy in terms of classical contribution as in force field in molecular mechanics as reported in Eq. 3.7.

Table 3.3 shows $\Delta\Delta E^\ddagger$ and its contributions as defined in Eq. 3.7. From the de-

	ΔE (kcal mol ⁻¹)	(6, 6)	(7, 7)	(8, 8)	(9, 9)	(10, 10)	(12, 12)	Graphene
S _N 2	$\Delta E(Geom, guest)$	-0.8	0.0	-0.8	-0.4	0.2	-1.1	-1.1
	$\Delta E(Geom, host)$	-0.2	0.0	0.0	0.1	-0.1	0.0	0.3
	$\Delta E(vdW)$	2.2	1.6	-0.1	1.1	0.8	-1.2	1.4
	$\Delta E(Elec)$	4.8	-2.4	-1.4	-4.1	3.2	13.9	3.1
	$\Delta\Delta E^\ddagger$ (kcal mol ⁻¹)	6.0	-0.9	-2.3	-3.2	4.2	11.6	3.7

Table 3.3: Energetic contributions to the overall confinement effect on the S_N2 kinetics: $\Delta\Delta E^\ddagger$, $\Delta E(Geom, guest)$, $\Delta E(Geom, host)$, $\Delta E(vdW)$ and $\Delta E(Elec)$.

composition analysis, it is possible to see how ***the electrostatic interaction is the most important contribution which governs the confinement effect on S_N2 kinetics.*** The comparison between the $\Delta\Delta E^\ddagger$ and $\Delta E(Elec)$ shows how this potentials have similar values (Table 3.3).

The geometrical distortion of the CNT structure is a negligible contribution as the geometrical distortion of the guest. Finally, van der Waals contribution plays an intermediate role in the catalysis/inhibition effects due to the confinement. In a previous study carried out by this research group, it was demonstrated how the Cl- π and CH- π interactions lead to a minor/major stabilisation of the reactant complex/transition state structures. $\Delta E(Elec)$ can be conceived as a global descriptor which contains the sum of all these interactions. [98]

Notably, the electrostatic interaction can be either advantageous ((7,7),(8,8),(9,9) CNTs) or disadvantageous ((6,6),(10,10),(12,12) CNTs). CNTs stabilise both **R_x** and **TS** compared to gas phase. Nonetheless, the rigidity of **TS** implies that the transition structure may not be able to maximise the stabilising interaction with the CNT which is a rigid structure too. This stabilisation is generally higher for **R_x** thanks to its flexibility which allows it to interact better with the CNT. However, when the CNT diameter fits with the **TS** structure size, the **TS** stabilisation is higher than the **R_x** stabilisation leading to an activation energy decreases. This complementarity between the *host* and the *guest* structures makes CNTs able to alter the substitution profile.

3.3.4 Elimination Mechanism

3.3.4.1 Kinetics

After the S_N2 mechanism analysis, confinement effects on *syn* and *anti*-E2 mechanisms were evaluated. **TS_{synE2}** and **TS_{antiE2}** structures were fully re-optimised

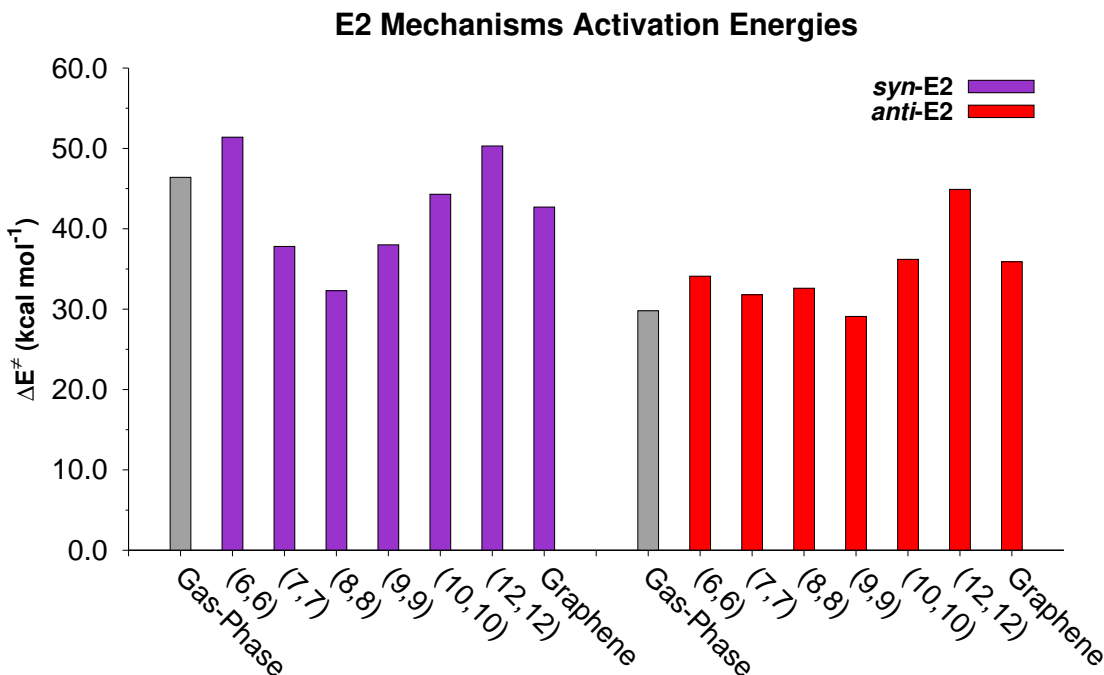


Figure 3.7: *syn* and *anti* E2 mechanisms activation energies (ΔE^\ddagger , kcal mol⁻¹) versus CNT diameter. In grey the unperturbed gas-phase activation energy for both mechanisms.

inside the range of CNT diameter considered. In Figure 3.7, the calculated activation energies (ΔE^\ddagger) are reported. Also for the elimination mechanism, Figure 3.8 shows that *CNTs can both catalyse or inhibit syn and anti-E2 mechanisms, depending on the CNT diameter*. In the case of *syn*-E2 mechanism, the highest inhibitions are calculated when the reaction takes place inside (6,6) and (12,12) CNTs. Computed activation energies are 51.4 kcal mol⁻¹ and 50.3 kcal mol⁻¹ for (6,6) and (12,12) CNTs, respectively. These CNTs increase the activation energy of 10.8 and 9.7 kcal mol⁻¹ compared to the gas phase reaction. *Anti*-E2 mechanism displayed to be less affected by confinement effects. However, also this mechanism undergoes a strong inhibition inside (12,12) CNT where the activation energy becomes 44.9 kcal mol⁻¹ (14.1 kcal mol⁻¹ higher than the gas phase activation energy $\Delta E^\ddagger(Gas) = 40.8$ kcal mol⁻¹).

As for the S_N2 mechanism, (7,7), (8,8) and (9,9) CNTs show catalytic effect on the *syn*-E2 mechanism with a decrease in the activation barrier of 2.8, 8.3 and 2.5 kcal mol⁻¹, respectively. (8,8) CNT shows the highest catalytic effect on *syn*-E2 mechanism. Finally, *anti*-E2 mechanism is slightly catalysed inside (9,9) CNT with a decrease of the gas-phase activation energy of 1.6 kcal mol⁻¹.

The plotted differences are reported in Figure 3.8. By applying the same decomposition analysis used for the S_N2 mechanism, it is possible to obtain the different contributions to the CNT confinement on *syn* and *anti*-E2 mechanisms (Table 3.4).

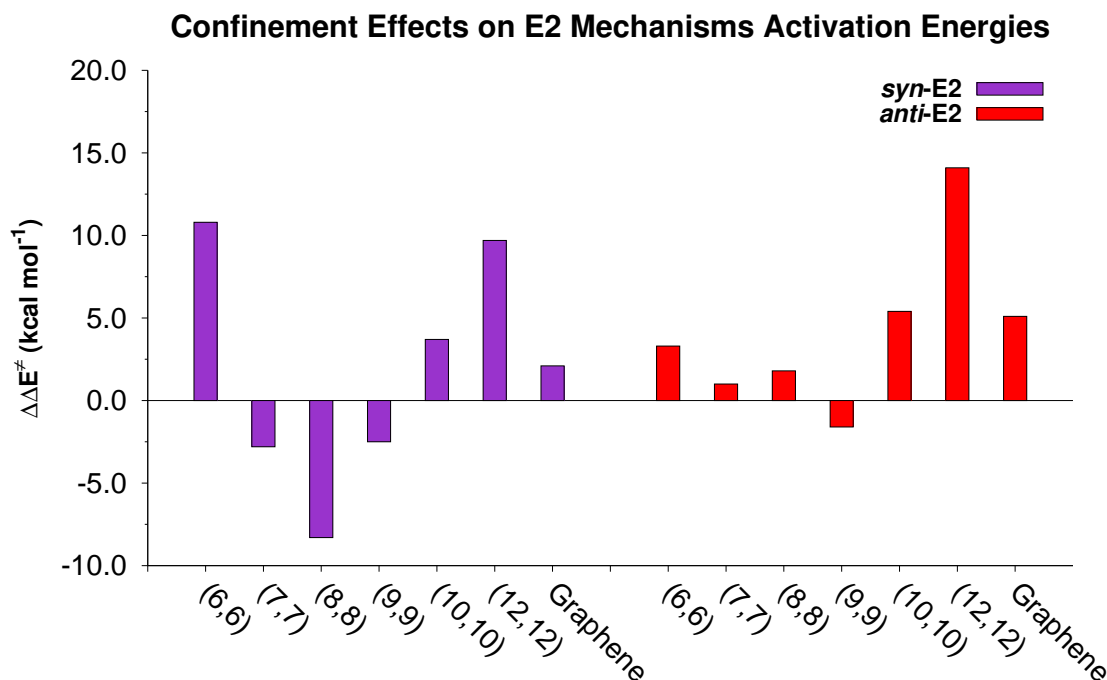


Figure 3.8: *syn* and *anti* E2 mechanisms activation energies (ΔE^\ddagger , kcal mol⁻¹) versus CNT diameter. In grey the unperturbed gas-phase activation energy for both mechanisms.

Also in the case of E2 mechanisms, activation energies variation

	ΔE (kcal mol ⁻¹)	(6,6)	(7,7)	(8,8)	(9,9)	(10,10)	(12,12)	Graphene
<i>syn</i> -E2	$\Delta E(\text{Geom, guest})$	3.9	-0.1	-0.9	0.2	1.0	-0.9	-0.7
	$\Delta E(\text{Geom, host})$	0.4	0.0	0.0	0.2	-0.1	0.0	0.9
	$\Delta E(\text{vdW})$	2.1	-0.4	-1.9	1.0	1.5	4.1	4.1
	$\Delta E(\text{Elec})$	4.4	-2.3	-5.5	-3.9	3.2	13.9	3.1
	$\Delta\Delta E^\ddagger$ (kcal mol ⁻¹)	10.8	-2.8	-8.3	-2.5	3.7	9.7	2.1
<i>anti</i> -E2	$\Delta E(\text{Geom, guest})$	-1.2	0.1	-1.0	-0.2	0.0	-0.9	-0.1
	$\Delta E(\text{Geom, host})$	-0.6	0.1	0.0	-0.1	-0.1	-0.2	-0.1
	$\Delta E(\text{vdW})$	-2.1	0.8	2.8	0.8	-0.4	2.3	2.3
	$\Delta E(\text{Elec})$	7.2	0.0	0.0	-2.1	6.0	12.9	3.0
	$\Delta\Delta E^\ddagger$ (kcal mol ⁻¹)	3.3	1.0	1.8	-1.6	5.4	14.1	5.1

Table 3.4: Energetic contributions to the overall confinement effect on the *syn* and *anti*-E2 kinetics: $\Delta\Delta E^\ddagger$, $\Delta E(\text{Geom, guest})$, $\Delta E(\text{Geom, host})$, $\Delta E(\text{vdW})$ and $\Delta E(\text{Elec})$.

is driven by the electrostatic contribution. The comparison between the $\Delta\Delta E^\ddagger$ and $\Delta E(\text{Elec})$ still shows similar values. However, in the case E2 $\Delta E(\text{vdW})$ becomes slightly higher because of the forming double bond. Again, it is possible to rationalise this trend as done for S_N2 mechanism.

3.3.4.2 Thermodynamics

The effects of the confinement were investigated on the elimination products to evaluate thermodynamical aspects of E2 mechanism. In the case of ethyl chloride

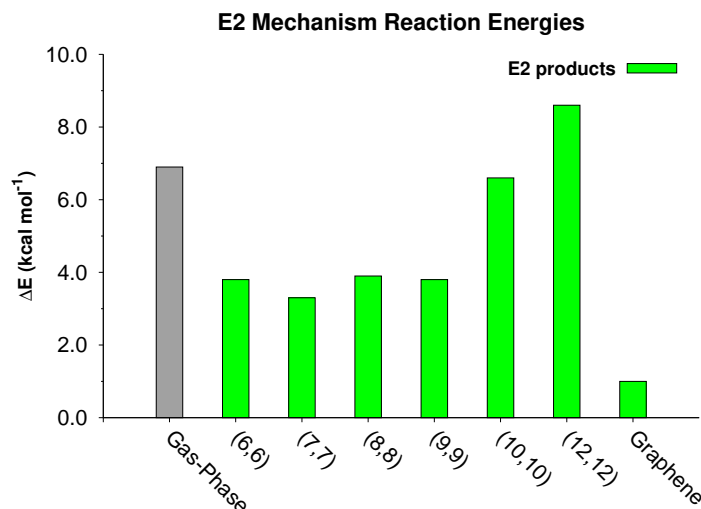


Figure 3.9: *syn*-E2 reaction energies (ΔE , kcal mol⁻¹) versus CNT diameter. In grey the unperturbed gas-phase reaction energy.

syn and *anti*-E2 mechanisms lead to the same alkene product. In Figure 3.9 the calculated reaction energies (ΔE) are reported.

Figure 3.9 shows that CNTs provides a stabilisation of the reaction products depending on the CNT size. the range of CNT radii from (6,6) to (9,9) provides a stabilisation of the products structure around 3 kcal mol⁻¹. (10,10) CNT stabilisation is absent (-0.3 kcal mol⁻¹ compared to gas-phase reaction energy) while (12,12) CNT destabilises the product structure and the reaction energy is 7.8 kcal mol⁻¹. The reaction energy (ΔE) is 6.5 kcal mol⁻¹ and 8.5 kcal mol⁻¹ for (10,10) and (12,12) CNTs, respectively. ***CNTs enhance and decrease the reaction energy of the elimination mechanism, depending on the CNT diameter.*** However, this products energy variation means also a catalysis/inhibition of the reverse reaction or electrophilic addition. ***CNTs catalyse and inhibit *syn* and *anti* electrophilic addition mechanisms, depending on the CNT diameter***

Interestingly, graphene surface provides the higher stabilisation of the elimination products, suggesting that graphene is able to provide a great thermodynamical enhancement to the elimination reaction (these aspects will be further analysed in the next section). The corresponding reaction energy is 1.5 kcal mol⁻¹, and the elimination profile is close to be iso-energetic as the S_N2 profile. However, S_N2 products (or **Rx**) are still the most stable minimum investigated. The plotted reaction energy difference is reported in Figure 3.10. By applying the decomposition analysis used for transition states, it is possible to obtain the different contributions to the confinement on the elimination reaction energy (Figure 3.5).

In this case, electrostatic contribution is no longer the dominant contribution and van der Waals term becomes more important thanks to π -stacking interac-

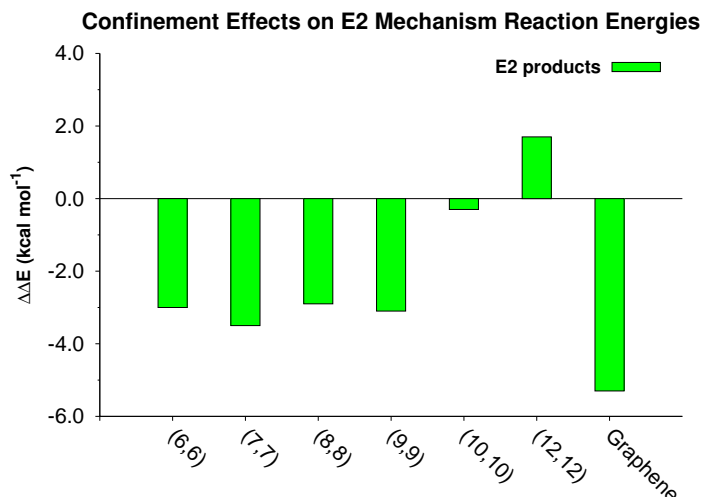


Figure 3.10: Reaction energy difference ($\Delta\Delta E$) between the confined reaction ($\Delta E(CNT)$) and the unperturbed gas phase reaction ($\Delta E(Gas)$).

	ΔE (kcal mol ⁻¹)	(6,6)	(7,7)	(8,8)	(9,9)	(10,10)	(12,12)	Graphene
E2	$\Delta E(Geom, guest)$	-1.1	1.2	2.2	0.5	0.7	-0.3	1.0
	$\Delta E(Geom, host)$	-0.6	0.0	0.0	0.1	0.0	-0.2	0.1
	$\Delta E(vdW)$	-5.3	-3.5	-1.7	-1.2	-1.8	-3.4	-3.4
	$\Delta E(Elec)$	4.0	-1.2	-3.4	-2.5	0.8	5.6	-3.0
	$\Delta\Delta E$ (kcal mol ⁻¹)	-3.0	-3.5	-2.9	-3.1	-0.3	1.7	-5.3

Table 3.5: Critical points energies of \mathbf{TS}_{S_N2} , \mathbf{TS}_{synE2} , \mathbf{TS}_{antiE2} and \mathbf{Pd} in gas phase and on a graphene sheet for R=H, CHCH₂, respectively.

tions between the ethylene molecule and the graphene π -system. However, HCl₂⁻ anion provides an important electrostatic contribution. *Elimination products formation lead to a change in the relative energy contributions importance. Van der Waals interactions, in products, become as important as electrostatic interactions.*

3.3.5 4-Chloro-1-butene

Because of the strong enhancement of the elimination mechanism thermodynamics generated by the graphene sheet, the same reaction mechanisms (S_N2 , *syn* and *anti*-E2 mechanisms) were investigated for the case of 4-chloro-1-butene reacting with chloride anion on a graphene sheet.

4-chloro-1-butene as ethyl chloride can undergo the same reaction mechanisms by reacting with chloride anion. By replacing a hydrogen atom with a vinyl group, the stereochemical aspects of these mechanisms do not change; S_N2 products are still equivalent to \mathbf{R}_x and no E-Z products can be obtained by *syn* and *anti*-E2 mechanisms. However, the elimination product \mathbf{Pd} for the reaction between 4-chloro-1-butene and chloride anion, is a butadiene molecule. Figure 3.11 depicts

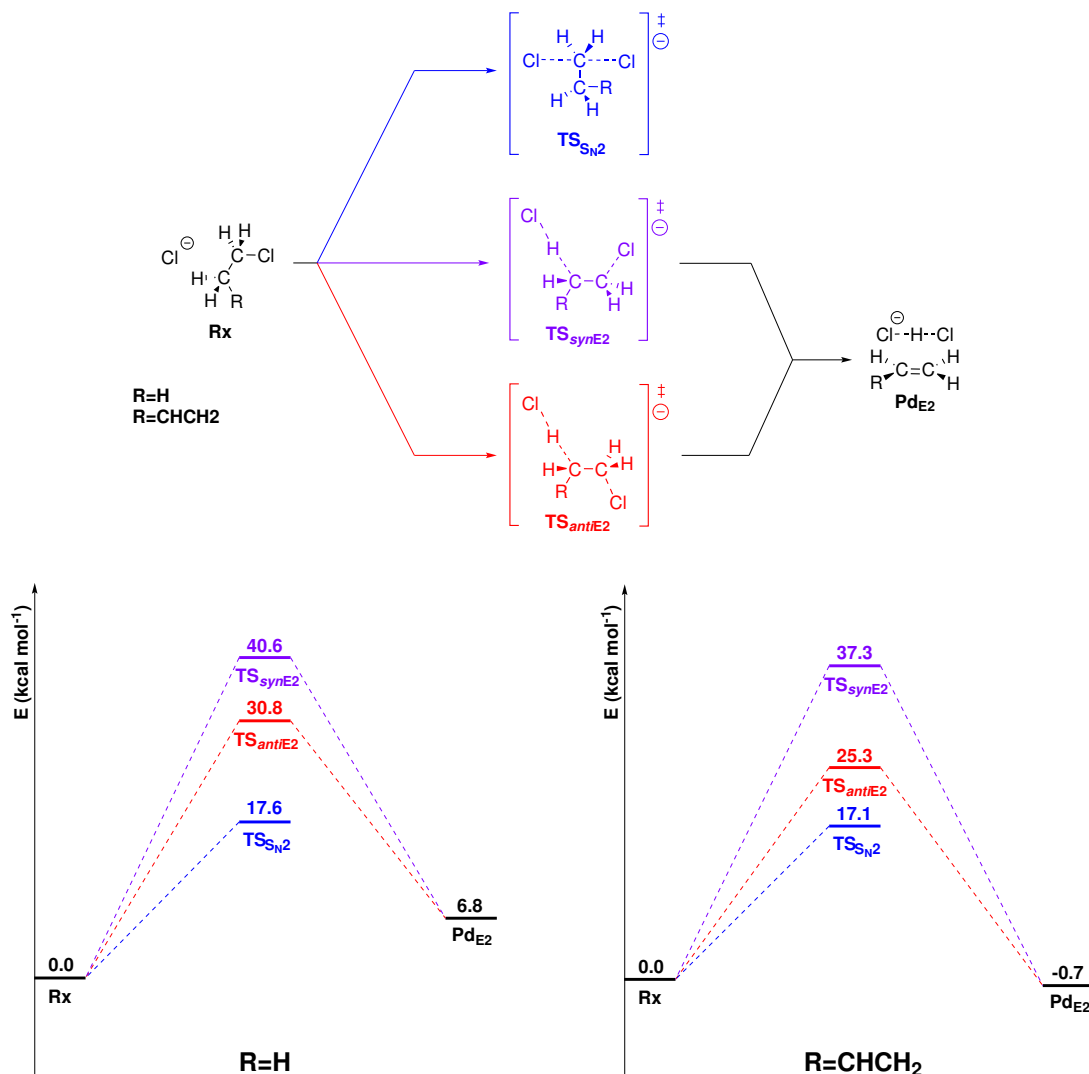


Figure 3.11: S_N2 , *syn* E2 and *anti*-E2 mechanisms for ethyl chloride/4-chloro-1-butene with chloride anion (on top). Reaction profiles (kcal mol⁻¹) computed at the M06-2X level for the gas-phase reaction mechanisms (on bottom).

these reaction profiles with a comparison with the ethyl chloride case investigated previously, both referring to **Rx** as zero energy.

Gas-phase reaction profiles (without graphene sheet) have similar activation energies for S_N2 and *syn*-E2 mechanisms while *anti*-E2 mechanism has lower activation energy when R=CHCH₂ (R=H, $\Delta E^\ddagger = 30.8$ kcal mol⁻¹ and R=CHCH₂, $\Delta E^\ddagger = 25.3$ kcal mol⁻¹). Nonetheless, the reaction energy is the quantity which more varies when R=CHCH₂ ($\Delta E = 6.8$ kcal mol⁻¹, R=H and $\Delta E^\ddagger = -0.7$ kcal mol⁻¹, R=CHCH₂). Differently from ethylene formation, butadiene formation is thermodynamically iso-energetic ($\Delta E = -0.7$ kcal mol⁻¹) thanks to the conjugation energy gained from the diene formation.

Graphene sheet displays great ability in stabilising reaction products. To explore this aspect, the reaction profiles corresponding to S_N2 , *syn* and *anti*-E2 mech-

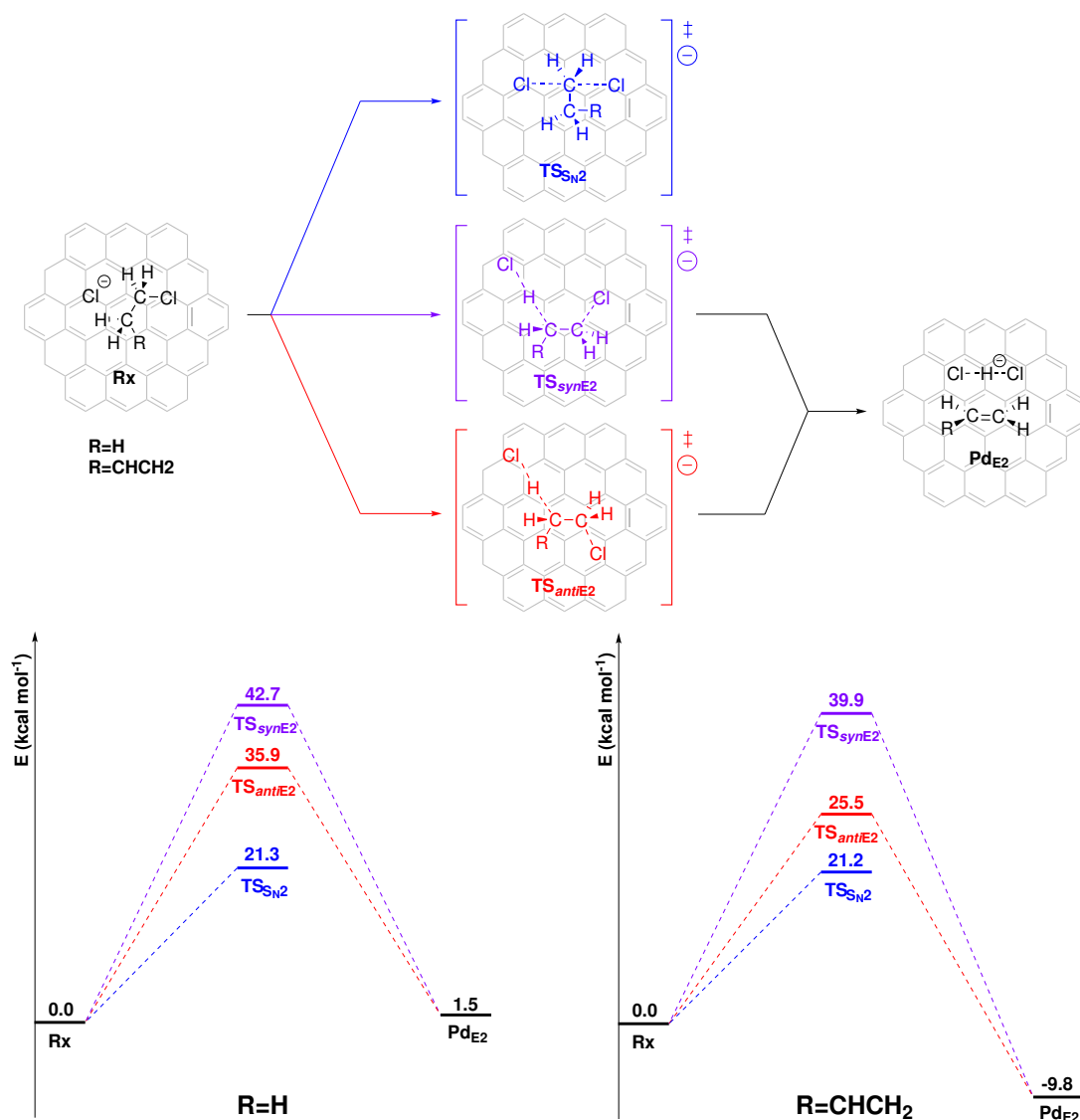


Figure 3.12: S_N2 , *syn* E2 and *anti*-E2 mechanisms for ethyl chloride/4-chloro-1-butene with chloride anion (on top). Reaction profiles (kcal mol⁻¹) computed at the M06-2X level for the graphene-hosted reaction mechanisms (on bottom).

anisms were evaluated for the case of 4-chloro-1-butene reacting with chloride anion on a graphene sheet (Figure 3.12). The reaction profile of ethyl chloride reacting with chloride anion on a graphene sheet is reported in the same Figure.

Reaction profiles displayed in Figure 3.12 show that S_N2 is still a kinetic-controlled mechanisms. In Table 3.6 the activation energies when the reaction takes place on a graphene surface compared to the gas-phase activation and reaction energies are reported.

Gas-phase profiles are affected very similarly by the presence of a graphene sheet. In particular the highest perturbation is on the reaction energy which decreases from R=H to R=CHCH₂ of -5.4 and -9.2 kcal mol⁻¹ respectively. Elimination mechanism for the reaction between 4-chloro-1-butene and chloride anion

		$\text{TS}_{\text{S}_{\text{N}}2}$	$\text{TS}_{\text{synE}2}$	$\text{TS}_{\text{antiE}2}$	Pd
R=H	Gas-Phase	17.6	40.6	32.7	6.9
	Graphene Sheet	21.3	42.7	35.9	1.5
	Graphene Effect	3.7	2.1	3.2	-5.4
R=CHCH ₂	Gas-Phase	17.1	37.3	25.3	-0.7
	Graphene Sheet	21.2	39.9	25.5	-9.8
	Graphene Effect	4.1	2.6	0.2	-9.2

Table 3.6: Critical points energies of $\text{TS}_{\text{S}_{\text{N}}2}$, $\text{TS}_{\text{synE}2}$, $\text{TS}_{\text{antiE}2}$ and Pd in gas phase and on a graphene sheet for R=H, CHCH₂, respectively.

become strongly exothermic.

Because of the diene formation on the graphene surface van der Waals interactions govern the products stabilisation. Graphene emphasises this behaviour which increases with the extension of the π -system. This is reflected in the increased stabilisation in the product formation from ethylene to butadiene.

3.4 Conclusions

A hybrid QM/MM method was used to describe the confinement effects on the $\text{S}_{\text{N}}2$, *syn* and *anti*-E2 mechanisms for ethyl chloride molecule reacting with chloride anion, inside CNTs of different diameter. $\text{S}_{\text{N}}2$ mechanism is largely preferred compared to *syn* and *anti*-E2 mechanisms both kinetically and thermodynamically.

The confinement inside CNTs of different diameter can have both catalytic or inhibiting effects depending on the CNT radius. In particular (9,9) CNT can lower the activation energy of $\text{S}_{\text{N}}2$ and *anti*-E2 mechanisms by 3.2 and 1.6 kcal mol⁻¹ compared to the gas-phase reaction; (12,12) CNT can increase the activation energy of $\text{S}_{\text{N}}2$ and *anti*-E2 mechanisms by 11.6 and 14.8 kcal mol⁻¹ respectively. *Syn*-E2 mechanism can be catalysed and inhibited more intensely with a decrease of the activation barrier of 8.3 kcal mol⁻¹ inside a (8,8) CNT and an increase of the activation energy of 10.8 kcal mol⁻¹ inside a (6,6) CNT.

After the evaluation of the kinetics of these mechanisms, the thermodynamics of the elimination reaction was investigated. CNTs can decrease the reaction energy of 3.5 kcal mol⁻¹ inside a (7,7) CNT and increase the reaction energy of 1.7 kcal mol⁻¹ inside a (12,12) CNT. However, the most intense effect in lowering the reaction energy was observed when the reaction is carried out on a graphene sheet. The reaction energy decreases of 5.3 kcal mol⁻¹ and the elim-

ination mechanism for the reaction between ethyl chloride and chloride anion becomes *quasi*-iso-energetic ($\Delta E = 1.5 \text{ kcal mol}^{-1}$) compared to the gas-phase reaction energy ($\Delta E(\text{Gas}) = 6.9 \text{ kcal mol}^{-1}$).

In the present research, a decomposition analysis of the energy variations from the reaction profile in gas-phase and inside CNTs was presented. This analysis decomposes the confinement effects in terms of vdW and electrostatic interactions and geometrical constrain on both *guest* and *host* systems. This decomposition analysis shows that geometrical rearrangement are not determinant to modify activation and reaction energies. Electrostatic contribution is the dominant contribution because it varies more than other contributions from reactant complex to transition states. Nonetheless, in the case of elimination products, van der Waals contribution becomes as important as the electrostatic interaction to describe the computed energetic trend.

To stress on the thermodynamical enhancement induced by graphene thanks to van der Waals interaction, the last part of the research has been the comparison of the reaction profiles investigated for ethyl chloride reacting with chloride anion with 4-chloro-1-butene reacting with chloride anion on a graphene sheet. Butadiene product has an increased π - π interaction with graphene surface. This comparison points out that also 4-chloro-1-butene reactions profile are kinetically affected by graphene as for ethyl chloride. However, the elimination product becomes more stable and the reaction energy decreases from the gas-phase to these calculated upon the graphene sheet by $9.2 \text{ kcal mol}^{-1}$, leading to a strongly exothermic reaction profile.

4.1 Introduction

After the discovery of catalytic RNA (ribozyme) in the 1980s, it made some sense to assume that also single-stranded DNA could have catalytic activity. This assumption was based on the fact that DNA contains almost the same functional groups as RNA. The first catalytic DNA molecule, with an RNAase Pb^{2+} -dependent activity, was isolated in 1994 by Breaker and Joyce. [111] They used the in vitro selection technique [112, 113] and demonstrated for the first time the catalytic possibility of DNA. Since then, using in vitro selection from synthetic random DNA libraries, various catalytic DNA molecules (deoxyribozymes) were identified. Nowadays, a large number of DNA-catalyzed reactions are known, [114–129] with promising potential applications in medicinal chemistry, [130, 131] nanotechnology, [132, 133] analytical chemistry, [134, 135] organic synthesis [136] and informatics. [137, 138]

Recently, the DNA catalyst 9DB1, characterized by RNA ligase activity, was crystallized in the postcatalytic state. The crystallized deoxyribozyme is a strand of 44 nucleotides that catalyzes the regioselective formation of a native phosphodiester bond between the 3'-hydroxyl and the 5'-triphosphate group of two RNA fragments. The structural characterization was achieved through single crystal X-ray crystallography, and the structural arrangement of a deoxyribozyme in its complex tertiary structure was revealed for the first time. [139] The crystallographic structure corresponds to a postcatalytic conformation where 9DB1 forms

Adapted with permission from *J. Chem. Inf. Model.* Copyright 2019, American Chemical Society

a complex with the ligated RNA product. These data show how 9DB1 uses the two binding arm motifs on the RNA substrates leaving only the two nucleotides in the ligation junction unpaired. Ribozymes with RNA ligase activity were already found in living organisms and from in vitro selection experiments. [140,141] Interestingly, the active site of RNA enzymes catalyzing the same reaction as 9DB1 is characterized by the presence of two phosphate groups that coordinate a divalent metal ion. This catalytic ion is supposed to provide electrostatic stabilization of the transition state along with other specific groups. However, no electron density suggesting the presence of a catalytic metal ion was observed in the core of 9DB1, and the possible involvement of a divalent ion is still under debate. [139] Another important structural feature evidenced by the crystallographic study is the position of nucleotide dA¹³. Because of its proximity to the ligation junction (about 3.1 Å), dA¹³ was supposed to play an important catalytic role, as suggested by mutagenesis and kinetic experiments. [139]

The commonly proposed catalytic mechanism is a general S_N2-like reaction where the 3'-hydroxyl group (nucleophile) attacks the 5'-triphosphate with the assistance of the dA¹³ phosphate group near the junction site. However, to date, the catalytic mechanism has not been understood in detail. In principle, different reaction channels are possible, particularly the following: (i) The nucleophile (3'-hydroxyl) is first activated by a proton transfer that could be accomplished by the dA¹³ phosphate. (ii) The nucleophilic attack occurs without a preliminary activation and is followed by a deprotonation by dA¹³ of the resulting acidic trivalent oxygen. (iii) The process is concerted, with the nucleophilic attack and deprotonation occurring in the same kinetic step. Since a deeper understanding of the intimate mechanism is essential to define effective tools that can help to improve catalytic efficiency, [142] we carried out a quantum-mechanical (QM) computational study at the DFT level to elucidate in detail the actual mechanism of 9DB1. Several examples are available in the literature showing that this computational methodology is successful to study enzymatic mechanisms. [143–155]

4.2 Computational Methods

MD Computations. To build a suitable model system for quantum-mechanical (QM) computations, the modelling of the system started from the crystallographic structure in the postcatalytic state (PDB: 5cck). [139] The precatalytic state was generated *in silico* by breaking the bond between the two nucleotides G⁵¹ and A⁵⁰. Then, the triphosphate group was added to generate the reactant nucleotide GTP⁵¹. A 100 ns molecular dynamics (MD) on this precatalytic state was carried out (broken G⁵¹-A⁵⁰ bond). This MD simulation was carried out in the subspace

of the full conformational space, *i.e.*, the subspace corresponding to the motion of the reactant nucleotides involved in the reaction (A^{50} and GTP^{51}). Thus, only these nucleotides were free to move while the other nucleotides were “frozen” at their crystallographic coordinates. Quenched Molecular Dynamics (QMD) protocol was used to examine the 100 ns MD trajectory. 1000 snapshots (one snapshot every 0.1 ns) were considered along the trajectory, and the corresponding structures were optimized at the MM level. The lowest energy structure (corresponding to optimized positions of the two nucleotides A^{50} and GTP^{51}) was chosen as representative of the precatalytic state and used to generate the model system for the QM computations (starting point for the subsequent QM optimization). The MD calculations were carried out with the AMBER12 [22] package in implicit water using the generalized Born (GB) solvation model. [22]

QM Computations. To reduce the size of the QM model system, all the residues within a radius of 5 Å from the center of the reacting nucleotides GTP^{51} and A^{50} were included. Also, for the residues interacting via Watson-Crick base-pairing, we removed the sugar ring and the phosphate moiety. However, the dA^{13} phosphate group was included in the model since mutagenesis studies unequivocally demonstrate its importance in the catalysis. The resulting model system included (a) the reacting nucleotides GTP^{51} and A^{50} , (b) the nucleobase portion of dA^{15} , dG^{27} , dT^{29} , and dT^{30} (for each nucleobase the removed sugar moiety was replaced by a methyl group), and (c) the dA^{13} phosphate group interacting with A^{50} . A schematic representation of the entire QM model system is given in Figure 4.1. All QM computations were carried out with the Gaussian09 software [13] using the M06-2X functional [20]. Two basis sets of different accuracy were first used to describe the system: a 6-31G* basis for the atoms involved directly in the reacting process and a 3-21G* basis for all remaining atoms (the atoms described at different levels of accuracy are indicated in Figure 4.2). This double layer approach is denoted as the M06-2X//6-31G*/3-21G* computational level. To check the accuracy of this computational approach, all critical points involved in the process (reactants **Rx**, transition states **TS1** and **TS2**, intermediate **Int**, and products **Pd**) were re-optimized using the 6-311++G** basis on the atoms participating actively in the reaction and the 6-31+G* basis for all remaining atoms (M06-2X//6-311++G**/6-31+G* computational level).

To preserve the geometry of the active site cavity and emulate the constraining effect of the RNA-ligated DNA, during the geometry optimization, the hydrogen atoms added to replace the removed atoms along the cut bonds and the atoms at the edges of the model-system at their original crystallographic positions were frozen (the “frozen” atoms are evidenced in Figure 4.2).

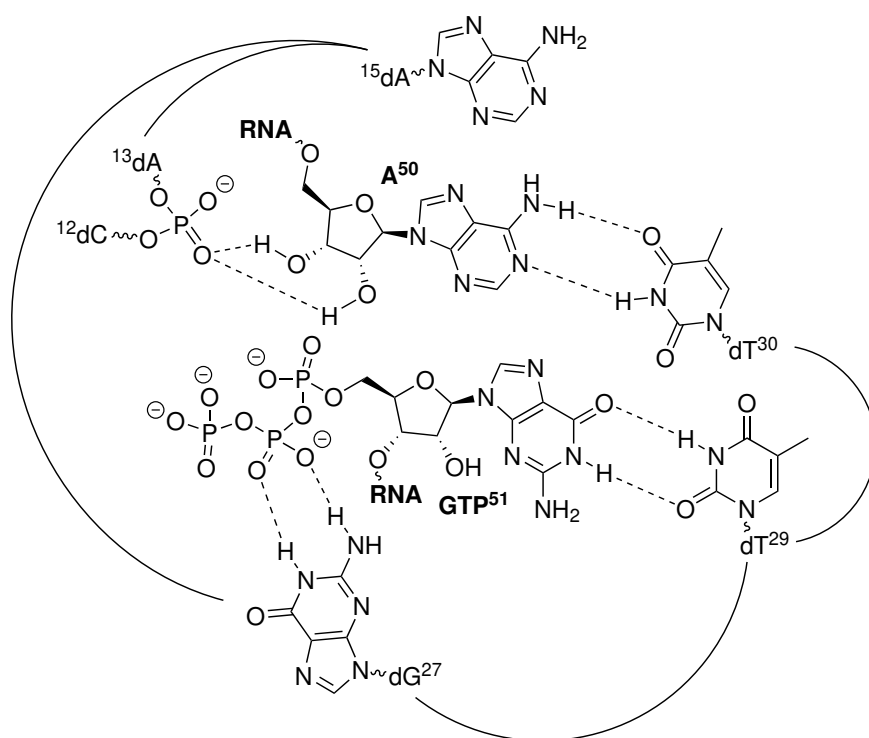


Figure 4.1: Schematic representation of the model-system used in QM computations. The continuous lines indicate the sequence of DNA nucleotides, the dotted lines indicate the hydrogen bonds between GTP^{51} and A^{50} of RNA strands and 9DB1.

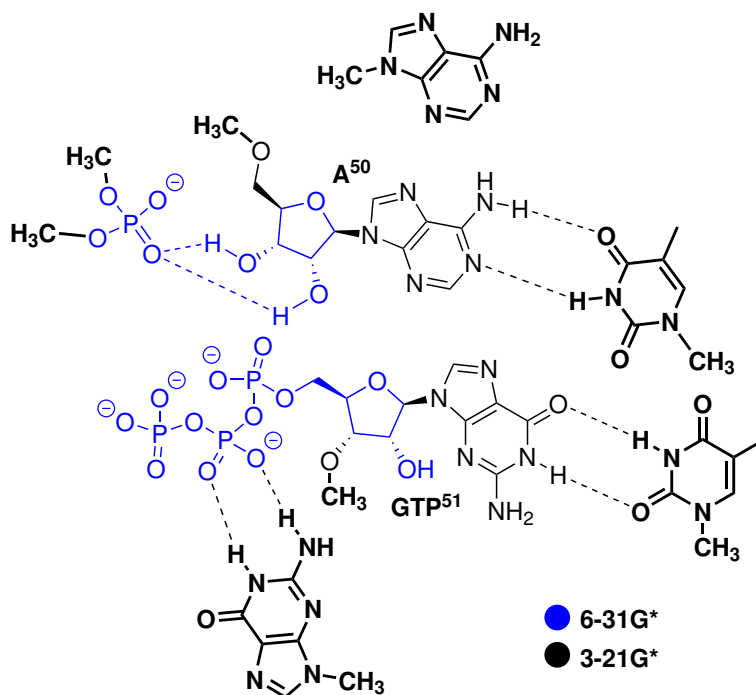


Figure 4.2: Basis sets used for the atoms included in the model-system. The marked atoms (blue) were described by the 6-31G* basis. The 3-21G* basis was used for all remaining atoms. In black bold lines the part of the system kept frozen during the calculations.

Frequency computations were carried to check the nature of the various critical points. Since the reactive system is completely exposed to water, all geometry optimizations were carried out using the IEF-PCM solvation model [21] with the water dielectric constant $\epsilon=78.36$.

4.3 Results and Discussion

4.3.1 Reaction Mechanism Investigation

The computed reaction surface is depicted in Figure 4.3. A conventional schematic representation of the reaction is given at the top of Figure 4.3.

A conventional schematic representation of the various critical points is given in Figure 4.4 (**Rx** and **TS1**) and Figure 4.6 (**Int** and **TS2**). Figures 4.4 and 4.6 also contain relevant distances to describe the reaction mechanism. The nucleobases dA¹⁵, dT³⁰, and dT²⁹ (all included in the QM computations) are deleted in the pictures since the interactions of these fragments with the reacting core are approximately constant in the course of the reaction. In **Rx**, the dA¹³ phosphate moiety forms two strong hydrogen bonds with the 2'- and 3'-hydroxyl groups: the corresponding O¹-HO² and O¹-HO³ distances are 1.78 and 1.83 Å, respectively. The distance between the 3'-hydroxyl and the α -phosphorus atom of GTP⁵¹ is still rather large, the O³-P distance being 5.82 Å. Two important hydrogen bonds involve the dG²⁷ nucleobase (nitrogen-bonded H atoms) and the second phosphate unit of the GTP⁵¹ triphosphate moiety (O⁶ and O⁷ oxygen atoms): the corresponding O⁶-HN and O⁷-HN distances are 1.72 and 1.90 Å, respectively.

A transition state **TS1** (Figure 4.4) was located for the nucleophilic attack of the 3'-hydroxyl on the α -phosphorus atom of the 5'-triphosphate group. This attack is “assisted” by a transfer of the hydroxyl proton. [156] The 3'-hydroxyl proton is “captured” by one of the negative oxygen (O⁴) bonded to the α -phosphorus atom of the GTP⁵¹ triphosphate moiety. *In TS1, the proton transfer and the nucleophilic attack occur simultaneously and are an example of “substrate-assisted mechanism”.* The O³-P distance (new forming bond) is 2.11 Å, and the proton is approximately halfway between O³ and O⁴, the H-O³ and H-O⁴ distances being 1.20 and 1.23 Å, respectively. The two hydrogen contacts involving the dG²⁷ nucleobase and the second phosphate unit of GTP⁵¹ are replaced by similar rather strong interactions with the terminal phosphate: the O⁸-HN and O⁹-HN distances are 1.75 and 1.67 Å, respectively. These interactions are important in maintaining the triphosphate moiety in the position suitable for the nucleophilic attack. Interestingly, the dA¹³ phosphate does not “assist” directly the nucleophilic attack. However, the strong hydrogen contact involving

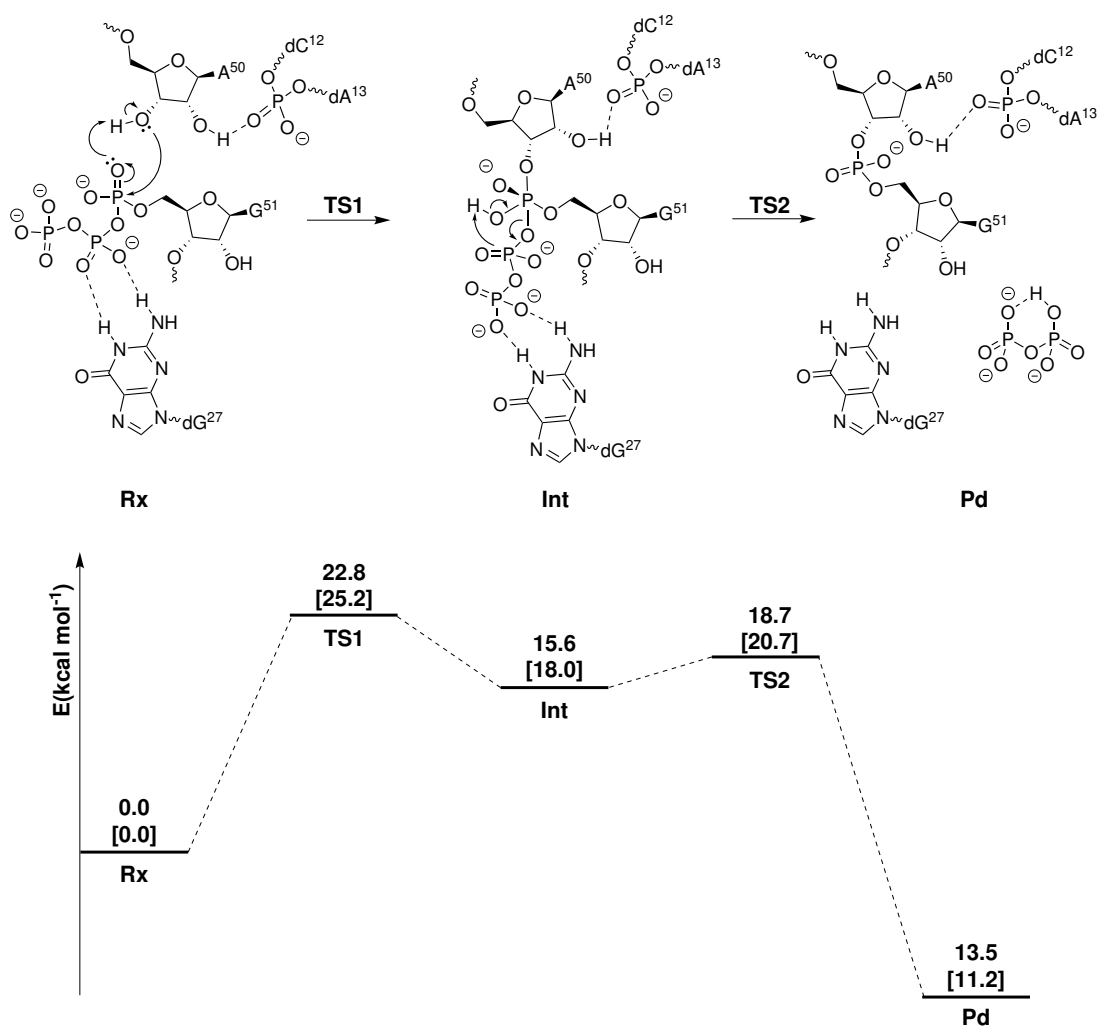


Figure 4.3: On top. A conventional representation of the reaction mechanism for the 9DB1-catalyzed reaction. On bottom. Reaction profile of the figure computed at the M06-2X//6-31G*/3-21G* computational level. In square brackets are the values obtained at the M06-2X//6-311++G**/6-31+G* level.

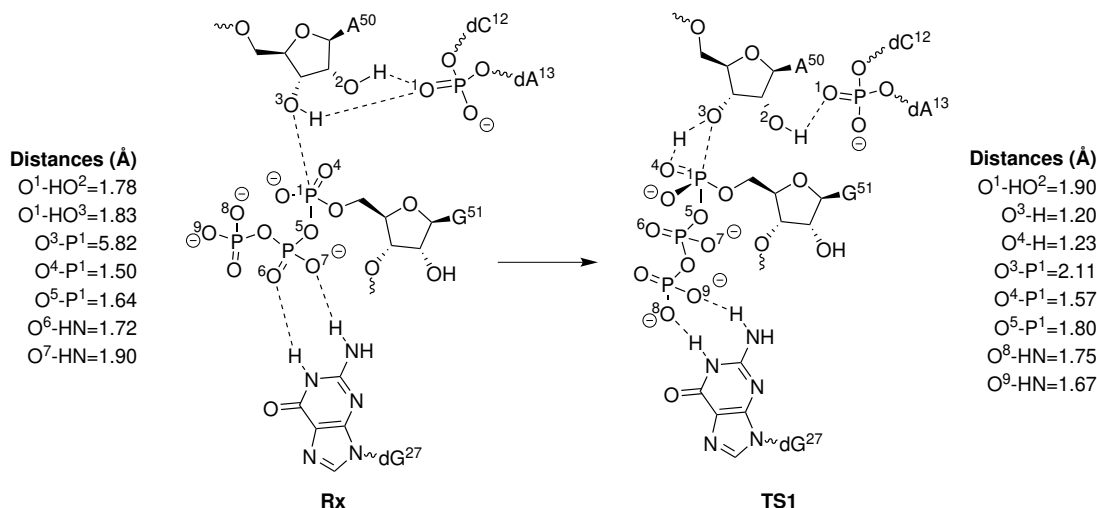


Figure 4.4: Schematic two-dimensional representation of the reactant complex **Rx** and transition state **TS1** with the related distances (Å) on margins.

the 2'-hydroxyl and the dA^{13} phosphate group is conserved during the transformation (O^1-HO^2 distance = 1.78 and 1.90 Å in **Rx** and **TS1**, respectively). *This contact can be considered as a key factor responsible for the regioselectivity of the reaction: being the 2'-hydroxyl group engaged in a strong H-bond, only the 3'-hydroxyl is available as a nucleophile to form the new bond between the two RNA nucleotides.* The computed activation energy for **TS1** (rate-determining step of the process) is 22.8 kcal mol⁻¹, a value in good agreement with the activation free energy (22.0 kcal mol⁻¹) that was obtained from the experimental kinetic constant using the Eyring's equation. [139] After inclusion of the zero-point energy corrections, the activation barrier does not change significantly, being 21.2 kcal mol⁻¹ (a complete energy profile including zero-point energy corrections is given in Figure 4.5). A reoptimization of **Rx** and **TS1** at the M06-2X//6-311++G**/6-31+G* computational level provided a barrier of 25.2 kcal mol⁻¹ (values in square brackets in Figure 4.3) in good agreement with the previous M06-2X//6-31G*/3-21G* value. This barrier becomes 23.6 kcal mol⁻¹ when zero-point energy corrections are considered (Figure 4.5). This suggests that double-layer M06-2X//6-31G*/3-21G* computations provide a reliable description of the system.

Alternative reaction channels, where the nucleophile (3'-hydroxyl) is activated by the dA^{13} phosphate or no preliminary activation occurs, were examined. To this purpose, a detailed scan of the corresponding regions of the potential surface was carried out. These reaction paths were discarded on energy ground since in all cases they lead to regions of the potential surface which are more than 40 kcal mol⁻¹ above reactants. **TS1** leads to intermediate **Int** (15.6 kcal mol⁻¹ higher than the starting complex) where the α -phosphorus atom is pentacoordinated (Figure

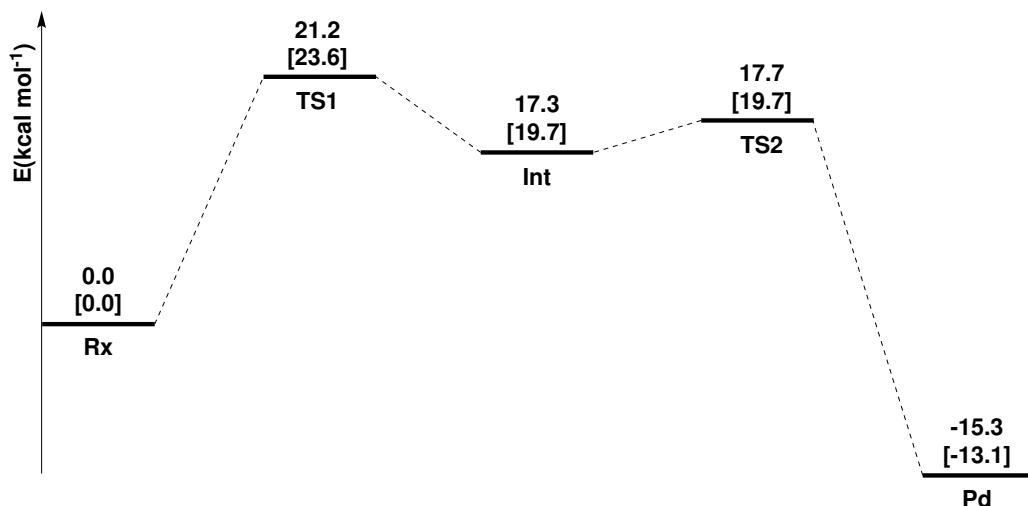


Figure 4.5: Reaction profile at the M06-2X//6-31G*/3-21G* level for the 9DB1-catalyzed reaction obtained after inclusion of the zero-point energy corrections. In square brackets the values obtained at the M06-2X//6-311++G**/6-31+G* level.

4.6).

The two strong hydrogen contacts involving the dG²⁷ nucleobase and the terminal GTP⁵¹ phosphate group do not change significantly with respect to the initial complex and the previous transition state. The hydrogen bond between the 2'-hydroxyl and the dA¹³ phosphate group also remains significant, the O¹-HO² distance being 2.63 Å. In the final step (transition state **TS2**, 18.7 kcal mol⁻¹ above **Rx**), the P-O⁵ bond breaks with the consequent dissociation of the diphosphate group. The breaking of the P¹-O⁵ bond is again “assisted” by a proton transfer from O⁴ to O⁶, *i.e.*, the oxygen belonging to the detaching diphosphate group. This mechanism agrees with the evidence recently obtained for the hydrolysis reactions of phosphate triesters that involve phosphorane intermediates. [157] The reaction is significantly exothermic, with the energy of the products **Pd** being 13.5 kcal mol⁻¹ lower than reactants.

The energy values of **Int** and **TS2** become 18.0 and 20.7 kcal mol⁻¹ after re-optimization at the more accurate M06-2X//6-311++G**/6-31+G* level. The exothermicity of the reaction changes from 13.5 to 11.2 kcal mol⁻¹. These results are a further validation of the reliability of the M06-2X//6-31G*/3-21G* approach.

The involvement of a phosphorane intermediate suggests an addition-elimination pathway (A_N+D_N), [158,159] in which the nucleophilic attack leads to a trigonal-bipyramidal pentacoordinate phosphorus that breaks down into products in a subsequent step. In the present case, the formation and breakdown of phosphorane is triggered by two “substrate assisted” proton transfers: one involving the

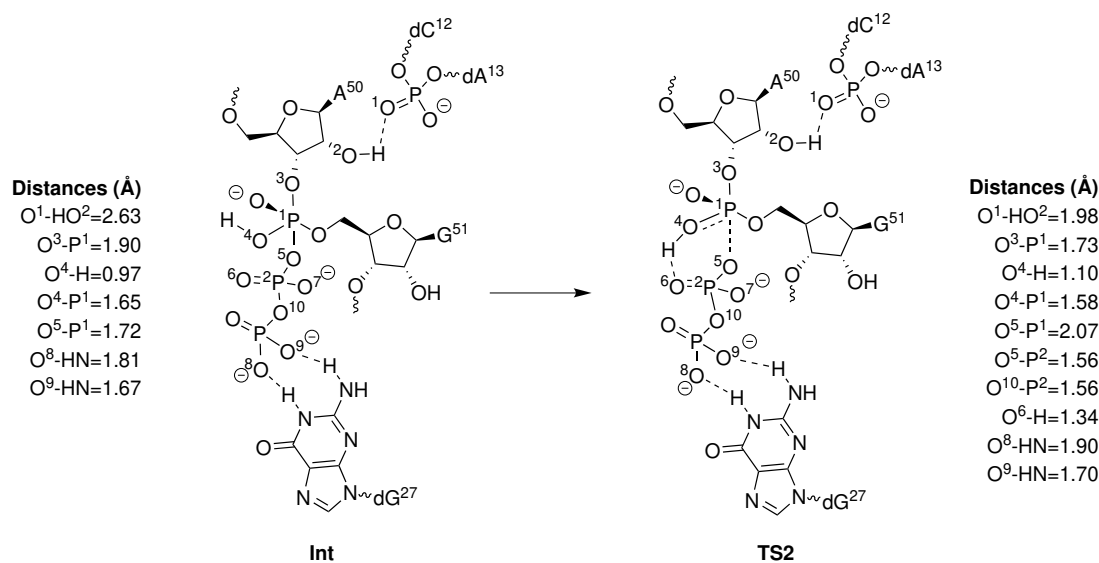


Figure 4.6: Schematic two-dimensional representation of the reactant complex **Int** and transition state **TS2** with the related distances (Å) on margins.

3'-hydroxyl and the other the hydroxyl bonded to the α -phosphorus atom. When zero-point energy corrections are included, **Int** and **TS2** become almost degenerate, with their energy relative to reactants being 17.3 and 17.7 kcal mol⁻¹, respectively (Figure 4.5). The same trend is observed at the M06-2X//6-311++G**/6-31+G* level: in that case, **Int** and **TS2** become exactly degenerate, *i.e.*, 19.7 kcal mol⁻¹. The negligible (or non existing) barrier between **Int** and **TS2** suggests that the entire process could be a concerted S_N2-like substitution with the initial attack of the nucleophile and the expulsion of the diphosphate (leaving group) occurring very asynchronously in two different phases of a unique kinetic step.

4.3.2 *In Silico* Mutagenesis

These computations clearly indicate that the H contact between the 2'-hydroxyl and the dA¹³ phosphate (O¹-HO² contact) engages the 2'-hydroxyl and favours the regioselective formation of the 3'-5' bond. At the same time, it contributes to stabilise transition state **TS1**. This finding confirms the observation of Salvatierra and co-workers on the role of the 2'-hydroxyl. These authors carried out mutagenesis experiments by substituting the 2'-OH with other groups. The same mutagenesis were carried out similar *in silico*, and the 2'-OH was replaced with F, H, and OMe. **Rx** and **TS1** were re-optimized for each mutated form, and the corresponding activation barriers were computed (Figure 4.7). In these new calculations, the M06-2X//6-31G*/3-21G* approach was used, since this com-

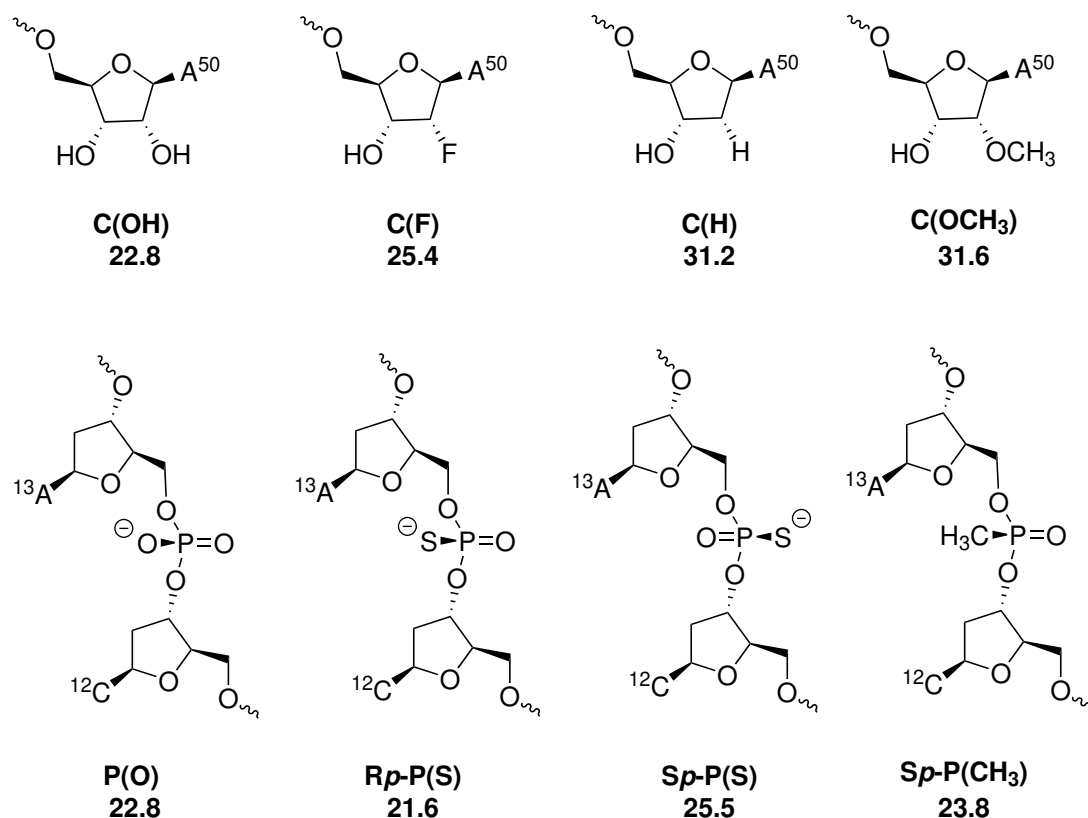


Figure 4.7: *In silico* mutagenesis operated on (first row) the 2'-hydroxyl group and (second row) dA¹³ phosphate. The corresponding computed activation barriers (kcal mol⁻¹) for TS1 are reported.

putational level was demonstrated to provide a reliable description of the entire mechanism at a lower computational cost.

The activation barrier slightly increases for F (25.4 kcal mol⁻¹) and, then, further increases for H (31.2 kcal mol⁻¹) and OMe (31.6 kcal mol⁻¹). The kinetic trend suggested by these values is OH (nonmutated) → F → H → OMe, in agreement with the experimental evidence [139] showing that the reaction becomes slower when OH is replaced by F and much slower for H and OMe. The optimized geometries for the various mutated forms show that, in the absence of the hydrogen contact, the A⁵⁰ ribose moiety moves far away from the dA¹³ phosphate. Since the new position corresponds to a more stable structural arrangement of the reactant complex, this determine an increase of the reaction barrier. To test the role of the dA¹³ phosphate, a second *in silico* mutagenesis was carried out, by replacing either of the non bridging oxygen atoms with a sulfur atom. The computed activation barriers for the two resulting stereoisomers Rp-P(S) and Sp-P(S) are 21.6 and 25.5 kcal mol⁻¹, respectively. *In silico mutagenesis barriers follow the kinetic trend evidenced by the experiment of Salvatierra.* [139] In the former case, a slight increase in the enzymatic activity was evidenced (decrease in the activation barrier of the rate-determining step TS1), while in the latter case

the process became slower (increase in the activation barrier) as experimentally observed. Interestingly, in *Rp*-P(S), the strong hydrogen bond involving the 2'-OH group and O¹ is maintained (O¹-HO² distance is 1.90 Å), and the A⁵⁰ ribose does not move significantly with respect to its original position in the nonmutated form. In *Sp*, where the sulfur atom replaces oxygen O¹, the nature of the hydrogen contact 2'-OH changes significantly. Since the new hydrogen contact involving sulfur is much weaker with respect to that of the nonmutated form (S-HO² distance becomes 2.43 Å), the A⁵⁰ ribose can move significantly from its original position leading to a more stable arrangement of the reactant complex and a consequent increase in the activation barrier.

4.4 Conclusions

This work showed that, in analogy to many ribozymes, [160, 161] a possible catalytic mechanism of 9DB1 follows a A_N+D_N reaction pattern, involving a phosphorane intermediate, where the 3'-hydroxyl group (nucleophile) of one RNA fragment attacks the 5'-triphosphate of another RNA fragment. This mechanism does not require the presence of a divalent metal cation in agreement with the experimental indications of Salvatierra [139] who did not find any evidence for electron density of a catalytic metal ion.

The process is assisted by two proton transfers occurring in different steps of the reaction: one from the 3'-hydroxyl to the oxygen bonded to the α -phosphorus atom of the triphosphate moiety of GTP⁵¹ (nucleophile activation assisted by the substrate) and the other from the α -phosphorus atom to the second phosphate group of GTP⁵¹ (leaving group activation). An accurate benchmark of the computational level demonstrated that the M06-2X//6-31G*/3-21G* approach provide a reliable description of the reaction mechanism and its energetics.

These computations point out that dA¹³ is not directly involved in the reaction. However, this nucleotide, because of its proximity to the ligation junction, plays an important catalytic role, as suggested by mutagenesis and kinetic experiments. The dA¹³ phosphate forms a strong hydrogen bond with the 2'-hydroxyl and determines the regioselectivity of the process: since the 2'-hydroxyl is engaged in a strong hydrogen contact, only the 3'-hydroxyl can behave as a nucleophile and form the new 3'-5' bond. Also, the hydrogen contact maintains the A⁵⁰ ribose in the right position to carry out the ligation process easily.

In silico mutagenesis, where the dA¹³ phosphate oxygen involved in the hydrogen contact was replaced by a sulfur atom, is accompanied by a significant rearrangement of the ribose position with an increase of the activation barrier. This leads to a lower enzymatic activity in agreement with the experimental evidence. Sim-

ilarly, the replacement of the 2'-hydroxyl with different groups (such as F, H, OMe) and the consequent disappearing of the strong hydrogen contact with the dA¹³ phosphate, causes a displacement of the A⁵⁰ ribose from its original position and a consequent increase in the activation barrier with a corresponding decrease of the enzymatic activity.

Conclusions

This thesis explores new unconventional ways to promote chemical reactivity with a computational approach. The computational approach allowed to obtain important information on the action mechanism of unusual catalytic methods which are still characterised by serious experimental limitations. The potential advantages and disadvantages of each method were carefully examined.

The first "unconventional" catalytic method examined here was the use of OEEF. This method is based on the application of an external electric field on the reacting system. The field has important effects on the molecular electronic density. Molecules are polarised along a direction which depends on the direction of the applied field. This can enhance or inhibit the natural reactivity of a system.

In particular, the effect of OEEFs on (i) substitution S_N2 reaction and (ii) electrocyclic reaction was examined.

In the first case (i), the effect of the external field on the reaction between Cl^- and CH_3Cl and the Menshutkin reaction between NH_3 and CH_3Cl was examined. The results suggest that OEEF can catalyse both substitution reaction and inhibit the natural reactivity promoting an unfavoured mechanism which leads to S_N2 with retention of configuration. Subsequently, the effect of electric fields on 7-chloronorbornane, a class of strained compounds where S_N2 reaction does not occur easily, was investigated. Electric fields can promote S_N2 mechanism in this class of unreactive compound.

In the second case (ii) the effect of OEEFs on electrocyclic reactions of 3-substituted cyclobutene molecules was studied. It was discovered that the external field affects not only the reaction rate but also the stereochemical output of the reaction. In all the investigated cases, it was possible to rationalize the effects of the external field on kinetics and stereochemistry by examining the variation of the induced dipole from reactants to transition state. The induced dipole can be

considered a global factor which simultaneously takes into account the variation of charges and the variation of orbital interactions due to the external field.

A second “unconventional” approach to catalysis examined in this thesis was the use of CNTs as nano-reactors. Reaction are confined within the nanotube that can affect both kinetics (acceleration or inhibition) and thermodynamics. The effect of the CNT strongly depends on its radius. The *host-guest* interactions affect the reaction energy profile. These interactions are mainly of electrostatic or van der Waals nature, depending on the polarity of the molecule and the complementarity between guest and CNT cavity size.

Finally, it was examined how deoxyribozyme (9DB1) can catalyse the RNA ligation reaction thanks to its ability to orient RNA strands in a conformation which allows the regioselective formation of the 3'-5' bond. Due to their structure, reactive RNA nucleotides can be positioned close to each other. This is done by means of the Watson-Crick base pairing which recognizes and properly orients reactants. After this organisation process, 9DB1 catalyses the regioselective RNA ligation reaction by generating a highly-polarised local environment provided by its nucleotides.

Bibliography

- [1] March, J. *Advanced Organic Chemistry: Reactions, Mechanisms, and Structure (3rd ed.)* **1985**.
- [2] Cerjan, C. J.; Miller, W. H. *J. Chem. Phys.* **1981**, *75*(6), 2800–2806.
- [3] Simons, J.; Joergensen, P.; Taylor, H.; Ozment, J. *J. Phys. Chem.* **1983**, *87*(15), 2745–2753.
- [4] Banerjee, A.; Adams, N.; Simons, J.; Shepard, R. *J. Phys. Chem.* **1985**, *89*(1), 52–57.
- [5] Schlegel, H. B. *J. Comp. Chem.* **1982**, *3*(2), 214–218.
- [6] Bell, S.; Crighton, J. S. *J. Chem. Phys.* **1984**, *80*(6), 2464–2475.
- [7] Peng, C.; Bernhard Schlegel, H. *Israel Journal of Chemistry* **1993**, *33*(4), 449–454.
- [8] Boys, S. F.; Egerton, A. C. *Proceedings of the Royal Society of London. Series A. Mathematical and Physical Sciences* **1950**, *200*(1063), 542–554.
- [9] Shavitt, I.; Karplus, M. *J. Chem. Phys.* **1962**, *36*(2), 550–551.
- [10] Hohenberg, P.; Kohn, W. *Phys. Rev.* **1964**, *136*, B864–B871.
- [11] Kohn, W.; Sham, L. *J. Phys. Rev.* **1965**, *140*, A1133–A1138.
- [12] Perdew, J. P.; Schmidt, K. *AIP Conf. Proc.* **2001**, *577*, 1–20.
- [13] Gaussian09 Revision E.01 Wallingford CT 2009. Frisch, M. J.; Trucks, G. W.; Schlegel, H. B.; Scuseria, G. E.; Robb, M. A.; Cheeseman, J. R.;

- Scalmani, G.; Barone, V.; Mennucci, B.; Petersson, G. A.; Nakatsuji, H.; Caricato, M.; Li, X.; Hratchian, H. P.; Izmaylov, A. F.; Bloino, J.; Zheng, G.; Sonnenberg, J. L.; Hada, M.; Ehara, M.; Toyota, K.; Fukuda, R.; Hasegawa, J.; Ishida, M.; Nakajima, T.; Honda, Y.; Kitao, O.; Nakai, H.; Vreven, T.; Montgomery, Jr., J. A.; Peralta, J. E.; Ogliaro, F.; Bearpark, M.; Heyd, J. J.; Brothers, E.; Kudin, K. N.; Staroverov, V. N.; Kobayashi, R.; Normand, J.; Raghavachari, K.; Rendell, A.; Burant, J. C.; Iyengar, S. S.; Tomasi, J.; Cossi, M.; Rega, N.; Millam, J. M.; Klene, M.; Knox, J. E.; Cross, J. B.; Bakken, V.; Adamo, C.; Jaramillo, J.; Gomperts, R.; Stratmann, R. E.; Yazyev, O.; Austin, A. J.; Cammi, R.; Pomelli, C.; Ochterski, J. W.; Martin, R. L.; Morokuma, K.; Zakrzewski, V. G.; Voth, G. A.; Salvador, P.; Dannenberg, J. J.; Dapprich, S.; Daniels, A. D.; Farkas, .; Foresman, J. B.; Ortiz, J. V.; Cioslowski, J.; Fox, D. J.
- [14] Becke, A. D. *Phys. Rev. A* **1988**, *38*, 3098–3100.
- [15] Becke, A. D. *J. Chem. Phys.* **1993**, *98*(2), 1372–1377.
- [16] Vosko, S. H.; Wilk, L.; Nusair, M. *Can. J. Chem.* **1980**, *58*(8), 1200–1211.
- [17] Lee, C.; Yang, W.; Parr, R. G. *Phys. Rev. B* **1988**, *37*, 785–789.
- [18] Becke, A. D. *J. Chem. Phys.* **1993**, *98*(7), 5648–5652.
- [19] Zhao, Y.; Truhlar, D. G. *J. Phys. Chem. A* **2006**, *110*(49), 13126–13130.
- [20] Zhao, Y.; Truhlar, D. G. *Theo. Chem. Acc.* **2008**, *120*(1), 215–241.
- [21] Tomasi, J.; Mennucci, B.; Cammi, R. *Chem. Rev.* **2005**, *105*(8), 2999–3094.
- [22] AMBER 12, University of California, San Francisco. Case, D.; Darden, T.; Cheatham, T.; Simmerling, C.; Wang, J.; Duke, R.; Luo, R.; Walker, R.; Zhang, W.; Merz, K.; Roberts, B.; Hayik, S.; Roitberg, A.; Seabra, G.; Swails, J.; Götz, A.; Kolossváry, I.; Wong, K.; Paesani, F.; Kollman, P.
- [23] Warshel, A.; Levitt, M. *Journal of Molecular Biology* **1976**, *103*(2), 227 – 249.
- [24] Maseras, F.; Morokuma, K. *J. Comp. Chem.* *16*(9), 1170–1179.
- [25] Humbel, S.; Sieber, S.; Morokuma, K. *J. Chem. Phys.* **1996**, *105*(5), 1959–1967.
- [26] Svensson, M.; Humbel, S.; Froese, R. D. J.; Matsubara, T.; Sieber, S.; Morokuma, K. *J. Phys. Chem.* **1996**, *100*(50), 19357–19363.

- [27] Dapprich, S.; Komáromi, I.; Byun, K.; Morokuma, K.; Frisch, M. *J. Am. Chem. Soc.* **1999**, *121*, 461–462, 1–21.
- [28] Petrosko, S. H.; Johnson, R.; White, H.; Mirkin, C. A. *J. Am. Chem. Soc.* **2016**, *138*(24), 7443–7445.
- [29] Larhed, M.; Moberg, C.; Hallberg, A. *Acc. Chem. Res.* **2002**, *35*(9), 717–727.
- [30] Mason, T. J. *Chem. Soc. Rev.* **1997**, *26*, 443–451.
- [31] Wang, J.; Kouznetsova, T. B.; Niu, Z.; Ong, M. T.; Klukovich, H. M.; Rheingold, A. L.; Martinez, T. J.; Craig, S. L. *Nat. Chem.* **2015**, *7*, 323–327.
- [32] Fried, S. D.; Bagchi, S.; Boxer, S. G. *Science* **2014**, *346*(6216), 1510–1514.
- [33] Warshel, A.; Sharma, P. K.; Kato, M.; Xiang, Y.; Liu, H.; Olsson, M. H. M. *Chem. Rev.* **2006**, *106*(8), 3210–3235.
- [34] Shaik, S.; de Visser, S. P.; Kumar, D. *J. Am. Chem. Soc.* **2004**, *126*(37), 11746–11749.
- [35] Lai, W.; Chen, H.; Cho, K.-B.; Shaik, S. *J. Phys. Chem. Letters* **2010**, *1*(14), 2082–2087.
- [36] Meir, R.; Chen, H.; Lai, W.; Shaik, S. *ChemPhysChem* **11**(1), 301–310.
- [37] Wang, Z.; Danovich, D.; Ramanan, R.; Shaik, S. *J. Am. Chem. Soc.* **2018**, *140*(41), 13350–13359.
- [38] Ramanan, R.; Danovich, D.; Mandal, D.; Shaik, S. *J. Am. Chem. Soc.* **2018**, *140*(12), 4354–4362.
- [39] Stuyver, T.; Danovich, D.; De Proft, F.; Shaik, S. *J. Am. Chem. Soc.* **2019**, *141*(24), 9719–9730.
- [40] Shaik, S.; Mandal, D.; Ramanan, R. *Nat. Chem.* **2016**, *8*, 1091–1098.
- [41] Aragonès, A. C.; Haworth, N. L.; Darwish, N.; Ciampi, S.; Bloomfield, N. J.; Wallace, G. G.; Diez-Perez, I.; Coote, M. L. *Nature* **2016**, *531*, 88–91.
- [42] Lakshmi, S.; Dutta, S.; Pati, S. K. *J. Phys. Chem. C* **2008**, *112*(38), 14718–14730.

- [43] Gorin, C. F.; Beh, E. S.; Kanan, M. W. *J. Am. Chem. Soc.* **2012**, *134*(1), 186–189.
- [44] Calvaresi, M.; Martinez, R. V.; Losilla, N. S.; Martinez, J.; Garcia, R.; Zerbetto, F. *J. Phys. Chem. Lett.* **2010**, *1*(22), 3256–3260.
- [45] Akamatsu, M.; Sakai, N.; Matile, S. *J. Am. Chem. Soc.* **2017**, *139*(19), 6558–6561.
- [46] Ciampi, S.; Darwish, N.; Aitken, H. M.; Díez-Pérez, I.; Coote, M. L. *Chem. Soc. Rev.* **2018**, *47*, 5146–5164.
- [47] Zhang, L.; Laborda, E.; Darwish, N.; Noble, B. B.; Tyrell, J. H.; Pluczyk, S.; Le Brun, A. P.; Wallace, G. G.; Gonzalez, J.; Coote, M. L.; Ciampi, S. *J. Am. Chem. Soc.* **2018**, *140*(2), 766–774.
- [48] Rai, D.; Joshi, H.; Kulkarni, A. D.; Gejji, S. P.; Pathak, R. K. *J. Phys. Chem. A* **2007**, *111*(37), 9111–9121.
- [49] Foster, J. P.; Weinhold, F. *J. Am. Chem. Soc.* **1980**, *102*(24), 7211–7218.
- [50] Reed, A. E.; Weinstock, R. B.; Weinhold, F. *J. Chem. Phys.* **1985**, *83*(2), 735–746.
- [51] Wang, C.; Danovich, D.; Chen, H.; Shaik, S. *J. Am. Chem. Soc.* **2019**, *141*(17), 7122–7136.
- [52] Lumb, J. T.; Whitham, G. H. *Chem. Comm.* **1966**, page 400.
- [53] Nash, J.; Waugh, T.; Morrison, H. *Tetrahedron Letters* **1998**, *39*(36), 6449 – 6452.
- [54] Menshutkin, N. *Z. Phys. Chem.* **1895**, *17*(193).
- [55] J.L.M. Abboud, R. Notario, J. B. M. *Progress in Physical Chemistry John Wiley & Sons Inc; Hoboken. NJ, USA* **1993**, *19*(1-182).
- [56] Pedley, J. *Thermochemical data and structures of organic compounds* **1993**, *18*(College Station, TX, USA).
- [57] Gao, J.; Xia, X. *J. Am. Chem. Soc.* **1993**, *115*(21), 9667–9675.
- [58] Maran, U.; Karelson, M.; Pakkanen, T. A. *Journal of Molecular Structure: THEOCHEM* **1997**, *397*(1), 263 – 272.
- [59] Amovilli, C.; Mennucci, B.; Floris, F. M. *J. Phys. Chem. B* **1998**, *102*(16), 3023–3028.

- [60] Castejon, H.; Wiberg, K. B. *J. Am. Chem. Soc.* **1999**, *121*(10), 2139–2146.
- [61] Ramanan, R.; Danovich, D.; Mandal, D.; Shaik, S. *J. Am. Chem. Soc.* **2018**, *140*(12), 4354–4362.
- [62] Woodward, R. B.; Hoffmann, R. *J. Am. Chem. Soc.* **1965**, *87*(2), 395–397.
- [63] Kirmse, W.; Rondan, N. G.; Houk, K. N. *J. Am. Chem. Soc.* **1984**, *106*(25), 7989–7991.
- [64] Rondan, N. G.; Houk, K. N. *J. Am. Chem. Soc.* **1985**, *107*(7), 2099–2111.
- [65] Rudolf, K.; Spellmeyer, D. C.; Houk, K. N. *J. Org. Chem.* **1987**, *52*(16), 3708–3710.
- [66] Dolbier, W. R.; Koroniak, H.; Houk, K. N.; Sheu, C. *Acc. Chem. Res.* **1996**, *29*(10), 471–477.
- [67] Niwayama, S.; Kallel, E. A.; Spellmeyer, D. C.; Sheu, C.; Houk, K. N. *J. Org. Chem.* **1996**, *61*(8), 2813–2825.
- [68] Vaissier, V.; Sharma, S. C.; Schaettle, K.; Zhang, T.; Head-Gordon, T. *ACS Catalysis* **2018**, *8*(1), 219–227.
- [69] Prah, A.; Frančišković, E.; Mavri, J.; Stare, J. *ACS Catalysis* **2019**, *9*(2), 1231–1240.
- [70] Miners, S. A.; Rance, G. A.; Khlobystov, A. N. *Chem. Commun.* **2013**, *49*, 5586.
- [71] Santiso, E. E.; George, A. M.; Turner, C. H.; Kostov, M. K.; Gubbins, K. E.; Buongiorno-Nardelli, M.; Sliwinska-Bartkowiak, M. *Appl. Surf. Sci.* **2005**, *252*, 766.
- [72] Pederson, M. R.; Broughton, J. Q. *Phys. Rev. Lett.* **1992**, *69*, 2689.
- [73] Khlobystov, A. N.; Britz, D. A.; Briggs, G. A. D. *Acc. Chem. Res.* **2005**, *38*, 901.
- [74] Khlobystov, A. N. *ACS Nano* **2011**, *5*, 9306.
- [75] Britz, D. A.; Khlobystov, A. N. *Chem. Soc. Rev.* **2006**, *35*, 637.
- [76] Troche, K. S.; Coluci, V. R.; Braga, S. F.; Chinellato, D. D.; Sato, F.; Legoas, S. B.; Rurali, R.; Galvao, D. S. *Nano Lett.* **2005**, *5*, 349.
- [77] Guan, L.; Suenaga, K.; Shi, Z.; Gu, Z.; Iijima, S. *Nano Lett.* **2007**, *7*, 1532.

- [78] Takenobu, T.; Takano, T.; Shiraishi, M.; Murakami, Y.; Ata, M.; Kataura, H.; Achiba, Y.; Iwasa, Y. *Nat. Mater.* **2003**, *2*, 683.
- [79] Plank, W.; Pfeiffer, R.; Schaman, C.; Kuzmany, H.; Calvaresi, M.; Zerbetto, F.; Meyer, J. *ACS Nano* **2010**, *4*, 4515.
- [80] Liu, X.; Kuzmany, H.; Ayala, P.; Calvaresi, M.; Zerbetto, F.; Pichler, T. *Adv. Funct. Mater.* **2012**, *22*, 3202.
- [81] Wang, W.; Wang, D.; Zhang, Y.; Ji, B.; Tian, A. *J. Chem. Phys.* **2011**, *134*, 054317.
- [82] Santiso, E. E.; Buongiorno Nardelli, M.; Gubbins, K. E. *J. Chem. Phys.* **2008**, *128*, 034704.
- [83] Feng, H.; Qian, Z.; Wang, C.; Chen, C.; Chen, J. *Dalton Trans.* **2011**, *40*, 4183.
- [84] Wang, L.; Yi, C.; Zou, H.; Gan, H.; Xu, J.; Xu, W. *J. Mol. Model.* **2011**, *17*, 2751.
- [85] Wang, L.; Yi, C.; Zou, H.; Xu, J.; Xu, W. *Mater. Chem. Phys.* **2011**, *127*, 232.
- [86] Mann, D. J.; Halls, M. D. *Phys. Rev. Lett.* **2003**, *90*, 195503.
- [87] Zoete, V.; Meuwly, M. *J. Chem. Phys.* **2004**, *120*, 7085.
- [88] Santiso, E. E.; George, A. M.; Gubbins, K. E.; Buongiorno Nardelli, M. *J. Chem. Phys.* **2006**, *125*, 084711.
- [89] Trzaskowski, B.; Adamowicz, L. *Theor. Chem. Acc.* **2009**, *124*, 95.
- [90] Wang, L.; Yi, C.; Zou, H.; Xu, J.; Xu, W. *Chem. Phys.* **2010**, *367*, 120.
- [91] Wang, L.; Xu, J.; Yi, C.; Zou, H.; Xu, W. *Journal of Molecular Structure: THEOCHEM* **2010**, *940*, 76.
- [92] Halls, M. D.; Schlegel, H. B. *J. Phys. Chem. B* **2002**, *106*, 1921.
- [93] Halls, M. D.; Raghavachari, K. *Nano Lett.* **2005**, *5*, 1861.
- [94] Lu, T.; Goldfield, E. M.; Gray, S. K. *J. Phys. Chem. C* **2008**, *112*, 2654.
- [95] Lu, T.; Goldfield, E. M.; Gray, S. K. *J. Phys. Chem. C* **2008**, *112*, 15260.
- [96] Lu, T.; Goldfield, E. M.; Gray, S. K. *J. Phys. Chem. C* **2010**, *114*, 9030.

- [97] Ravinder, P.; Subramanian, V. *J. Phys. Chem. C* **2013**, *117*, 5095.
- [98] Giacinto, P.; Bottoni, A.; Calvaresi, M.; Zerbetto, F. *J. Phys. Chem. C* **2014**, *118*(9), 5032–5040.
- [99] Marforio, T. D.; Bottoni, A.; Giacinto, P.; Zerbetto, F.; Calvaresi, M. *J. Phys. Chem. C* **2017**, *121*(49), 27674–27682.
- [100] Bento, A.; Sola, M.; Bickelhaupt, F. *J. Chem. Theory Comput.* **2008**, *4*(6), 929–940.
- [101] Zhao, Y.; Truhlar, D. G. *J. Chem. Theory Comput.* **2010**, *6*(4), 1104–1108.
- [102] Vreven, T.; Byun, K. S.; Komáromi, I.; Dapprich, S.; Montgomery, J. A.; Morokuma, K.; Frisch, M. J. *J. Chem. Theory Comput.* **2006**, *2*, 815.
- [103] Humphrey, W.; Dalke, A.; Schulten, K. *J. Mol. Graphics* **1996**, *14*, 33.
- [104] Vreven, T.; Morokuma, K.; Farkas, .; Schlegel, H. B.; Frisch, M. J. *J. Comput. Chem.* **2003**, *24*, 760.
- [105] Dewar, M. J. S.; Zoebisch, E. G.; Healy, E. F. *J. Am. Chem. Soc.* **1985**, *107*, 3902.
- [106] Mayo, S. L.; Olafson, B. D.; Goddard, W. A. *J. Phys. Chem.* **1990**, *94*, 8897.
- [107] Barlow, S. E.; van Doren, J. M.; Bierbaum, V. M. *J. Am. Chem. Soc.* **1988**, *110*, 7240.
- [108] Halls, M. D.; Schlegel, H. B. *J. Phys. Chem. B* **2002**, *106*(8), 1921–1925.
- [109] van Zeist, W. J.; Bickelhaupt, F. M. *Org. Biomol. Chem.* **2010**, *8*, 3118–3127.
- [110] Li, Y.; Osuna, S.; Garcia-Borràs, M.; Qi, X.; Liu, S.; Houk, K. N.; Lan, Y. *Chem. Eur. J.* **2016**, *22*(36), 12819–12824.
- [111] Breaker, R. R.; Joyce, G. F. *Chem. Biol.* **1994**, *1*, 223.
- [112] Mills, D. R.; Peterson, R. L.; Spiegelman, S. *Proc. Natl. Acad. Sci. U. S. A.* **1967**, *58*, 217.
- [113] Joyce, G. F. *Angew. Chem., Int. Ed.* **2007**, *46*, 6420.
- [114] Chandra, M.; Silverman, S. K. *J. Am. Chem. Soc.* **2008**, *130*, 2936.

- [115] Mohan, U.; Burai, R.; McNaughton, B. R. *Org. Biomol. Chem.* **2013**, *11*, 2241.
- [116] Li, Y. F.; Sen, D. *Nat. Struct. Mol. Biol.* **1996**, *3*, 743.
- [117] Flynn-Charlebois, A.; Wang, Y.; Prior, T. K.; Rashid, I.; Hoadley, K. A.; Coppins, R. L.; Wolf, A. C.; Silverman, S. K. *J. Am. Chem. Soc.* **2003**, *125*, 2444.
- [118] Sheppard, T. L.; Ordoukhanian, P.; Joyce, G. F. *Proc. Natl. Acad. Sci. U. S. A.* **2000**, *97*, 7802.
- [119] Chiuman, W.; Li, Y. *Chem. Biol.* **2006**, *13*, 1061.
- [120] Gellert, M.; Lipsett, M. N.; Davies, D. R. *Proc. Natl. Acad. Sci. U. S. A.* **1962**, *48*, 2013.
- [121] Arnott, S.; Chandrasekaran, R.; Marttila, C. M. *Biochem. J.* **1974**, *141*, 537.
- [122] McManus, S. A.; Li, Y. *Molecules* **2010**, *15*, 6269.
- [123] Semlow, D. R.; Silverman, S. K. *J. Mol. Evol.* **2005**, *61*, 207.
- [124] Hoadley, K. A.; Purtha, W. E.; Wolf, A. C.; Flynn-Charlebois, A.; Silverman, S. K. *Biochemistry* **2005**, *44*, 9217.
- [125] Kost, D. M.; Gerdt, J. P.; Pradeepkumar, P. I.; Silverman, S. K. *Org. Biomol. Chem.* **2008**, *6*, 4391.
- [126] Silverman, S. K. *Acc. Chem. Res.* **2009**, *42*, 1521.
- [127] Purtha, W. E.; Coppins, R. L.; Smalley, M. K.; Silverman, S. K. *J. Am. Chem. Soc.* **2005**, *127*, 13124.
- [128] Coppins, R. L.; Silverman, S. K. *J. Am. Chem. Soc.* **2005**, *127*, 2900.
- [129] Wang, Y.; Silverman, S. K. *Biochemistry* **2005**, *44*, 3017.
- [130] Bennett, C. F.; Swayze, E. E. *Annu. Rev. Pharmacol. Toxicol.* **2010**, *50*, 259.
- [131] Goyenvalle, A.; Griffith, G.; Babbs, A.; Andaloussi, S.; Ezzat, K.; Avril, A.; Dugovic, B.; Chaussenot, R.; Ferry, A.; Voit, T.; Amthor, H.; Bühr, C.; Schürch, S.; Wood, M. J.; Davies, K. E.; Vaillend, C.; Leumann, C.; Garcia, L. *Nat. Med.* **2015**, *21*, 270.

- [132] Aldaye, F. A.; Palmer, A. L.; Sleiman, H. F. *Science* **2008**, *321*, 1795.
- [133] Jones, M. R.; Seeman, N. C.; Mirkin, C. A. *Science* **2015**, *347*, 840.
- [134] Turner, A. P. *Chem. Soc. Rev.* **2013**, *42*, 3184.
- [135] Kim, H. N.; Ren, W. X.; Kim, J. S.; Yoon, J. *Chem. Soc. Rev.* **2012**, *41*, 3210.
- [136] Boersma, A. J.; Coquière, D.; Geerdink, D.; Rosati, F.; Feringa, B. L.; Roelfes, G. *Nat. Chem.* **2010**, *2*, 991.
- [137] Guo, Y.; Zhou, L.; Xu, L.; Zhou, X.; Hu, J.; Pei, R. *Sci. Rep.* **2015**, *4*, 7315.
- [138] Wu, C.; Wan, S.; Hou, W.; Zhang, L.; Xu, J.; Cui, C.; Wang, Y.; Hu, J.; Tan, W. *Chem. Commun.* **2015**, *51*, 3723.
- [139] Ponce-Salvatierra, A.; Wawrzyniak-Turek, K.; Steuerwald, U.; Hobartner, C.; Pena, V. *Nature* **2016**, *529*, 231.
- [140] Bartel, D. P.; Szostak, J. W. *Science* **1993**, *261*, 1411.
- [141] Joyce, G. F. *Annu. Rev. Biochem.* **2004**, *73*, 791.
- [142] Wirmer-Bartoschek, J.; Schwalbe, H. *Angew. Chem., Int. Ed.* **2016**, *55*, 5376.
- [143] Calvaresi, M.; Garavelli, M.; Bottoni, A. *Proteins: Struct., Funct., Genet.* **2008**, *73*, 527.
- [144] Siegbahn, P. E. M.; Borowski, T. *Faraday Discuss.* **2011**, *148*, 109.
- [145] Bottoni, A.; Miscione, G. P.; Calvaresi, M. *Phys. Chem. Chem. Phys.* **2011**, *13*, 9568.
- [146] Williams, R. T.; Wang, Y. *Biochemistry* **2012**, *51*, 6458.
- [147] Wójcik, A.; Broclawik, E.; Siegbahn, P. E. M.; Borowski, T. *Biochemistry* **2012**, *51*, 9570.
- [148] Sheng, X.; Liu, Y. *Biochemistry* **2013**, *52*, 8079.
- [149] Aranda, J.; Cerqueira, N. M. F. S. A.; Fernandes, P. A.; Roca, M.; Tuñon, I.; Ramos, M. J. *Biochemistry* **2014**, *53*, 5820.
- [150] Marforio, T. D.; Giacinto, P.; Bottoni, A.; Calvaresi, M. *Biochemistry* **2015**, *54*, 4404.

- [151] Fick, R. G.; Clay, C. C.; Vander Lee, L.; Scheiner, S.; Al-Hashimi, H.; Trievel, R. C. *Biochemistry* **2018**, *57*, 3733.
- [152] Rankin, J. A.; Mauban, R. C.; Fellner, M.; Desguin, B.; McCracken, J.; Hu, J.; Varganov, S. A.; Hausinger, R. P. *Biochemistry* **2018**, *57*, 3244.
- [153] Lintuluoto, M.; Lintuluoto, J. M. *Biochemistry* **2016**, *55*, 4697.
- [154] Messiha, H. L.; Ahmed, S. T.; Karuppiah, V.; Suardiaz, R.; Ascue Avalos, G. A.; Fey, N.; Yeates, S.; Toogood, H. S.; Mulholland, A. J.; Scrutton, N. S. *Biochemistry* **2018**, *57*, 1997.
- [155] Fisher, G.; Thomson, C. M.; Stroek, R.; Czekster, C. M.; Hirschi, J. S.; da Silva, R. G. *Biochemistry* **2018**, *57*, 4357.
- [156] Klahn, M.; Rosta, E.; Warshel, A. *J. Am. Chem. Soc.* **2006**, *128*, 15310.
- [157] Prasad, B. R.; Plotnikov, N. V.; Warshel, A. *J. Phys. Chem. B* **2013**, *117*, 153.
- [158] Kirby, A. J.; Nome, F. *Acc. Chem. Res.* **2015**, *48*, 1806.
- [159] Pereira, E. S.; Da Silva, J. C. S.; Brandao, T. A. S.; Rocha, W. R. *Phys. Chem. Chem. Phys.* **2016**, *18*, 18255.
- [160] Lilley, D. M. J. *Biochem. Soc. Trans.* **2017**, *45*, 683.
- [161] Lilley, D. M. J. *Philos. Trans. R. Soc., B* **2011**, *366*, 2910.

List of Figures

1.1	Schematic representation of the cavity shapes formed in the medium to accommodate the solute. In particular, the surface described by a) spherical cavity, b) VDW radii, c) solvent-accessible surface. . .	18
1.2	The entire system (<i>Real</i>) is partitioned into a model system (<i>Mod</i>) and an environment (<i>Env</i>). <i>Mod</i> is described with QM approach <i>Env</i> is described with MM approach.	25
2.1	Two charges q_1 and q_2 with position r_1 and r_2 respectively (On top). The same system after a rigid translation Δr (On bottom).	32
2.2	Possible S_N2 mechanism: a <i>front-side</i> attack mechanism (unfavoured) and a <i>back-side</i> attack mechanism (favoured)	33
2.3	<i>Back</i> and <i>front-side</i> S_N2 mechanisms with their computed gas-phase profiles (kcal mol ⁻¹) for the preliminary complex Rx and transition states (TS_{Back} , in blue lines and TS_{Front} , in red lines).	34
2.4	The x-,y-,z-directions of Reactants, Rx , TS_{Back} and TS_{Front} for the chlorine exchange reaction between methyl chloride and chloride anion.	35
2.5	Rx and Rx2 with their relative orientation in the chosen Cartesian system.	37
2.6	Qualitative picture of a hypothetical reaction, where chloride anion leading nucleophilic attack on chloride atom instead of the classical electrophilic carbon atom, thanks to $-F_z$ (on top). A generalisation of this behaviour (bottom).	38

- 2.7 Reaction profiles of chlorine exchange reaction between methyl chloride and chloride anion under the influence of $F_z = 5.0 \times 10^{-3} a.u.$. At $F_z = -5.0 \times 10^{-3} a.u.$ methyl chloride molecule rotates by 180° by paying E_{Reorg} 39
- 2.8 Reaction profiles of chlorine exchange reaction between methyl chloride and chloride anion under the influence of $F_z = 10.0 \times 10^{-3} a.u.$. At $F_z = -10.0 \times 10^{-3} a.u.$ methyl chloride molecule rotates by 180° by paying E_{Reorg} . The same reaction profile under the influence of $F_z = 12.5 \times 10^{-3} a.u.$ is reported below. The picture underlines that **Rx** is not a critical point anymore. 41
- 2.9 From the left to the right side, norbornane structure with the relative carbon atoms numeration, 7-chloronorbornane (ClNor), syn-7-chloro-2-norbornanone (ClNorCO) and syn-7-chloro-2,3-norbornandione (ClNor2CO) 43
- 2.10 Reaction mechanisms (on the left) and profiles (on the right) for chlorine exchange reaction between chloride anion and 1) ClNor, 2) ClNorCO and 3) ClNor2CO. 43
- 2.11 OEEF orientations for the ClNor molecule. Three cases from left to right: F_z, F'_z and F''_z 44
- 2.12 **Rx** geometry changing when $F_z = \pm 2.5 \times 10^{-3} a.u.$ for the z-axis orientation considered (F_z, F'_z and, F''_z). 45
- 2.13 Reaction profiles of chlorine exchange reaction between 7-chloronorbornane and chloride anion under the influence of $F = 2.5 \times 10^{-3} a.u.$. At $F = -2.5 \times 10^{-3} a.u.$ 7-chloronorbornane molecule rotates by 180° by paying E_{Reorg} . F_z is applied on the system (top), F'_z is applied on the system (middle), F''_z is applied on the system (bottom). . . 46
- 2.14 Reaction profiles of chlorine exchange reaction between 7-chloronorbornane and chloride anion under the influence of $F = 5.0 \times 10^{-3} a.u.$. At $F = -5.0 \times 10^{-3} a.u.$ 7-chloronorbornane molecule rotates by 180° by paying E_{Reorg} . F_z is applied on the system (left), F'_z is applied on the system (right). 47
- 2.15 Reaction profile of the chlorine exchange reaction between 7-chloronorbornane and chloride anion under the influence of $F''_z = 5.0 \times 10^{-3} a.u.$. At $F''_z = -5.0 \times 10^{-3} a.u.$ 7-chloronorbornane molecule rotate by 180° by paying E_{Reorg} 48
- 2.16 *Back* and *front-side* S_N2 mechanisms with their reaction profiles (kcal mol⁻¹). 50
- 2.17 The x-,y-,z-directions for the Mentschutkin reaction between ammonia and methyl chloride. 51

2.18	The x-,y-,z-directions for isolated reactants and products.	51
2.19	The x-,y-,z-directions for Rx1 , Rx2 , Rx3	52
2.20	The x-,y-,z-directions for TS_{Back}	54
2.21	Internal (ΔE_{Int}^\ddagger) and global barriers (ΔE_{Glob}^\ddagger) of the <i>back-side</i> mechanism as a function of the field intensity in the scanned range $R(F_z, 10^{-3}a.u.)$	55
2.22	OEEF effect on the <i>back-side</i> mechanism on the unperturbed case (black lines) when $F_z = 12.5 \times 10^{-3}a.u.$ (green lines). All points refer to the unperturbed isolated reactants.	57
2.23	The x-,y-,z-directions for TSS_{Front} of the Menschutkin reaction. TS_{Front} with nucleophilic attack from the <i>front-side</i> with the C-Cl bond oriented along the z-axis TS_{Front}^a . TS with nucleophilic attack from the <i>front-side</i> with the C-N bond oriented along the z-axis TS_{Front}^b	58
2.24	ΔE_{Int}^\ddagger) and global barriers (ΔE_{Glob}^\ddagger) of the <i>front-side</i> mechanism as function of the field intensity in the scanned range $R(F_z, 10^{-3}a.u.)$. On the left. TS_{Front}^a . On the right. TS_{Front}^b	59
2.25	Global (ΔE_{Glob}^\ddagger) barrier of <i>back-side</i> and <i>front-side</i> mechanism as function of the field intensity in the scanned range $R(F_z, 10^{-3}a.u.)$ (left); internal (ΔE_{Int}^\ddagger) barrier of <i>back-side</i> and <i>front-side</i> mechanism as function of the field intensity in the scanned range $R(F_z, 10^{-3}a.u.)$. (right) for the Menschutkin reaction between methyl chloride and ammonia.	60
2.26	The x-,y-,z-directions for Pd1 , Pd2 , Pd3	61
2.27	Reaction mechanism of Menschutkin reaction in presence of OEEFs. $F_z = 12.5 \times 10^{-3}a.u.$ (top), $F_z = 0.0a.u.$ (middle) $F_z = 12.5 \times 10^{-3}a.u.$ (bottom).	63
2.28	Possible ring opening mechanisms for the 4-electrons electrocyclic ring opening of cyclobutene: a <i>disrotatory</i> mechanism (forbidden) and a <i>conrotatory</i> mechanism (allowed).	64
2.29	Possible rotations for the allowed <i>conrotatory</i> mechanism. An <i>inward</i> and a <i>outward</i> rotation could occur	65

- 2.30 The orientation of the coordinate system and applied field and representation of the induced dipole moment in reactants (\mathbf{R}_x) and transition state (\mathbf{TS}). Two different perspectives are given: along the y-axis (top) and along the x-axis (bottom). The relative orientations of the electric field F_z (positive) and dipole μ_z (negative) shown in the picture stabilize the system. The increase of the dipole from reactants to transition state (top) stabilizes more \mathbf{TS} than \mathbf{R}_x and lowers the activation barrier 67
- 2.31 Reaction profiles (kcal mol⁻¹) for the *conrotatory* (*inward* and *outward* rotation pathways) ring opening reaction of 3-methylcyclobutene and 3-aminocyclobutene in the absence of OEEF. 69
- 2.32 Activation energies (ΔE^\ddagger , kcal mol⁻¹) for the *conrotatory* ring opening reaction of 3-methylcyclobutene as a function of the applied field along the three axes ($F, 10^{-3}a.u.$). In red *outward* rotation pathway (\mathbf{TS}_{Out}), in blue *inward* rotation pathway (\mathbf{TS}_{In}). 69
- 2.33 Activation energies (ΔE^\ddagger , kcal mol⁻¹) for the *conrotatory* ring opening reaction of 3-aminocyclobutene as a function of the applied field along the three axes ($F, 10^{-3}a.u.$). In red *outward* rotation pathway (\mathbf{TS}_{Out}), in blue *inward* rotation pathway (\mathbf{TS}_{In}). 71
- 2.34 Activation energies (ΔE^\ddagger , kcal mol⁻¹) for the *conrotatory* ring opening reaction of a) 3-nitrosocyclobutene; b) cyclobut-2-en-1-ylborane and c) 3-formylcyclobutene, as a function of the applied field along the three axes ($F, 10^{-3}a.u.$). 73
- 2.35 Activation energies (ΔE^\ddagger , kcal mol⁻¹) for the *conrotatory* ring opening reaction of 3-formylcyclobutene, as a function of the applied field along the three axes ($F, 10^{-3}a.u.$). In red *outward* rotation pathway (\mathbf{TS}_{Out}), in blue *inward* rotation pathway (\mathbf{TS}_{In}). 74
- 2.36 Activation energies (ΔE^\ddagger , kcal mol⁻¹) for the *conrotatory* ring opening reaction of 3-nitrosocyclobutene as a function of the applied field along the three axes ($F, 10^{-3}a.u.$). In red *outward* rotation pathway (\mathbf{TS}_{Out}), in blue *inward* rotation pathway (\mathbf{TS}_{In}). 76
- 2.37 Activation energies (ΔE^\ddagger , kcal mol⁻¹) for the *conrotatory* ring opening reaction of 3-nitrosocyclobutene as a function of the applied field along the three axes ($F, 10^{-3}a.u.$). In red *outward* rotation pathway (\mathbf{TS}_{Out}), in blue *inward* rotation pathway (\mathbf{TS}_{In}). 78
- 2.38 Activation energies (ΔE^\ddagger , kcal mol⁻¹) for the *conrotatory* ring opening reaction of cyclobut-2-en-1-ylborane as a function of the applied field along the three axes ($F, 10^{-3}a.u.$). In red *outward* rotation pathway (\mathbf{TS}_{Out}), in blue *inward* rotation pathway (\mathbf{TS}_{In}). 78

3.1	Elicity vector C (top) different CNT types (bottom)	84
3.2	S_N2 , <i>syn</i> E2 and <i>anti</i> E2 mechanisms.	85
3.3	S_N2 , <i>syn</i> E2 and <i>anti</i> -E2 mechanisms (on top). Reaction profiles (kcal mol ⁻¹) computed at the M06-2X level for the gas-phase reaction mechanisms (on bottom).	88
3.4	S_N2 , <i>syn</i> E2 and <i>anti</i> E2 model mechanisms inside a CNT.	89
3.5	S_N2 mechanism activation energies (ΔE^\ddagger , kcal mol ⁻¹) versus CNT diameter. In grey the unperturbed gas-phase activation energy.	90
3.6	Activation energy difference ($\Delta\Delta E^\ddagger$) between the confined reaction ($\Delta E^\ddagger(CNT)$) and the unperturbed gas phase reaction ($\Delta E^\ddagger(Gas)$).	90
3.7	<i>syn</i> and <i>anti</i> E2 mechanisms activation energies (ΔE^\ddagger , kcal mol ⁻¹) versus CNT diameter. In grey the unperturbed gas-phase activation energy for both mechanisms.	93
3.8	<i>syn</i> and <i>anti</i> E2 mechanisms activation energies (ΔE^\ddagger , kcal mol ⁻¹) versus CNT diameter. In grey the unperturbed gas-phase activation energy for both mechanisms.	94
3.9	<i>syn</i> -E2 reaction energies (ΔE , kcal mol ⁻¹) versus CNT diameter. In grey the unperturbed gas-phase reaction energy.	95
3.10	Reaction energy difference ($\Delta\Delta E$) between the confined reaction ($\Delta E(CNT)$) and the unperturbed gas phase reaction ($\Delta E(Gas)$).	96
3.11	S_N2 , <i>syn</i> E2 and <i>anti</i> -E2 mechanisms for ethyl chloride/4-chloro-1-butene with chloride anion (on top). Reaction profiles (kcal mol ⁻¹) computed at the M06-2X level for the gas-phase reaction mechanisms (on bottom).	97
3.12	S_N2 , <i>syn</i> E2 and <i>anti</i> -E2 mechanisms for ethyl chloride/4-chloro-1-butene with chloride anion (on top). Reaction profiles (kcal mol ⁻¹) computed at the M06-2X level for the graphene-hosted reaction mechanisms (on bottom).	98
4.1	Schematic representation of the model-system used in QM computations. The continuous lines indicate the sequence of DNA nucleotides, the dotted lines indicate the hydrogen bonds between GTP ⁵¹ and A ⁵⁰ of RNA strands and 9DB1.	104
4.2	Basis sets used for the atoms included in the model-system. The marked atoms (blue) were described by the 6-31G* basis. The 3-21G* basis was used for all remaining atoms. In black bold lines the part of the system kept frozen during the calculations.	104

-
- 4.3 On top. A conventional representation of the reaction mechanism for the 9DB1-catalyzed reaction. On bottom. Reaction profile of the figure computed at the M06-2X//6-31G*/3-21G* computational level. In square brackets are the values obtained at the M06-2X//6-311++G**/6-31+G* level. 106
- 4.4 Schematic two-dimensional representation of the reactant complex **Rx** and transition state **TS1** with the related distances (Å) on margins. 107
- 4.5 Reaction profile at the M06-2X//6-31G*/3-21G* level for the 9DB1-catalyzed reaction obtained after inclusion of the zero-point energy corrections. In square brackets the values obtained at the M06-2X//6-311++G**/6-31+G* level. 108
- 4.6 Schematic two-dimensional representation of the reactant complex **Int** and transition state **TS2** with the related distances (Å) on margins. 109
- 4.7 *In silico* mutagenesis operated on (first row) the 2'-hydroxyl group and (second row) dA¹³ phosphate. The corresponding computed activation barriers (kcal mol⁻¹) for TS1 are reported. 110

List of Tables

2.1	Bond length (R) and partial charges (q) of methyl chloride, at different intensities of the OEEF along the z-axis. Relative energies of methyl chloride and chloride anion (E) refer to the unperturbed state.	36
2.2	Bond lengths: (R) and partial charges (q) of Rx and Rx2 at different intensities of the OEEF along the z-axis. Relative energies of Rx and Rx2 (E) refer to unperturbed Rx	37
2.3	Bond lengths (R), partial charges (q), global (ΔE_{Glob}^{\neq}) and internal (ΔE_{Int}^{\neq}) barriers of TS_{Back} and TS_{Front} at different intensities of the OEEF along the z-axis	42
2.4	Bond length (R) and partial charges (q) of the transition state for the <i>back-side</i> mechanism, at different intensities of the OEEF along the z, z' and z''-axis.	48
2.5	Geometrical parameters Bond lengths: (R), angles: (A) and partial charges (q) of reagents and products at different intensities of the OEEF along the z-axis. Relative energies reported refer to the unperturbed state.	52
2.6	Bond lengths (R) and partial charges (q) of Rx1 , Rx2 , Rx3 at different intensities of the OEEF along the z-axis. Relative energies refer to the most stable Rx	53
2.7	Energies of Rx1 and Rx3 E (kcal mol ⁻¹) referred to reactants in their positive field value and relative energies referred to reactants in their negative field value by considering E_{Reorg} . Finally, energy difference between Rx1 and Rx3 : $\Delta\Delta E$ (kcal mol ⁻¹).	53

2.8	Internal (ΔE_{Int}^\ddagger) and global (ΔE_{Glob}^\ddagger) barriers of the <i>back-side</i> mechanism. Bond lengths (R) and partial charges (q) of TS_{Back} , at different intensities of the OEEF along the z-axis.	55
2.9	Induced dipole moment along z-axis: μ_z (D) of methyl chloride, ammonia, reactants, Rx and TS_{Back} when $F_z = 0.0$ to $12.5 \times 10^{-3} a.u.$ The last row is the induced dipole moment variation $\Delta\mu_z$ (D) per critical point.	56
2.10	Internal (ΔE_{Int}^\ddagger) and global (ΔE_{Glob}^\ddagger) barriers of TSs_{Front}^{a,b} . Bond lengths (R) and partial charges (q) of the transition state for the <i>front-side</i> nucleophilic attack, at different intensities of the OEEF along the z-axis.	58
2.11	Induced dipole moment along z-axis: μ_z (D) of methyl chloride, ammonia, reactants, Rx , TS_{Front}^a and TS_{Front}^b when $F_z = 0.0$ to $\pm 12.5 \times 10^{-3} a.u.$ The forth and the last rows is the induced dipole moment variation $\Delta\mu_z$ (D) per critical point.	60
2.12	Bond lengths (R) and partial charges (q) of Pd1 , Pd2 , Pd3 at different intensities of the OEEF along the z-axis. Relative energies refer to the most stable Pd	62
2.13	Activation energies (ΔE^\ddagger , kcal mol ⁻¹) and reaction energies (ΔE_{React} for the <i>conrotatory</i> ring opening of 3-methylcyclobutene at different fields ($F, 10^{-3} a.u.$) applied along the three Cartesian axes.	70
2.14	Induced dipole ($\mu_{x,y,z}$) along the direction of the applied field ($F_{x,y,z}, 10^{-3} a.u.$) for the various critical points located for the thermal ring-opening of 3-methylcyclobutene.	70
2.15	Activation energies (ΔE^\ddagger , kcal mol ⁻¹) and reaction energies (ΔE_{React} , kcal mol ⁻¹) for the <i>conrotatory</i> ring opening of 3-aminocyclobutene at different fields ($F, 10^{-3} a.u.$) applied along the three Cartesian axes.	71
2.16	Induced dipole ($\mu_{x,y,z}$) along the direction of the applied field ($F_{x,y,z}, 10^{-3} a.u.$) for the various critical points located for the thermal ring-opening of 3-aminocyclobutene.	71
2.17	Activation energies (ΔE^\ddagger , kcal mol ⁻¹) and reaction energies (ΔE_{React} , kcal mol ⁻¹) for the <i>conrotatory</i> ring opening of 3-formylcyclobutene at different fields ($F, 10^{-3} a.u.$) applied along the three Cartesian axes.	74
2.18	Induced dipole ($\mu_{x,y,z}$) along the direction of the applied field ($F, 10^{-3} a.u.$) for the various critical points located for the thermal ring-opening of 3formylcyclobutene.	75

2.19	Activation energies (ΔE^\ddagger , kcal mol ⁻¹) and reaction energies (ΔE_{React} , kcal mol ⁻¹) for the <i>conrotatory</i> ring opening of 3-nitrosocyclobutene at different fields (F , 10 ⁻³ a.u.) applied along the three Cartesian axes.	76
2.20	Induced dipole ($\mu_{x,y,z}$) along the direction of the applied field (F , 10 ⁻³ a.u.) for the various critical points located for the thermal ring-opening of 3-nitrosocyclobutene.	77
2.21	Activation energies (ΔE^\ddagger , kcal mol ⁻¹) and reaction energies (ΔE_{React} , kcal mol ⁻¹) for the <i>conrotatory</i> ring opening of cyclobut-2-en-1-ylborane at different fields (F , 10 ⁻³ a.u.) applied along the three Cartesian axes.	79
2.22	Induced dipole ($\mu_{x,y,z}$) along the direction of the applied field (F , 10 ⁻³ a.u.) for the various critical points located for the thermal ring-opening of cyclobut-2-en-1-ylborane	79
3.1	Diameter and circumference (Å) of armchair CNTs from (6,6) to (12,12)	85
3.2	Critical points energy (kcal mol ⁻¹) for the S _N 2 and E2 (<i>syn</i> and <i>anti</i>) mechanisms. Energies are calculated with M06-2X functional with different basis set (6-311+G**, 6-311++G** and 6-311++G(2df,2p)) with the reference CCSD(T)/CBS value obtained by Bento <i>et al.</i> [100].	86
3.3	Energetic contributions to the overall confinement effect on the S _N 2 kinetics: $\Delta\Delta E^\ddagger$, $\Delta E(Geom, guest)$, $\Delta E(Geom, host)$, $\Delta E(vdW)$ and $\Delta E(Elec)$	92
3.4	Energetic contributions to the overall confinement effect on the <i>syn</i> and <i>anti</i> -E2 kinetics: $\Delta\Delta E^\ddagger$, $\Delta E(Geom, guest)$, $\Delta E(Geom, host)$, $\Delta E(vdW)$ and $\Delta E(Elec)$	94
3.5	Critical points energies of TS _{S_N2} , TS _{<i>syn</i>E2} , TS _{<i>anti</i>E2} and Pd in gas phase and on a graphene sheet for R=H, CHCH ₂ , respectively.	96
3.6	Critical points energies of TS _{S_N2} , TS _{<i>syn</i>E2} , TS _{<i>anti</i>E2} and Pd in gas phase and on a graphene sheet for R=H, CHCH ₂ , respectively.	99